UNIVERSITY OF OKLAHOMA

GRADUATE COLLEGE

EXPERIMENTAL STUDY OF CS ISOTROPIC AND ANISOTROPIC POLYATOMIC RYDBERG MOLECULES

A DISSERTATION

SUBMITTED TO THE GRADUATE FACULTY

in partial fulfillment of the requirements for the

Degree of

DOCTOR OF PHILOSOPHY

By

JIN YANG
Norman, Oklahoma
2019

EXPERIMENTAL STUDY OF CS ISOTROPIC AND ANISOTROPIC POLYATOMIC RYDBERG MOLECULES

A DISSERTATION APPROVED FOR THE
HOMER L. DODGE DEPARTMENT OF PHYSICS AND ASTRONOMY

BY

Dr. James P. Shaffer, Chair

Dr. Arne Schwettmann

Dr. Alberto Marino

Dr. Bruno Uchoa

Dr. Henry Neeman

© Copyright by JIN YANG 2019
All Rights Reserved.

To Cs_2^+, I finally find you and know about you.

Acknowledgements

I would first like to acknowledge my advisor James P. Shaffer, who takes me into the wonderful cold atom world. It is Jim's hard working that encourages me to finish my graduate research. Second, I would like to acknowledge Hossein Sadeghpour at ITAMP and Seth Rittenhouse at United States Naval Academy for their invaluable theoretical contributions. Then I would like to acknowledge Dr. Donald W. Booth. He prepared me for my research on ultralong-range Rydberg molecules. Without his help, I could not finish my graduate study at this moment. I would also like to thank Dr. Jiteng Sheng, Dr. Santosh Kumar, Dr. Jon Sedlacek, Dr. Haoquan Fan, Akbar Jahangiri Jozani and George Chao for their valuable suggestions and kindly help, and Peter Schauss at the university of Virginia for offering me the chance to work on ultracold degenerate Fermi gas.

At the end, I would like to acknowledge my parents for their support from China. And my love, Chao. Thanks for her love and support. Lots of things changed during my graduate study, but her love and support never.

Table of Contents

Abstract

In this thesis, we investigate few-body physics and many-body physics of ultralong-range Rydberg molecules. Ultralong-range Rydberg molecules are formed through scattering processes between Rydberg electrons and ground state atoms. The huge size of the Rydberg electron's orbit makes the Rydberg electron able to interact with more than one ground state atom in cold atomic gases with atom number densities from 10^{12} cm^{-3} to 10^{14} cm^{-3}. In cold atomic gases, the ground state atoms on average are far away from each other. They are weakly interacting. Depending on the angular momentum state of the Rydberg electron, two types of polyatomic Rydberg molecules have been studied. When the Rydberg electron is in an ns state, the isotropic probability distribution of the Rydberg electron makes the Rydberg electron interact with different ground state atoms equally. The total binding energy is a summation of the binding energy from each scattering process. These additive interactions have been studied using Cs $6s + 83s$ and $6s + 90s$ polyatomic Rydberg molecules in this thesis. When the Rydberg electron is in an $l > 0$ angular momentum state, spatial correlations between different ground state atoms are established through the anisotropic probability distribution of the Rydberg electron. The total binding energy depends on the relative positions of different ground state atoms. These nonadditive interactions are studied using Cs $6s + 6s + 34d$ and $6s + 6s + 36d$ triatomic Rydberg molecules in this thesis.

Chapter 1

Introduction

Ultralong-range Rydberg molecules, a novel kind of molecules formed between Rydberg atoms and ground state atoms is a significant discovery and can be seen as a milestone of the century-long research on Rydberg atoms. The investigation of interactions between Rydberg atoms and ground state atoms can be tracked back to 1934 when Edoardo Amaldi and Emilio Segré observed energy shifts of Rydberg atoms immersed in a dense gas of ground state atoms [1]. The transition lines were supposed to always move to the red because of the screening effect generated by the ground state atoms inserted between the Rydberg ion cores and Rydberg electrons. Surprisingly, for different atomic species, both red line shifts and blue line shifts were observed. In the same year, Enrico Fermi developed the zero-energy pseudopotential and resolved this contradictory result [2]. When Rydberg electrons get close to the outer turning points of their orbits, they can be approximately seen as free electrons with zero speed. A low energy scattering happens between the Rydberg electron and the ground state atoms in the vicinity of the outer turning point, figure 1.1. The resulting energy shift can be treated by a delta function potential located at the ground state atom and proportional to the electron-atom scattering length. The original model created by Enrico Fermi only includes s-wave scattering. It was extended for p-wave scattering, d-wave scattering and other high order scatterings by Omont in 1977 [3]. In 2000, using this model, Chris Greene *et al.* predicted the existence of ultralong-range Rydberg

molecules [4]. They found the scattering process between a Rydberg electron and a ground state atom with negative scattering length generates negative energy shifts, which can support bound molecular states.

So far, ultralong-range Rydberg molecules have been observed and studied successfully using Rb, Cs and Sr. Ultralong-range Rydberg molecules in low angular momentum states ($l < 3$) possess shallow Born-Oppenheimer potential energy curves (PECs) that oscillate as a function of the internuclear distance. The oscillations mimic the behavior of the Rydberg electron's radial wavefunction and the depth of the potential energy curve is around several hundred MHz. When Rydberg electrons are in high angular momentum states ($l \geq 3$), the angular momentum states are degenerate. A summation of the degenerate wavefunctions with opposite parities breaks the spherical symmetry of the probability distribution of the Rydberg electron and makes the Rydberg electron tend to be localized around the ground state atom. The positive charge center and the negative charge center do not overlap anymore. A giant permanent dipole moment is established. This makes Rydberg molecules the only homonuclear diatomic molecules which possess dipole moments. One example of the probability distributions for this type of Rydberg molecules is shown in figure 1.2. As it looks like an ancient trilobite fossil, this type of Rydberg molecule is named a "trilobite" molecule. High angular momentum states also mean the Rydberg electrons have little chance to get close to the ion cores and they concentrate their probability distributions far away from the ion cores. This causes the potential wells to be much deeper than potential wells of low angular momentum states. The typical depth of the

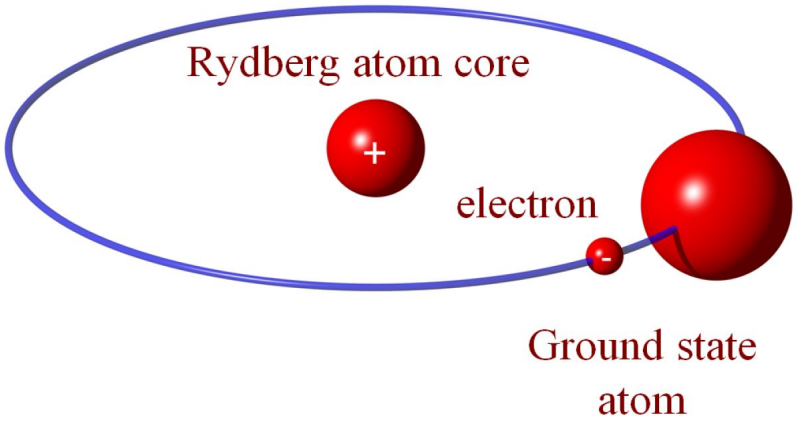

Figure 1.1: The scheme of the basic structure of an ultralong-range Rydberg molecule. The binding is generated by the scattering between the Rydberg electron and the ground state atom.

potential wells of Rydberg molecules in high angular momentum states is several GHz.

High order scatterings possess shape resonances. They are metastable states in which an electron is trapped due to the shape of a potential barrier. Shape resonances can shift potential energy curves dramatically, which makes different potential energy curves tend to cross each other. Avoided crossings generated by p-wave shape resonances mix low angular momentum states with high angular momentum states [5]. This makes the molecular states generated by the avoided crossings behave like a second type of Rydberg molecules. In contrast to "trilobite" molecules, the probability distribution of the Rydberg electron is butterfly shaped. This type of Rydberg molecule is named a "butterfly" molecule.

Although research on interactions between Rydberg atoms and ground state atoms started around one century ago, intensive and diverse study of ultralong-range Rydberg molecules started one decade ago with the popularization of laser cooling and trapping techniques. The first observation of ultralong-range Rydberg

molecules was achieved by Tilman Pfau's group at the university of Stuttgart in 2009 [6]. The bound molecular states generated by internal quantum reflection and avoided crossings were observed shortly after that [7, 8]. The behavior of Rydberg molecules in electric and magnetic fields has also been explored [9, 10, 11, 12]. Recently, scientists started to consider spin dependent relativistic effects. One prominent effect is that spin-spin interactions between Rydberg electrons and electrons in ground state atoms can mix singlet scattering channels with triplet scattering channels, forming a new series of potential energy curves [13, 14, 15, 16].

The observation and measurement of the large permanent dipole moments of ultralong-range Rydberg molecules were challenging for many years. This is because directly exciting electrons to high angular momentum states to generate "trilobite" and "butterfly" molecules needs a sophisticated experimental setup. Due to the selection rules, three lasers with different frequencies are needed to excite ground state electrons where $l = 0$, to $l \geq 3$ angular momentum states. More fields, for example microwaves, are required to excite angular momentum states where $l \geq 3$. So far, direct excitation of Rydberg molecules to high angular momentum states has not been achieved. A clever strategy to circumvent this obstacle was developed by our group in 2015. Due to the quasi-integer quantum defect of the Cs ns state ~ 4.05, low angular momentum states are degenerate with $n - 4$ high angular momentum states. Mixing with high angular momentum states leads the Cs $6s + ns$ Rydberg molecules to possess large permanent dipole moments. On the other hand, ns states can be reached using two-photon transitions from the ground state. In 2015, we photoassociated Cs $6s + 37s$, $6s + 39s$, $6s + 40s$

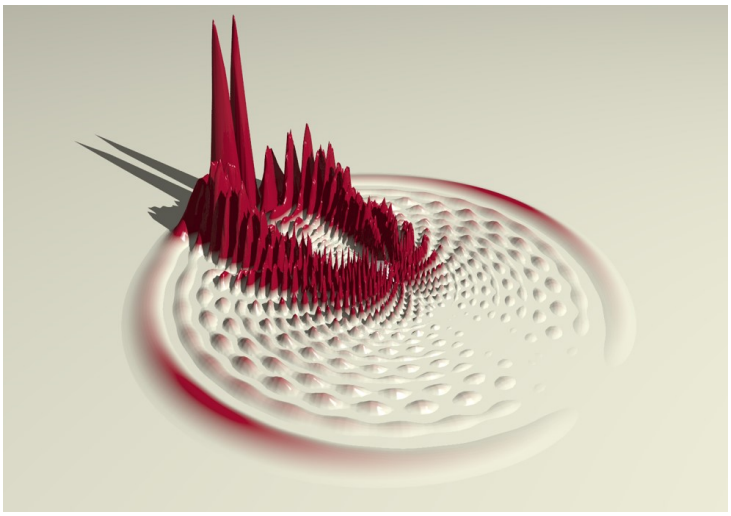

Figure 1.2: The probability distribution of the Rydberg electron of a "trilobite" molecule. The height represents the probability. The silver ball represents the Rydberg ion core. The ground state atom is buried under the two highest peaks.

"trilobite" molecules and succeeded in measuring their permanent dipole moments for the first time [12].

Rydberg electrons are highly excited electrons with enormous orbits. The typical size of Rydberg molecules is ~ 100 nm. Ultralong-range Rydberg molecules are excellent candidates to explore many-body physics. The large space between the Rydberg ion cores and Rydberg electrons make it possible to have more than one ground state atom within the orbit of the Rydberg electron. When the atom number density is extremely high ($> 10^{14}$ cm^{-3}), Rydberg molecules can be used to probe shape resonances [17]. In Bose-Einstein condensates a Rydberg atom can be seen as an impurity which interacts with all ground state atoms nearby [18, 19, 20, 21]. More interestingly, when the atom number density is moderate ($\sim 10^{11}$ cm^{-3} to $\sim 10^{13}$ cm^{-3}), few-body physics can be studied, where spatial correlations between different ground state atoms have been observed and reported [22, 23, 24].

The first evidence of polyatomic Rydberg molecules was reported by Tilman Pfau's group in 2010 [7]. Molecular signals observed in the spectra with a frequency difference of twice the binding energy of the ground molecular dimer state were shown to be Rydberg trimer signals. In 2012, as they went to higher principal quantum states, $n = 60$ to $n = 110$, higher orders of polyatomic Rydberg molecules formed by more ground state atoms were observed, where a series of molecular signals formed by different numbers of ground state atoms was evenly distributed on the red side of the Rydberg transition line [25]. The frequency difference between two of the adjacent molecular signals is the binding energy of the Rydberg dimer. The binding energies of Rydberg molecules formed by different numbers of ground state atoms are multiples of the binding energy of the Rydberg dimer. These results can be understood intuitively by imagining the orbit of the Rb ns Rydberg electron as spherically symmetric and very large. Different ground state atoms interacting with the Rydberg electron are far away from each other and independent. The total binding energy is a summation of the binding energy of each scattering process.

When a Rydberg electron is in an np, nd, or even higher angular momentum state, the probability distribution is not spherically symmetric anymore. This makes the total binding energy from different ground state atoms angularly dependent, where the angles are determined by the relative positions of different ground state atoms. In 2018, we studied Cs $6s + 6s + 34d$ and $6s + 6s + 36d$ triatomic Rydberg molecules and observed the angular dependence of the binding energy caused by the anisotropic probability distribution of the Rydberg electron

for the first time [24].

This thesis is organized as follows. Chapter 2 introduces the Fermi pseudopotential. We firstly introduce some basic properties of Rydberg atoms. An understanding of Rydberg atom properties helps to understand the formation of ultralong-range Rydberg molecules. Then we give expressions which describe s-wave scattering and p-wave scattering. We consider the spin dependent relativistic effects, which include spin-orbit coupling and spin-spin coupling. Then we investigate how a Rydberg molecule behaves in electric fields and how a Rydberg electron interacts with more than one ground state atom.

In Chapter 3, we describe the experimental apparatus used to conduct the Rydberg molecule experiments. The experiments were conducted in an ultracold environment which is achieved by combining a Zeeman slower, magneto-optical trap and far-off-resonance trap. Two-photon transition, photoionization, ion detection and the time sequence of the experiment are presented.

In Chapter 4, we present our work on few-body and many-body physics of Rydberg molecules, where we investigate the manner in which a Rydberg electron interacts with more than one ground state atom. There are two different situations. The first one is when the Rydberg electron is in an ns state. Its probability distribution is isotropic. In the second situation, the Rydberg electron is in an $l > 0$ state, where the probability distribution is anisotropic. We compare our results with theoretical study and good agreement is obtained. We conclude in Chapter 5 and discuss several topics which will be interesting in the future. Detailed information about the setup of our experiment are at the end of this

thesis as appendices.

Chapter 2

Theory

2.1 Introduction

Ultralong-range Rydberg molecules are investigated using spectroscopy. Correspondingly, we need to calculate the molecular states and simulate the spectra theoretically. The goal of this chapter is to introduce the model we create to analyze and characterize ultralong-range Rydberg molecules and the method we use to simulate the bound molecular states. In the seminal paper written by Chris Greene in 2000 [4], the scattering between a Rydberg electron and a ground state atom is treated as a perturbation of the unperturbed spherically symmetric Coulomb potential generated by the Rydberg ion core. We can obtain the Hamiltonian for the Rydberg electron in the ulralong-range Rydberg molecule by writing the potential term as a combination of the Coulomb potential and the Fermi pseudopotential. Knowing the Hamiltonian, potential energy curves (PECs) of the Rydberg electron can be calculated. Then we can obtain bound molecular states and simulations of spectra. Since the scattering is treated as a perturbation, eigenenergies and wavefunctions of the Rydberg electron in the unperturbed Coulomb potential have to be known to calculate the perturbation [26]. In the first part of this chapter, we introduce Rydberg atom physics.

The accuracy of the Hamiltonian determines the accuracy of the calculations and simulations. To obtain an accurate Hamiltonian, both s-wave scattering and

p-wave scattering are included. p-wave shape resonances of Cs change the potential energy curves dramatically. Compared to Rb, the p-wave shape resonances of Cs need to be treated more carefully. Spin dependent relativistic effects are important for ultralong-range Rydberg molecules. The fine structure and hyperfine structure generated by the spin dependent relativistic effects have been observed using modern, advanced spectroscopic techniques. After adding the spin dependent relativistic effects into the Hamiltonian, we obtain the most complete Hamiltonian up to now.

Two concrete examples are presented in the last part of this chapter, which demonstrate how we adjust the model and extend the Hamiltonian according to different conditions. The first example focuses on the most important property, the dipole moments of ultralong-range Rydberg molecules. Ultralong-range Rydberg molecules possessing dipole moments behave like pendula in electric fields instead of free rigid rotors. We demonstrate how the Hamiltonian changes when the ultralong-range Rydberg molecule is in electric fields. Using the new Hamiltonian, we describe what will be different in the spectra when the ultralong-range Rydberg molecule is in an electric field. The second example focuses on a situation where a Rydberg electron interacts with several ground state atoms. We demonstrate how to extend the Hamiltonian to include all different scatterings with different ground state atoms. This is the theoretical background for Chapter 4, where we present our work on isotropic and anisotropic polyatomic Rydberg molecules.

2.2 Rydberg Atoms

2.2.1 Scaling Laws

Rydberg atoms have their outer electrons in a high principal quantum number state $n \geq 10$. A highly excited hydrogen atom is the simplest Rydberg atom, where the potential is [27]

$$V(r) = -\frac{1}{4\pi\epsilon_0}\frac{1}{r}. \tag{2.1}$$

The loosely bound electron has a tiny binding energy,

$$E = -\frac{e^2/4\pi\epsilon_0}{2a_0}\frac{1}{n^2}, \tag{2.2}$$

and an enormous orbital with a radius r,

$$r = a_0 n^2, \tag{2.3}$$

where a_0 is a constant called Bohr radius. e is the charge of the electron. ϵ_0 is the vacuum dielectric constant.

Since the potential is a spherically symmetric Coulomb potential, properties of Rydberg atoms are functions of r. Knowing expectation values of r^σ where σ is a positive or negative integer, one can understand the properties of Rydberg atoms. In table 2.1, we list some expectation values of r^σ as functions of the principal quantum number n. This can help us to quickly estimate the change of the property as n changes, as soon as we know its expression as a function

Table 2.1: Expectation values of r^σ for H in atomic units [28, 29].

$< r >$	$= \frac{1}{2}[3n^2 - l(l+1)]$
$< r^2 >$	$= \frac{n^2}{2}[5n^2 + 1 - 3l(l+1)]$
$< 1/r >$	$= \frac{1}{n^2}$
$< 1/r^2 >$	$= \frac{1}{n^3(l+1/2)}$
$< 1/r^3 >$	$= \frac{1}{n^3(l+1)(l+1/2)l}$
$< 1/r^4 >$	$= \frac{3n^2 - l(l+1)}{2n^5(l+3/2)(l+1)(l+1/2)l(l-1/2)}$
$< 1/r^6 >$	$= \frac{35n^4 - 5n^2[6l(l+1) - 5] + 3(l+2)(l+1)l(l-1)}{8n^7(l+5/2)(l+2)(l+3/2)(l+1)(l+1/2)l(l-1/2)(l-1)(l-3/2)}$

When $\sigma > 0$, expectation values of r^σ are determined mostly by the location of the outer classical turning point, $r = a_0 n^2$. This is because the electron spends most of its time there. So for $\sigma > 0$, $< r^\sigma > \sim n^{2\sigma}$. When $\sigma < -1$, the behavior of the small r part of the wavefunction is important. For $n \gg l$, $< r^\sigma > \sim n^{-3}$.

of r. For example, we know the operator of the dipole moment is $\boldsymbol{d} = e\boldsymbol{r}$, the expectation value can be calculated as,

$$\boldsymbol{d}_{nl,nl'} =< \psi_{nlm}|e\boldsymbol{r}|\psi_{nl'm} > \ \sim \ n^2. \tag{2.4}$$

For a hydrogen atom, if we excite it from the ground $1s$ state to the Rydberg $10s$ state, its dipole moment increases 100 times. This makes Rydberg atoms very sensitive to electric fields, because the dipole moment is directly related to the atomic polarizability. A moderate electric field can make a notable shift of the energy level. The electric field can be a DC field, which causes a DC Stark

Table 2.2: Selected scaling laws for Cs Rydberg atoms [28].

Property	Scales as	Cs $40s_{1/2}$
Orbital Radius r	n^2	123 nm
Energy Spacing between Adjacent Levels ΔE	n^{-2}	136 GHz
Polarizability P	n^7	6 MHz (V cm^{-1})$^{-2}$
Radiative Lifetime τ_0	n^3	68 μs

shift. It can also come from laser light, which causes an AC Stark shift. Another example is the diamagnetic effect. It is proportional to the area of the orbit of the Rydberg electron, which is proportional to r^2. Using table 2.1, we know the diamagnetic effect scales as n^4. The diamagnetic shifts which are very difficult to be observed in low n states are obvious in Rydberg states.

For some properties we frequently use, tabulating their scaling laws is very helpful. Table 2.2 shows a short list of representative properties and demonstrates how Rydberg atom properties change with n.

2.2.2 Energies of Rydberg states

The essential difference between a highly excited hydrogen atom and the highly excited alkali atoms we use in our experiment is that the nucleus of the alkali atom is surrounded by inner electrons. The screening effect generated by the inner electrons makes the net charge of a Rydberg ion core be $+e$ when the Rydberg electron is outside the ion core. In this case, the structure of the Rydberg atom can be modelled using the structure of a hydrogen atom. The energy levels of

Rydberg atoms are similar to the energy levels of hydrogen atoms. However, when Rydberg electrons are in low angular momentum states ($l < 3$), they have a chance to penetrate into the inner shells and "see" more positive charges. Thus the screening of the nuclear charge by the inner shell electrons is less effective. As Rydberg electrons get to higher angular momentum states ($l \geq 3$), the chance to penetrate into inner shells rapidly decreases. To take into account this scenario, we modify the expression of the energy levels, equation 2.2, slightly,

$$E = -\frac{e^2/4\pi\epsilon_0}{2a_0}\frac{1}{(n-\delta_l)^2}. \tag{2.5}$$

A small experimentally determined quantity δ_l, called the quantum defect, is subtracted from the principal quantum number n to give an effective principal quantum number $n^* = n - \delta_l$. The subscript means the quantum defect depends on the angular momentum state of the Rydberg electron. The quantum defect can be further parameterized

$$\delta_l = \mu_l(0) + \frac{\mu_l'(0)}{(n-\mu_l(0))^2}, \tag{2.6}$$

where $\mu_l(0)$ and $\mu_l'(0)$ for $ns, np, nd, and\ nf$ states of Rb [30, 31] and Cs [32, 33] are given in table 2.3. For higher angular momentum states, the quantum defects account for core polarization through the approximate formula [34]

$$\delta_{l_{\text{high}}} = \frac{\alpha_c[3n^2 - l(l+1)]/4}{n^2(l-1/2)l(l+1/2)(l+1)(l+3/2)}, \tag{2.7}$$

Table 2.3: Quantum defect parameters for Rb and Cs [30, 31, 32, 33].

Rb	$\mu_l(0)$	$\mu_l'(0)$	Cs	$\mu_l(0)$	$\mu_l'(0)$
$s_{1/2}$	3.1311804	0.1784	$s_{1/2}$	4.049325	0.2462
$p_{1/2}$	2.6548849	0.2900	$p_{1/2}$	3.591556	0.3714
$p_{3/2}$	2.6416737	0.2950	$p_{3/2}$	3.559058	0.374
$d_{3/2}$	1.34809171	-0.60286	$d_{3/2}$	2.475365	0.5554
$d_{5/2}$	1.34646572	-0.59600	$d_{5/2}$	2.466210	0.067
$f_{5/2}$	0.0165192	-0.085	$f_{5/2}$	0.033392	-0.191
$f_{7/2}$	0.0165437	-0.086	$f_{7/2}$	0.033537	-0.191

where α_c is the polarizability of the Rydberg ion core. For Rb, $\alpha_c = 9.11$, for Cs, $\alpha_c = 15.8$, in atomic units.

2.2.3 Wavefunctions of Rydberg States

Since Rydberg electrons in different angular momentum states have different chances to penetrate into inner shells of the Rydberg ion cores, an l dependent potential is used when we calculate the wavefunctions of the Rydberg electrons [35],

$$V_l(r) = -\frac{Z_l(r)}{r} - \frac{\alpha_c}{2r^4}[1 - e^{-(r/r_c)^6}]. \tag{2.8}$$

The first term on the right side of the equation is the Coulomb potential generated by the nucleus. The second term comes from the polarization interaction between the Rydberg electron and the ion core. $1 - e^{-(r/r_c)^6}$ is a cut-off function, which prevents the singularity of the potential at the origin. r_c is the cut-off radius, which is chosen to be of the order of the core radius. Some authors treat r_c as a

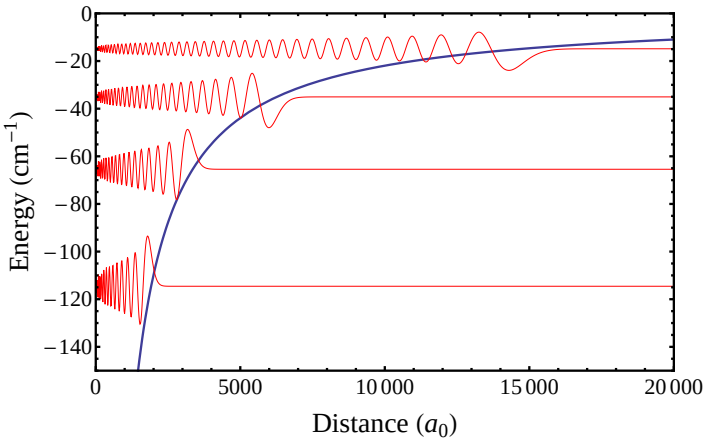

Figure 2.1: The blue curve is the l dependent potential calculated using equation 2.8 where $l = 0$. The red curves are wavefunctions of $35s$, $45s$, $60s$, $90s$ Rydberg states calculated using the RADIAL program.

variable parameter to be chosen to reproduce accurate experimental data. α_c is the static dipole polarizability of the ion core, Z_l is the charge parameter which can be expressed as

$$Z_l(r) = 1 + (Z-1)e^{-a_1 r} - r(a_3 + a_4 r)e^{-a_2 r}, \tag{2.9}$$

where Z is the nuclear charge of the atom, and a_n are fitting parameters fit to measured energy levels. The wavefunctions can be obtained by numerically solving the Schrödinger equation using a Fortran program called RADIAL [36]. Numerical results of the wavefunctions are obtained on series of grid points which changes depending on how many nodes are in the wavefunction, see figure 2.1.

Additionally, this program can calculate continuum wavefunctions above the ionization threshold using the SFREE subroutine, which is necessary for determining photoionization cross sections for Rydberg states in an optical dipole trap.

2.2.4 Lifetimes of Rydberg States

Rydberg atoms decay radiatively due to spontaneous emission as a result of the coupling of the atom to the vacuum electromagnetic field. The radiative lifetime τ_0 of a Rydberg state nl can be expressed as

$$\frac{1}{\tau_0} = \Gamma_0 = \sum_{E_{nl} > E_{n'l'}} A(nl \rightarrow n'l'), \tag{2.10}$$

where Γ_0 is the total transition rate to all states $n'l'$ lower than the Rydberg state nl. It is a sum of the Einstein A coefficients, which is the transition rate to a single state $n'l'$. The Einstein A coefficient can be expressed as,

$$\mathrm{A}(nl \rightarrow n'l') = \frac{4\omega_{nn'}^3}{3c^3} \frac{l_{max}}{2l+1} R^2(nl \rightarrow n'l'), \tag{2.11}$$

where $\omega_{nn'}$ is the transition frequency between n and n'. l_{max} is the larger of l and l', c is speed of light, and $R(nl \rightarrow n'l')$ is a radial matrix element of the electric dipole transition. The transition rate from nl to $n'l'$ depends on the frequency difference and the dipole matrix between them. Equation 2.11 together with Equation 2.2 indicate two important results. First, decay back to the lowest allowed state is the dominant process, because the frequency difference ω between them is the largest. Second, when a Rydberg electron is in a high principal quantum number state n, further increasing n only makes a tiny increase of the frequency difference. Therefore, in the limit of high n, the Einstein A coefficient changes mostly determined by the dipole matrix between the Rydberg state and

the low lying state. The wavefunction of a Rydberg electron in an nl state has little overlap with the radial wavefunction of a valence electron in a low $n'l'$ state. The small overlap makes the transition rate back to the low lying state of a Rydberg electron very small [37]. Thus, the radiative lifetimes of Rydberg electrons are very long. As listed in table 2.2, the radiative lifetime of the Cs $40s$ Rydberg atom can be as long as 68 μs. The radiative lifetimes scale with n as [28]

$$\tau_0 = \tau(n^*)^3, \tag{2.12}$$

where n^* is the effective principal quantum number, and τ is a parameter for the radiative lifetime that depends on l and the properties of the atom.

Blackbody radiation makes an atom in a Rydberg state nl transition to nearby states $n'l'$. For Rb at $T = 300$ K, around $n = 30$, blackbody-radiation-induced decay is the dominant decay process. Blackbody-radiation-induced decay can be expressed as

$$\frac{1}{\tau_{BBR}} = \Gamma_{BBR} = \sum_{n'} \mathrm{A}(nl \to n'l') \frac{1}{\exp(\omega_{nn'}/kT) - 1}. \tag{2.13}$$

Here the blackbody-radiation-induced decay can go to any states with a transition amplitude weighted by the Planck distribution.

When there is no photoionization or other ionization processes, the total decay rate is a sum of the spontaneous decay rate and the blackbody-radiation-induced decay rate [38]

$$\frac{1}{\tau_{eff}} = \Gamma_0 + \Gamma_{BBR} = \frac{1}{\tau_0} + \frac{1}{\tau_{BBR}}, \tag{2.14}$$

where τ_{eff} is the effective lifetime of the Rydberg state. Equation 2.14 gives results approximately consistent with experimental observations. To get a better agreement with experimental observations, we use an equation with fitting parameters [38],

$$\tau_{eff} = \left[\frac{1}{\tau_s (n^*)^\delta} + \frac{A}{(n^*)^D} \frac{21.4}{\exp(315780B/(n^*)^C T) - 1}\right]^{-1}. \tag{2.15}$$

These parameters vary with different effective principal quantum number n^*, angular momentum states l and different atomic species. This expression gives very good agreement with experimental observations. Parameters can be found in reference [38].

In our experiment, we use a far-off-resonance trap (FORT) laser to photoionize Rydberg molecules and Rydberg atoms [39, 40]. We conducted experiments to investigate the photoionization rate by the beams of our FORT laser. The result is shown in figure 2.2. The effective lifetimes of the Rydberg atoms are reduced when the Rydberg atoms are confined in our FORT. Equation 2.14 for the atoms in our FORT becomes [41]

$$\frac{1}{\tau_{eff}} = \Gamma_0 + \Gamma_{BBR} + \Gamma_{photo-ion} = \frac{1}{\tau_0} + \frac{1}{\tau_{BBR}} + \frac{1}{\tau_{photo-ion}}. \tag{2.16}$$

$\Gamma_{photo-ion}$ is the photoionization rate. It depends on laser intensity I, laser frequency ω and photoionization cross section $\sigma_{photo-ion}$,

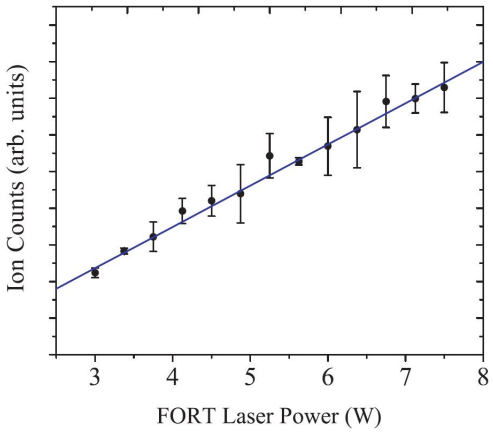

Figure 2.2: Photoionized Rydberg atom counts as a function of the FORT laser power in our experiment. The maximum density of our cold atomic cloud is around 5×10^{12} cm^{-3}, the temperature is around 40 μK. The solid blue line is a linear fit to the data. It crosses the horizontal axis at a non-zero point, which indicates other ionization channels exist. The error bar is the standard deviation. This result is reported in [41].

$$\Gamma_{photo-ion} = \frac{I}{\hbar\omega}\sigma_{photo-ion}. \tag{2.17}$$

The photoionization cross section can be calculated as,

$$\sigma_{photo-ion} = 2\pi^2 \frac{\hbar e^2}{m_e c}\frac{df}{dE}, \tag{2.18}$$

where df/dE can be written as,

$$\frac{df}{dE} = \sum_{l=l_{Ryd}-1}^{l_{Ryd}+1} \frac{2m_e\omega l_>}{3\hbar(2l_{Ryd}+1)}\left|\int \psi_{n,l}(r) r \psi_{L,E}(r) dr\right|^2. \tag{2.19}$$

l_{Ryd} is the angular momentum quantum number of the Rydberg state, $l_>$ is the greater of l and l_{Ryd}. $\psi_{n,l}(r)$ is the Rydberg state wavefunction. $\psi_{L,E}(r)$ is the continuum wavefunction with energy E.

2.2.5 Summary

Many characteristics of ultralong-range Rydberg molecules are stemmed from the exaggerated properties of Rydberg atoms, for example, the geometric size and the lifetime. Therefore a better understanding of the properties of Rydberg atoms helps to understand the formation of ultralong-range Rydberg molecules and their characteristics. Scaling laws are handy tools to quickly estimate how the properties of Rydberg atoms change as n changes. Exact calculations of these properties require a knowledge of the eigenenergies and wavefunctions of the Rydberg electron. Since the scattering that binds a Rydberg electron and a ground state atom together is treated as a perturbation, the eigenenergy and wavefunction of the Rydberg electron in the Coulomb potential are also needed to calculate the potential energy curves generated by the scattering. Because of the screening effect, the eigenenergy and wavefunction of a Rydberg electron depend on its angular momentum state. This means the angular momentum state of the Rydberg electron has an important impact on the properties of Rydberg molecules, for example, the dipole moments of Rydberg molecules and the total binding energies of polyatomic Rydberg molecules, which we will discuss in following sections.

2.3 Ultralong-range Rydberg Molecules

2.3.1 s-wave Scattering Process

In 1934, Edoardo Amaldi and Emilio Segré conducted a famous experiment. The basic idea of the experiment is straightforward. They mixed small amounts of Rydberg alkali atoms (Na, K) with rare gas atoms (Ar, He, Ne, H_2, N_2) at densities of $\sim 10^{19}$ cm^{-3} to observe the energy shifts of the Rydberg states. Since Rydberg electrons have very large orbits, the space between the Rydberg electron and the Rydberg ion core is filled with polarizable, rare gas atoms instead of vacuum when the density is high enough. If we consider a polarizable dielectric plate placed between two parallel charged conductive plates, we can derive what Edoardo Amaldi and Emilio Segré expected at that time. According to this model, there will be a red shift of the Rydberg electron's energy level, which means the transition frequency is smaller, or equivalently, the energy difference between the Rydberg level and the ground state level becomes smaller, no matter what rare gases are present. But the result of the experiment was surprising and not consistent with this simple model. The pressure shifts of Ar and He were to the red, while the pressure shift of Ne was to the blue, which means the transition frequency was larger. Shortly after the experiment, Enrico Fermi developed quantum zero-energy scattering theory to explain the experimental results.

Ground state atoms in the vicinity of Rydberg electrons can be polarized by the Rydberg electrons. The interaction between the Rydberg electron and the

polarized ground state atom is

$$V(r) = -\frac{1}{(4\pi\epsilon_0)^2}\frac{\alpha q^2}{2r^4}, \tag{2.20}$$

where α is the polarizability of the ground state atom. Unlike the Coulomb potential, equation 2.1, which scales as $1/r$, the polarization potential scales as $1/r^4$. The potential becomes very deep when the Rydberg electron gets close to the polarized ground state atom, but increases to zero very fast when the Rydberg electron moves away from the polarized ground state atom. The polarization potential has a very small effective range.

On the other hand, the loosely bound Rydberg electrons have small kinetic energy. The kinetic energy of a Rydberg electron can be related to the principal quantum number n using Bohr's theory $mvr = n\hbar$ [42],

$$\frac{1}{2}mv^2 = \frac{1}{2}\frac{\hbar^2}{mn^2a_0^2}. \tag{2.21}$$

If we excite one hydrogen atom from the ground state $n = 1$ to a Rydberg state $n = 30$, the kinetic energy decreases 900 times. The de Broglie wavelength of the Rydberg electron is very large. Hence, the scattering between a Rydberg electron and a polarized ground state atom is a low energy, zero-range scattering process, where the long wavelength limit $kr_0 \ll 1$ is fulfilled. k is the wavevector of the de Broglie wave of the Rydberg electron and r_0 is the effective range

of the polarization potential. In this situation, partial waves of the scattering processes for higher l can be ignored, since they cannot penetrate the centrifugal barrier. The s-wave scattering process is the dominant scattering process [26]. The polarization potential extends over only a small fraction of the Rydberg electron's enormous de Broglie wavelength, the collision can be approximately treated by adding a scattering phase shift to the Rydberg electron's wavefunction. The resulting energy shift is equivalent to that provided by a delta function potential located at the perturber which is proportional to the electron-atom scattering length [2],

$$V_{\mathbf{s}}(\mathbf{r}-\mathbf{R}) = 2\pi a_{\mathbf{s}}^{\mathrm{T}}(k)\delta(\mathbf{r}-\mathbf{R}), \tag{2.22}$$

where $\mathbf{r}$ is the position of the Rydberg electron, $\mathbf{R}$ is the position of the ground state atom, and $a_{\mathbf{s}}^{\mathrm{T}}(k)$ is the energy-dependent s-wave triplet scattering length. Triplet means the spin of the Rydberg electron is parallel with the spin of the valence electron of the ground state atom. For Cs atoms we use in our experiment, $a_{\mathbf{s}}^{\mathrm{T}}(k) = -21.7\ a_0$. When they are antiparallel, the scattering process is a singlet scattering process, with a singlet scattering length $a_{\mathbf{s}}^{\mathrm{S}}(k) = -1.33\ a_0$. Only negative scattering lengths form attractive interactions between Rydberg electrons and ground state atoms. For alkali atoms, $a_{\mathbf{s}}^{\mathrm{S}}(k)$ is too small to generate deep potential wells that support bound molecular states. $a_{\mathbf{s}}^{\mathrm{T}}(k)$ can be written as a function of phase shift [43]

$$a_{\mathbf{s}}^{\mathrm{T}}(k) = \frac{\tan(\eta)}{k}, \tag{2.23}$$

where η is the phase shift. By approximating the electron's motion as a classic Coulomb system, we can get a semiclassical expression for k,

$$\frac{k(R)^2}{2} = -\frac{1}{2n^2} + \frac{1}{R}. \tag{2.24}$$

The potential energy curve generated by the scattering process at the position of the ground state atom can be evaluated as

$$\begin{aligned} V_{\mathbf{s}}^{\mathrm{T}}(\mathbf{r}, \mathbf{R}) &= < \psi_{nlm}(\mathbf{r}) | 2\pi a_{\mathbf{s}}^{\mathrm{T}}(k) \delta(\mathbf{r} - \mathbf{R}) | \psi_{nlm}(\mathbf{r}) > \\ &= 2\pi a_{\mathbf{s}}^{\mathrm{T}}(k) |\psi_{nlm}(\mathbf{R})|^2. \end{aligned} \tag{2.25}$$

The $\delta(\mathbf{r} - \mathbf{R})$ function in the interaction operator makes the final potential energy curves mimic the wavefunctions of Rydberg electrons. These shallow Born-Oppenheimer potential curves oscillate as functions of internuclear distance R. Due to the negative scattering length, the successive potential energy curve minima correlate with the successive maxima of the Rydberg electron density, figure 2.3.

When the Rydberg electrons are in high angular momentum states, different angular momentum states are degenerate. The final potential energy curves are a summation of different wavefunctions with opposite parities. Neglecting the small quantum defects of all $l \geq 3$ states, the potential energy curve generated by

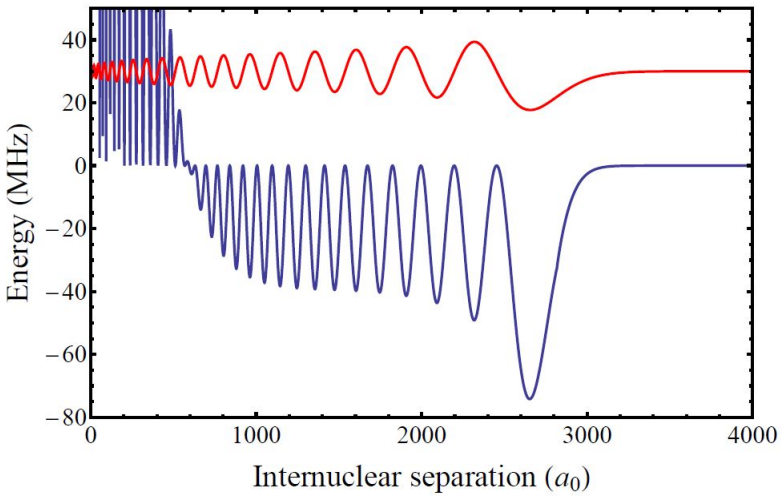

Figure 2.3: The red curve represents the Rydberg electron's wavefunction while the blue curve represents the potential energy curve of a Rydberg molecule formed by an s-wave scattering process. We can see the oscillatory potential curve tracks the radial Rydberg wavefuncion. Due to the negative scattering length, the maxima of the wavefunction correlate with the minima of the potential well. Since the scattering length depends on k, which changes along the internuclear axis, the oscillation of the potential curve is out of phase with the oscillation of the wavefunction. The tracking stops at around 600 a_0 corresponding to the Ramsauer-Townsend minima of the s-wave scattering cross section [4, 44].

the scattering process is given in terms of radial hydrogenic wavefunctions $R_{nl}(R)$ evaluated at the location of the perturber as [4],

$$U_n(R) = -\frac{1}{2n^2} + 2\pi a_{\mathbf{s}}^{\mathrm{T}}(k) \sum_{l=l_{min}}^{n-1} \frac{2l+1}{4\pi} R_{nl}(R)^2. \tag{2.26}$$

This expression can be approximated as

$$U_n(R) \approx -\frac{1}{2n^2} + a_{\mathbf{s}}^{\mathrm{T}}(k) \frac{\left(\frac{2}{R} - \frac{1}{n^2} - \frac{(l_{min}+\frac{1}{2})^2}{R^2}\right)^{\frac{1}{2}}}{\pi n^3}. \tag{2.27}$$

In this case, the Rydberg electron tends to be localized around the ground state atom. A dipole moment is established because the Rydberg electron with $-e$

is localized at the ground state atom while the Rydberg ion core has a net positive charge $+e$. The nodal pattern of the Rydberg electron's probability density function is reminiscent of a trilobite fossil, figure 1.2, so this type of ultralong-range Rydberg molecule is called a "trilobite" molecule.

2.3.2 p-wave Scattering Process and Shape Resonances

The Rydberg electron obtains more kinetic energy when it gets closer to the Rydberg ion core. High order partial waves start to penetrate the centrifugal barrier. We need to consider high order scattering processes in this situation. The next order is p-wave scattering [16, 26, 3],

$$V_{\mathbf{p}}(\mathbf{r}-\mathbf{R}) = 6\pi a_{\mathbf{p}}^3(k)\delta(\mathbf{r}-\mathbf{R})\overleftarrow{\nabla}\cdot\overrightarrow{\nabla}, \tag{2.28}$$

where $a_{\mathbf{p}}^3(k)$ is the scattering volume of the p-wave scattering process, which depends on the wavevector k of the Rydberg electron,

$$a_{\mathbf{p}}^3(k) = -\frac{\tan(\eta)}{k^3}. \tag{2.29}$$

$\overrightarrow{\nabla}$ is the gradient operator acting on the right side. $\overleftarrow{\nabla}$ is the conjugate of the gradient operator acting on the left side. η is the phase shift of the p-wave scattering. The gradient operators act in all three spatial directions, giving rise to two possible sets of states: those that maximize the gradient parallel to the internuclear axis, and those that maximize the gradient perpendicular to the internuclear axis. The former have a nodal plane perpendicular to the internuclear

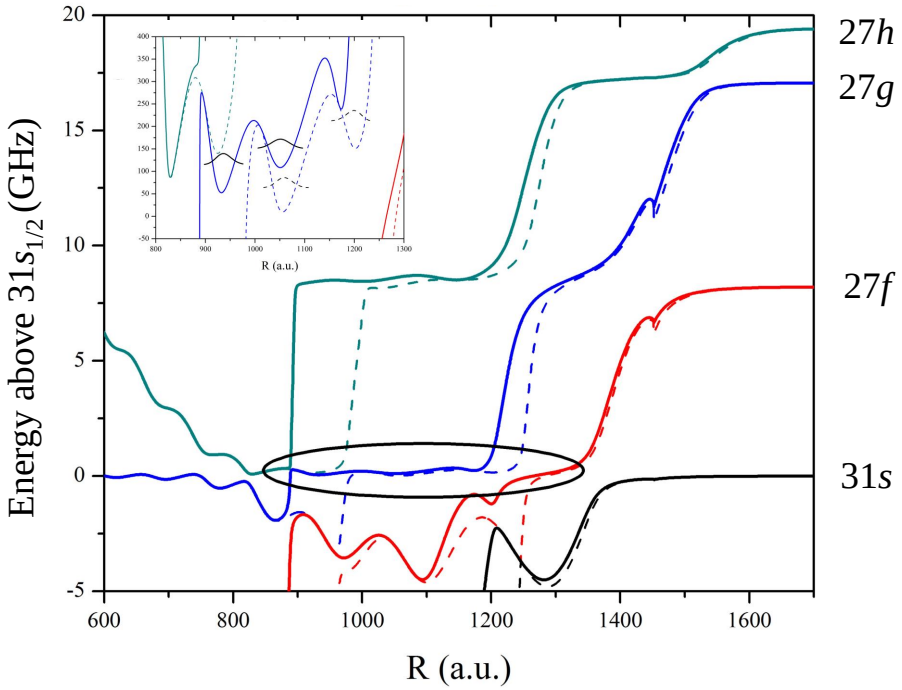

Figure 2.4: The potential energy curves near Cs $31s$ Rydberg transition. The black one is the PECs of Cs $6s + 31s$ Rydberg molecule. The green, blue, and red curves correspond to Cs $6s + 27h$, $6s + 27g$, and $6s + 27f$ Rydberg molecule. The solid lines correspond to Σ molecular symmetry, and the dashed lines correspond to Π molecular symmetry. The potential wells formed by avoided crossings can support bound molecular states mixed with hydrogenic state characters. This makes the Cs $6s + 31s$ Rydberg molecules gain large permanent dipole moments. The results have been reported in [8].

axis, and thus a Σ molecular symmetry ($m = 0$), and the latter place the nodal plane along the axis, and hence have a Π molecular symmetry ($m = 1$).

High order scattering processes, where the angular momentum of the scattered electron relative to the ground state atom is greater than zero, may support quasi-bound negative ion states, where the incident electron is trapped by the centrifugal potential barrier and attached to the ground state atom temporarily [45]. This phenomenon is called a shape resonance. Shape resonances occur at well defined energies when electrons scatter from atoms or molecules. At the

position of a resonance, the tangent of the phase shift diverges. The p-wave potential energy curves are shifted by the p-wave shape resonance dramatically. This makes potential energy curves of different angular momentum states tend to cross. The selection rules prevent the crossings and generate avoided crossings which support bound molecular states [5].

Figure 2.4 gives an example of avoided crossings generated by p-wave shape resonances. The potential energy curves near the Cs $31s$ state are shown. Since the quantum defect of the Cs ns state is -4.05, the potential energy curve of the Cs $31s$ state is almost energetically degenerate with potential energy curves of the Cs $n = 27$ high angular momentum states. Several different p-wave shape resonances at different positions along the internuclear axis shift the potential energy curves of the Cs $n = 27$ high angular momentum states dramatically. Here we focus on the Cs $27g$ state. The shape resonance makes it tend to cross the Cs $27f$ state at around 1180 a_0, where an avoided crossing is generated. The inset on the graph is a zoom-in view of the avoided crossing. Several bound molecular states are supported by the potential wells generated by the avoided crossing. These bound molecular states also possess large electric dipole moments. The nodal pattern is different from the nodal pattern of a "trilobite" molecule. It features two large "wings" of electron density extending to the usual spatial boundary of the atomic Rydberg state, but along the internuclear axis the density accumulates near the position of the perturber. This class of ultralong-range Rydberg molecule is called a "butterfly" molecule [5, 46].

p-wave shape resonances are more important for Cs than Rb [44, 47]. There are

three reasons. First, when on resonance, the cross section for Cs is almost twice the cross section for Rb. This shifts potential energy curves of Cs Rydberg molecules much more than in the case for Rb molecules. Second, different shape resonances are well separated for Cs compared to Rb. This leads to more complicate potential energy curves for Cs Rydberg molecules. As shown in figure 2.4, the potential energy curves near the Cs $31s$ state are shaped strongly by three successive p-wave shape resonances at around 1000 a_0, 1250 a_0, and 1300 a_0. Third, Cs shape resonances are within the classically accessible region of the electron kinetic energy. The resonance energy of the Cs 0^- shape resonance is only 1.69 meV [44]. The entire potential energy curve is strongly perturbed by the Cs p-wave shape resonances except the outer-most potential well, which is formed by an s-wave dominated scattering process.

2.3.3 Relativistic Effects in Rydberg Molecules

Historically, people noticed that relativistic effects influenced the motion of electrons in atoms in the early days of quantum mechanics. It was Sommerfeld who first took special relativity into account, refining Bohr's prominent contributions, to explain the fine structure of hydrogen atoms. Spin dependent relativistic effects also play a significant role in the formation of Rydberg molecules. Different spin dependent relativistic effects in an ultralong-range Rydberg molecule are shown in figure 2.5.

Depending on the spins of the Rydberg electron and the valence electron in the ground state atom, scattering processes between the Rydberg electron and the

ground state atom can be triplet scattering, where the two spins are parallel, or singlet scattering, where the two spins are antiparallel. The projection operators for triplet scattering $\hat{\mathbb{I}}_{\mathrm{T}}$ and singlet scattering $\hat{\mathbb{I}}_{\mathrm{S}}$ are

$$\hat{\mathbb{I}}_{\mathrm{T}} = \hat{\mathbf{S}}_{\mathrm{G}} \cdot \hat{\mathbf{S}}_{\mathrm{R}} + \frac{3}{4}, \tag{2.30}$$

and,

$$\hat{\mathbb{I}}_{\mathrm{S}} = \hat{\mathbb{I}} - \hat{\mathbb{I}}_{\mathrm{T}}, \tag{2.31}$$

where $\hat{\mathbf{S}}_{\mathrm{G}}$ is the spin operator of the ground state atom and $\hat{\mathbf{S}}_{\mathrm{R}}$ is the spin operator of the Rydberg atom. $\hat{\mathbb{I}}$ is the identity operator. For triplet states, the eigenvalue is one. For singlet states, the eigenvalue is zero. The wavefunction can be written as $\psi_{nlm}(\mathbf{r})|\mathrm{S_R}, \mathrm{M_R}; \mathrm{S_G}, \mathrm{M_G} >$ [16], where $|\mathrm{S_R}, \mathrm{M_R}; \mathrm{S_G}, \mathrm{M_G} >$ is the spin wavefunction. $\psi_{nlm}(\mathbf{r})$ is the unperturbed wavefunction of the Rydberg electron in the Coulomb potential,

$$\hat{H}_0 \ \psi_{nlm}(\mathbf{r}) = -\frac{1}{2(n-\delta_{n,l})^2} \ \psi_{nlm}(\mathbf{r}). \tag{2.32}$$

The PECs of s-wave triplet scatterings and singlet scatterings are

$$
\begin{aligned}
V_{\mathbf{s}}^{\mathrm{T}}(\mathbf{r},\mathbf{R}) &= 2\pi a_{\mathbf{s}}^{\mathrm{T}}(k)|\psi_{nlm}(\mathbf{R})|^2 < \mathrm{S_R},\mathrm{M_R};\mathrm{S_G},\mathrm{M_G}|\ \hat{\mathbb{I}}_{\mathrm{T}}\ |\mathrm{S_R},\mathrm{M_R};\mathrm{S_G},\mathrm{M_G}> \\
&= 2\pi a_{\mathbf{s}}^{\mathrm{T}}(k)|\psi_{nlm}(\mathbf{R})|^2 < \mathrm{S_R},\mathrm{M_R};\mathrm{S_G},\mathrm{M_G}|\ \hat{\mathbf{S}}_{\mathrm{G}}\cdot\hat{\mathbf{S}}_{\mathrm{R}} + \frac{3}{4}\ |\mathrm{S_R},\mathrm{M_R};\mathrm{S_G},\mathrm{M_G}> \\
&= 2\pi a_{\mathbf{s}}^{\mathrm{T}}(k)|\psi_{nlm}(\mathbf{R})|^2,
\end{aligned}
\tag{2.33}
$$

and,

$$
\begin{aligned}
V_{\mathbf{s}}^{\mathrm{S}}(\mathbf{r},\mathbf{R}) &= 2\pi a_{\mathbf{s}}^{\mathrm{S}}(k)|\psi_{nlm}(\mathbf{R})|^2 < \mathrm{S_R},\mathrm{M_R};\mathrm{S_G},\mathrm{M_G}|\ \hat{\mathbb{I}}_{\mathrm{S}}\ |\mathrm{S_R},\mathrm{M_R};\mathrm{S_G},\mathrm{M_G}> \\
&= 0.
\end{aligned}
\tag{2.34}
$$

Since p-wave scattering depends on the coupling between the scattering angular momentum $\mathrm{L}_{sc} = 1$ and the total spin $\mathrm{S} = \mathrm{S_R} + \mathrm{S_G}$, the uncoupled basis $\psi_{nlm}(\mathbf{r})|\mathrm{S_R},\mathrm{M_R};\mathrm{S_G},\mathrm{M_G}>$ are not the eigenstates of the spin dependent Hamiltonian when we include p-wave scattering into the Hamiltonian. We define a new basis $\psi_{nlm}(\mathbf{r})|\mathrm{J},\mathrm{M_J};\mathrm{S},\mathrm{M_S}>$, where $\mathrm{J} = \mathrm{L}_{sc}+\mathrm{S}$ is the total angular momentum and $\mathrm{M_J}$ is its projection on the internuclear axis. As discussed in the above section, the triplet ($\mathrm{S} = 1$) p-wave scattering ($\mathrm{L}_{sc} = 1$) phase shift of Cs exhibits a relatively large splitting of the resonance energy for J = 0, 1, 2. The three successive p-wave shape resonances of Cs strongly perturb all but the outer-most potential well, where the s-wave scattering process is dominant. These effects make the calculated potential energy curves of Cs Rydberg molecules very complex. In the case of Rb, we usually use a single average shape resonance curve to represent

p-wave scattering since the resonances overlap in resonance energy.

The scattering between the Rydberg electron and the ground state atom depends on the spin-spin coupling between the Rydberg electron and the valence electron of the ground state atom. Any spin dependent relativistic effects which have influence on either the spin of the Rydberg electron or the spin of the ground state electron affect the potential energy curves. This spin-spin coupling builds a bridge between the Rydberg atom and the ground state atom. The spin-orbit coupling and electron-nucleus spin coupling (hyperfine interaction) of both the Rydberg atom and the ground state atom need to be included in the calculation to obtain accurate results [13, 16]. The hyperfine interaction decreases as n^{-3}. In Rydberg states, the hyperfine interaction is too weak to affect the curves at currently relevant experimental resolutions. We only consider the hyperfine interaction of the ground state atom. The spin-orbit coupling also decreases as n^{-3}. However, in $n = 30$ to $n = 40$ states, which we discussed in Chapter 4, the spin-orbit coupling is comparable to the hyperfine interaction of the ground state atom. We include spin-orbit coupling of the Rydberg atom in our calculation. For alkali ground state atoms, there is no spin-orbit coupling since they are in an ns state. The final expression which includes all spin dependent relativistic effects is

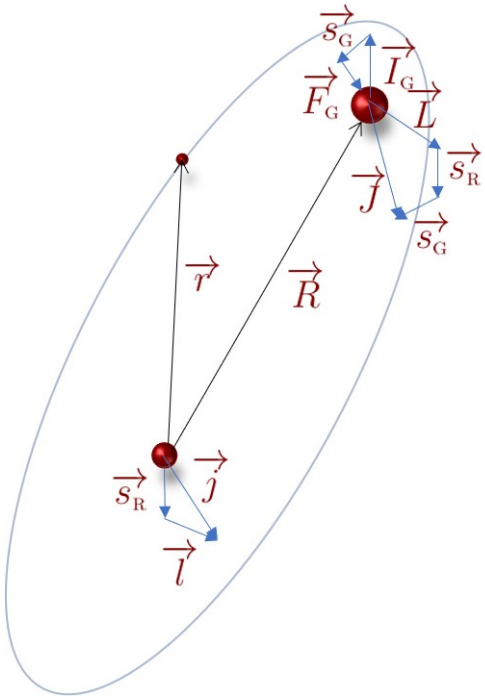

Figure 2.5: The scattering between the Rydberg electron and the ground state atom depends on the spin-spin coupling of the Rydberg electron and the valence electron of the ground state atom. Any spin dependent relativistic effects having influences on the spin status of either electron affects the potential energy curves of the formed Rydberg molecule. For the p-wave scattering process, $\overrightarrow{\mathrm{L}}_{sc} = 1$ is not zero anymore. The total spin $\overrightarrow{\mathrm{S}} = \overrightarrow{S}_{\mathrm{R}} + \overrightarrow{S}_{\mathrm{G}}$ couples with $\overrightarrow{\mathrm{L}}_{sc}$, which forms a new basis $\overrightarrow{J}$. The spin-orbit coupling of the Rydberg atom couples the spin of the Rydberg electron $\overrightarrow{S}_{\mathrm{R}}$ and the angular momentum orbital $\overrightarrow{l}$, which forms $\overrightarrow{j}$. The hyperfine interaction of the ground state atom couples the spin of the ground state electron $\overrightarrow{S}_{\mathrm{G}}$ and the spin of the nucleus $\overrightarrow{I}_{\mathrm{G}}$, which forms $\overrightarrow{F_G}$. Since the hyperfine interaction decreases as n^{-3}, the hyperfine interaction of the Rydberg atom can be ignored.

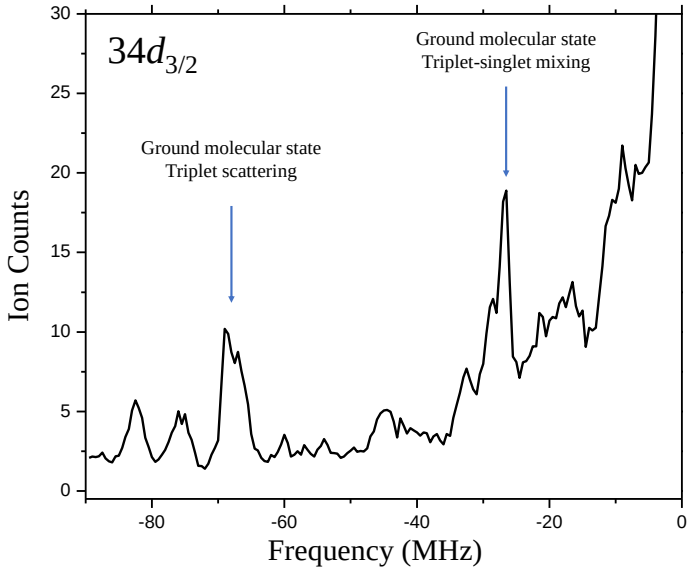

Figure 2.6: The spectrum of Cs $6s + 34d$ Rydberg molecules. One striking feature are the two labeled peaks. One is the ground molecular state of the outer-most potential well formed by triplet scattering. The other one is the ground molecular state of the outer-most potential well "duplicated" by triplet-singlet mixing due to the hyperfine interaction of the ground state atom with the Rydberg electron.

$$\begin{aligned}\hat{H} =& \hat{H}_0 + \hat{H}_{\text{so-R}} \\ &+ \hat{H}_{\text{s,T}} \cdot \hat{\mathbb{I}}_{\text{T}} + \hat{H}_{\text{s,S}} \cdot \hat{\mathbb{I}}_{\text{S}} \\ &+ \hat{H}_{\text{p,T}} \cdot \hat{\mathbb{I}}_{\text{T}} + \hat{H}_{\text{p,S}} \cdot \hat{\mathbb{I}}_{\text{S}} \\ &+ \hat{H}_{\text{hf-G}}.\end{aligned} \tag{2.35}$$

More explicitly writing out the operators,

$$\begin{aligned}\hat{H} =& \hat{H}_0 + \hat{H}_{\text{so-R}} \\ &+ 2\pi[a_{\mathbf{s}}^{\text{S}}(k)\hat{\mathbb{I}}^{\text{S}} + a_{\mathbf{s}}^{\text{T}}(k)\hat{\mathbb{I}}^{\text{T}}]\delta^{(3)}(\mathbf{r}-\mathbf{R}) \\ &+ 6\pi[a_{\mathbf{p}}^{\text{S-J}}(k)\hat{\mathbb{I}}^{\text{S}} + a_{\mathbf{p}}^{\text{T-J}}(k)\hat{\mathbb{I}}^{\text{T}}]\delta^{(3)}(\mathbf{r}-\mathbf{R})\frac{\overleftarrow{\nabla}\cdot\overrightarrow{\nabla}}{k^2} \\ &+ A\hat{\mathbf{S}}_{\text{G}} \cdot \hat{\mathbf{I}}_{\text{G}}.\end{aligned} \tag{2.36}$$

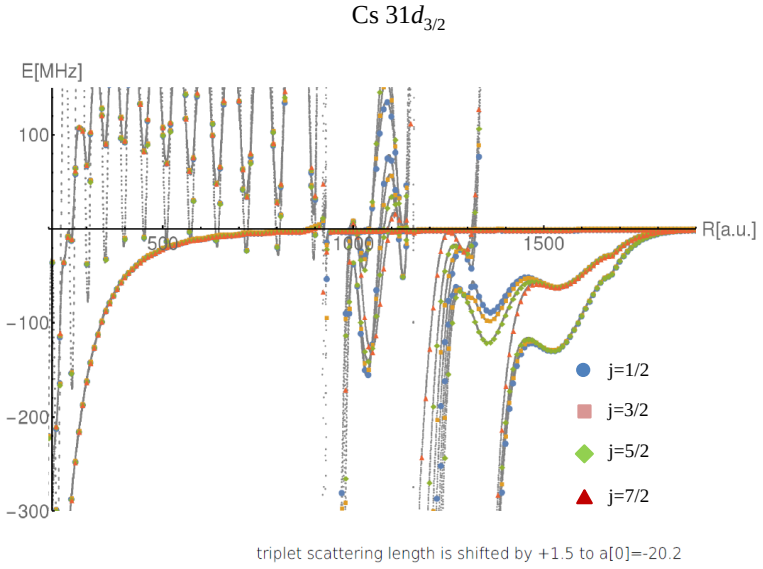

Figure 2.7: The potential energy curves of Cs $6s+31d$ Rydberg molecules. Several series of potential energy curves correspond to different projections of total angular momentum along the internuclear axis. They overlap very well when the scattering is s-wave dominated. As p-wave scattering starts to perturb the potential energy curves strongly, they start to separate energetically.

As in atoms, fine structure appears after adding the spin dependent relativistic effects.

Electron-nucleus spin coupling of the ground state atom couples singlet and triplet scattering channels. It generates a new series of potential energy curves [13], which are shallower than the potential energy curves of triplet scattering but deeper than the potential energy curves of singlet scattering. The potential wells are deep enough to support bound molecular states. These bound molecular states were first observed in 2015 [14]. Using Cs $6s+nd$ Rydberg molecules, we also observed the mixing between singlet scattering channels and triplet scattering channels, see figure 2.6. The total angular momentum $J_{tot} = l_r + s_r + s_g + I_g$ and the projection of the total angular momentum, $m_{tot} = m_{l_r} + m_{s_r} + m_{s_g} + m_{I_g}$, are the only good quantum numbers. Correspondingly, different potential energy

curves for different m_{tot} are separated in energy. For the outer-most potential wells where the s-wave scattering is dominant, it is difficult to observe the splitting of these states, as in figure 2.7. The potential energy curves are more complex for heavier atoms because of a larger m_{I_g}.

2.3.4 Rydberg Molecules in Static Electric Fields

A molecule in the gas phase is free to rotate relative to a set of mutually orthogonal axes of fixed orientation in space, centered on the center of mass of the molecule. Free rotation is not possible for molecules in liquid or solid phases due to the presence of intermolecular forces. The free rotation of a Rydberg molecule can be described as a rigid rotor. The Schrödinger equation of the free rotation is

$$\hat{H}\psi = \frac{\hat{L}^2}{2I}\psi = \frac{J(J+1)\hbar^2}{2I}\psi, \tag{2.37}$$

where $\hat{L}$ is the rotational angular momentum operator, I is the moment of inertia of the Rydberg molecule. By defining the rotation constant $B = \hbar^2/2I$, the rotational energy can be written as

$$E = J(J+1)B, \tag{2.38}$$

where J is the rotational quantum number, which is a positive integer.

Ultralong-range Rydberg molecules possessing large permanent dipole moments cannot be seen as free rigid rotors anymore in static electric fields. Instead, we model them as harmonic pendula. The Schrödinger equation of the pendular state

can be written as,

$$\hat{H}\psi = \left[\frac{\hat{L}^2}{2I} - \mu \cdot \epsilon\right]\psi, \tag{2.39}$$

where the first term on the right side of the equation describes the rotation and the second term describes the interaction between the electric field and the Rydberg molecule. μ is the dipole moment of the Rydberg molecule, ϵ is the strength of the electric field. If the static electric field is very weak or the dipole moment of the Rydberg molecule is very small, the interaction between the Rydberg molecule and the electric field can be treated as a perturbation. When the static electric field is very strong or the dipole moment of the Rydberg molecule is very large, the interaction between them becomes the dominant term. Here we define a parameter η,

$$\eta = \frac{\mu \cdot \epsilon}{B}, \tag{2.40}$$

which we use to describe the strength of the interaction between the Rydberg molecule and the static electric field. When the interaction is very strong, the Rydberg molecule cannot rotate a full circle, but behaves like a pendulum. The energy of the pendular movement is,

$$E \xrightarrow{\eta \to large} -\eta + (\nu + 1)(2\eta)^{1/2} \cdot B, \tag{2.41}$$

where

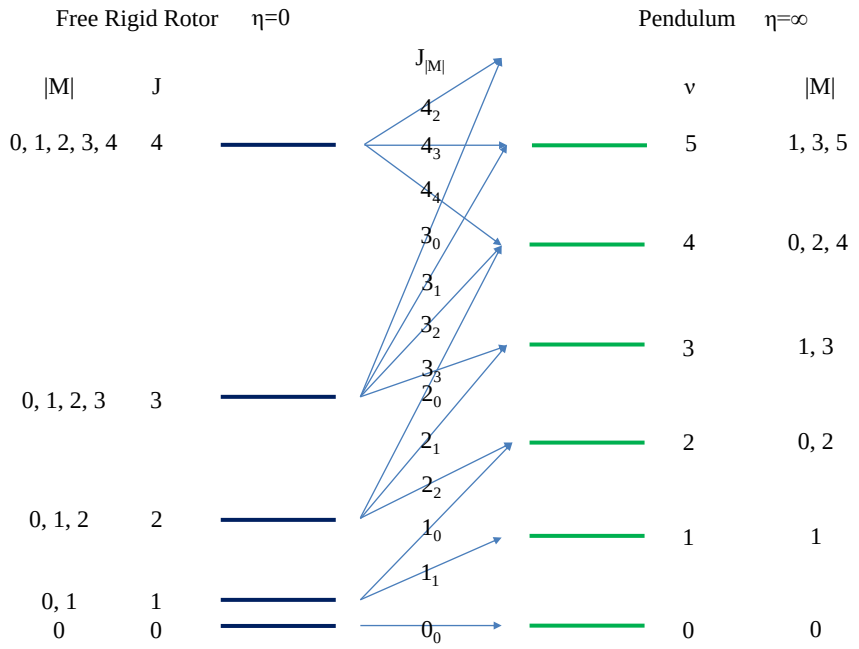

Figure 2.8: Energy level correlations between the rigid rotor system and the pendular system.

$$\nu = 2J - |M_j|, \tag{2.42}$$

which is the pendular quantum number.

In the pendular system, J is not a good quantum number anymore, but M_j is still a good quantum number. Correspondingly, the selection rules $\Delta J = \pm 1$ are not valid anymore. But the selection rules $\Delta M_j = 0, \pm 1$ are still valid. According to equation 2.41 and equation 2.42, two different rotational states with different rotational energies may have the same energy in pendular system. For example, both the rotational state $J = 2$, $M_j = 2$ and $J = 1$, $M_j = 0$ correspond to the $\nu = 1 \cdot 2 - 0 = 2$ pendular state. Their separated energy levels will merge together after adding an electric field. The correlations between the energy levels of the

rigid rotor system ($\eta = 0$) and the pendular system ($\eta = \infty$) are shown in figure 2.8. Another important feature generated by equation 2.42 is when ν is an odd number, there are no even M_j sublevels. When ν is an even number, there are no odd M_j sublevels.

From equation 2.41, the energy difference between two adjacent pendular states is $(2\eta)^{1/2}B$, where $\eta = \mu \cdot \epsilon / B$. If we increase the strength of the electric field, different pendular states are more separated energetically. In spectra, the corresponding molecular signal will be broader. This gives us a way to derive the dipole moment of the Rydberg molecule. By adding different electric fields, we measured the line broadening of the molecular signal and extracted the dipole moments of the Cs "trilobite" molecules in 2015 [12].

2.3.5 Isotropic and Anisotropic Polyatomic Rydberg Molecules

Because a highly excited Rydberg electron has an enormous orbit, it is not hard to imagine that there may be more than one ground state atom within the orbit of the Rydberg electron when the atom number density of a cold atomic gas is high enough. Experiments investigating this interesting topic have been conducted and the results have been reported and discussed [7, 17, 20, 24, 25, 48]. With different atom number densities and different n, the average number of ground state atoms within the orbit of the Rydberg electron can range from less than one to several thousand. In this situation, the Rydberg electron interacts with each of the ground state atoms. Since different ground state atoms are far away from each other, their weak interactions are negligible. The relation between the

total binding energy and each scattering process depends on the wavefunction of the Rydberg electron.

When the Rydberg electron is in an isotropic s angular momentum state, the probability distribution of the Rydberg electron is spherically symmetric. The Rydberg electron has equal chance to interact with each ground state atom. There is no correlation between different ground state atoms. The total binding energy is a summation of the binding energy of each individual scattering process. The polyatomic Rydberg molecule in this case is called an isotropic polyatomic Rydberg molecule.

When the Rydberg electron is in an $l > 0$ angular momentum state, its probability distribution is not spherically symmetric anymore. Spatial correlation can be established due to the anisotropic probability distribution of the Rydberg electron. The polyatomic Rydberg molecule in this case is called an anisotropic polyatomic Rydberg molecule.

To illustrate these two different cases, we use triatomic Rydberg molecules to study the interaction between a Rydberg electron and two ground state atoms. Considering two ground state atoms at $\mathbf{R}_1$ and $\mathbf{R}_2$, by treating them as identical particles, the wavefunctions of the triatomic Rydberg molecule are

$$\begin{aligned} \Psi_+(\mathbf{r}, \mathbf{R_1}, \mathbf{R_2}) &= A_+(\mathbf{R_1}, \mathbf{R_2})[\Psi_1(\mathbf{r}, \mathbf{R_1}) + \Psi_2(\mathbf{r}, \mathbf{R_2})] \quad \text{(even parity)}, \\ \Psi_-(\mathbf{r}, \mathbf{R_1}, \mathbf{R_2}) &= A_-(\mathbf{R_1}, \mathbf{R_2})[\Psi_1(\mathbf{r}, \mathbf{R_1}) - \Psi_2(\mathbf{r}, \mathbf{R_2})] \quad \text{(odd parity)}, \end{aligned} \tag{2.43}$$

where $A_\pm$ are normalization coefficients. $\Psi_1(\mathbf{r}, \mathbf{R_1})$ and $\Psi_2(\mathbf{r}, \mathbf{R_2})$ are the wave-

functions of the Rydberg dimers,

$$\Psi_i(\mathbf{r}, \mathbf{R}_i) = \sum_m \psi_{nlm}(\mathbf{R}_i)^* \psi_{nlm}(\mathbf{r}), \tag{2.44}$$

where $\psi_{nlm}(\mathbf{r})$ is the unperturbed Rydberg electron's wavefunction in the Coulomb potential. The potential energy curves for the even parity state and the odd parity state are [23]

$$\begin{aligned} E_{\pm}(\mathbf{R}_1, \mathbf{R}_2) = E_0 + \frac{2\pi a_1 g_{11} + 2\pi a_2 g_{22}}{2} \\ \pm \frac{1}{2}\sqrt{(2\pi a_1 g_{11} - 2\pi a_2 g_{22})^2 + 16\pi^2 a_1 a_2 g_{12} g_{21}}, \end{aligned} \tag{2.45}$$

where E_0 is the energy of the unperturbed Rydberg electron in the Coulomb potential. a_i is the s-wave triplet scattering length. And

$$g_{ij} = \sum_{n,l,m} \psi^*_{nlm}(\mathbf{R}_i) \psi_{nlm}(\mathbf{R}_j). \tag{2.46}$$

The cross term g_{ij} is a sum of different principal quantum number states n, angular momentum states l, and their projections on the internuclear axis m. Since the Rydberg atom has fixed n and l, the cross term g_{ij} is a sum of m. Depending on whether m is fixed or not, there are two different kinds of polyatomic Rydberg molecules, isotropic polyatomic Rydberg molecules and anisotropic polyatomic Rydberg molecules.

When n, l, m are all fixed,

$$
\begin{aligned}
g_{11} &= \psi^*_{nlm}(\mathbf{R}_1)\psi_{nlm}(\mathbf{R}_1) \\
g_{22} &= \psi^*_{nlm}(\mathbf{R}_2)\psi_{nlm}(\mathbf{R}_2) \\
g_{12} &= \psi^*_{nlm}(\mathbf{R}_1)\psi_{nlm}(\mathbf{R}_2) \\
g_{21} &= \psi^*_{nlm}(\mathbf{R}_2)\psi_{nlm}(\mathbf{R}_1).
\end{aligned}
\tag{2.47}
$$

It can be easily shown that

$$
g_{11} \cdot g_{22} = g_{12} \cdot g_{21}. \tag{2.48}
$$

Substituting equation 2.48 into equation 2.45, we obtain

$$
\begin{aligned}
E_{\pm}(\mathbf{R}_1, \mathbf{R}_2) &= E_0 + \frac{2\pi a_1 g_{11} + 2\pi a_2 g_{22}}{2} \pm \frac{1}{2}\sqrt{(2\pi a_1 g_{11} + 2\pi a_2 g_{22})^2} \\
&= E_0 + \frac{2\pi a_1 g_{11} + 2\pi a_2 g_{22}}{2} \pm \frac{2\pi a_1 g_{11} + 2\pi a_2 g_{22}}{2}.
\end{aligned}
\tag{2.49}
$$

Writing it more explicitly,

$$
E_+ = -\frac{1}{2n^2} + 2\pi a_{\mathrm{s}}^{\mathrm{T}}(k)|\psi_{nlm}(\mathbf{R}_1)|^2 + 2\pi a_{\mathrm{s}}^{\mathrm{T}}(k)|\psi_{nlm}(\mathbf{R}_2)|^2, \tag{2.50}
$$

and,

$$
E_- = -\frac{1}{2n^2}. \tag{2.51}
$$

It turns out when n, l, m are all fixed, the total binding energy is a summation of

the binding energy from each scattering process. Different scattering processes are independent. The additive interactions with different ground state atoms can be observed using ns Rydberg molecules, because for an ns Rydberg atom, n, l, m are all fixed. This can be understood in another way. When a Rydberg electron is in an ns state, its spherically symmetric probability distribution makes it equally interact with each ground state atom, no matter what the relative positions are. This kind of polyatomic Rydberg molecule has been observed using Rb ns Rydberg molecules at the university of Stuttgart for the first time [25]. We obtained experimental spectra of isotropic polyatomic Rydberg molecules using Cs ns Rydberg molecules [48].

When $l > 0$, m is not fixed, the cross terms under the square root in equation 2.45 cannot be canceled. For example, supposing there are two angular momentum sublevels m and m',

$$\begin{aligned} g_{11} &= \psi^*_{nlm}(\mathbf{R}_1)\psi_{nlm}(\mathbf{R}_1) + \psi^*_{nlm'}(\mathbf{R}_1)\psi_{nlm'}(\mathbf{R}_1) \\ g_{22} &= \psi^*_{nlm}(\mathbf{R}_2)\psi_{nlm}(\mathbf{R}_2) + \psi^*_{nlm'}(\mathbf{R}_2)\psi_{nlm'}(\mathbf{R}_2) \\ g_{12} &= \psi^*_{nlm}(\mathbf{R}_1)\psi_{nlm}(\mathbf{R}_2) + \psi^*_{nlm'}(\mathbf{R}_1)\psi_{nlm'}(\mathbf{R}_2) \\ g_{21} &= \psi^*_{nlm}(\mathbf{R}_2)\psi_{nlm}(\mathbf{R}_1) + \psi^*_{nlm'}(\mathbf{R}_2)\psi_{nlm'}(\mathbf{R}_1). \end{aligned} \tag{2.52}$$

$g_{11} \cdot g_{22}$ equals

$$
\begin{aligned}
g_{11} \cdot g_{22} = & \psi^*_{nlm}(\mathbf{R}_1)\psi_{nlm}(\mathbf{R}_1)\psi^*_{nlm}(\mathbf{R}_2)\psi_{nlm}(\mathbf{R}_2) \\
& + \psi^*_{nlm}(\mathbf{R}_1)\psi_{nlm}(\mathbf{R}_1)\psi^*_{nlm'}(\mathbf{R}_2)\psi_{nlm'}(\mathbf{R}_2) \\
& + \psi^*_{nlm'}(\mathbf{R}_1)\psi_{nlm'}(\mathbf{R}_1)\psi^*_{nlm}(\mathbf{R}_2)\psi_{nlm}(\mathbf{R}_2) \\
& + \psi^*_{nlm'}(\mathbf{R}_1)\psi_{nlm'}(\mathbf{R}_1)\psi^*_{nlm'}(\mathbf{R}_2)\psi_{nlm'}(\mathbf{R}_2),
\end{aligned} \tag{2.53}
$$

and $g_{12} \cdot g_{21}$ equals

$$
\begin{aligned}
g_{12} \cdot g_{21} = & \psi^*_{nlm}(\mathbf{R}_1)\psi_{nlm}(\mathbf{R}_1)\psi^*_{nlm}(\mathbf{R}_2)\psi_{nlm}(\mathbf{R}_2) \\
& + \psi^*_{nlm}(\mathbf{R}_1)\psi_{nlm'}(\mathbf{R}_1)\psi^*_{nlm'}(\mathbf{R}_2)\psi_{nlm}(\mathbf{R}_2) \\
& + \psi^*_{nlm'}(\mathbf{R}_1)\psi_{nlm}(\mathbf{R}_1)\psi^*_{nlm}(\mathbf{R}_2)\psi_{nlm'}(\mathbf{R}_2) \\
& + \psi^*_{nlm'}(\mathbf{R}_1)\psi_{nlm'}(\mathbf{R}_1)\psi^*_{nlm'}(\mathbf{R}_2)\psi_{nlm'}(\mathbf{R}_2).
\end{aligned} \tag{2.54}
$$

In this case,

$$
g_{11} \cdot g_{22} \neq g_{12} \cdot g_{21}. \tag{2.55}
$$

The spatial correlations between different ground state atoms are established through the summation on m. With a further assumption $\mathbf{R}_1 = \mathbf{R}_2 = \mathbf{R}$, equation 2.45 becomes

$$
E_{\pm}(\mathbf{R}, \theta) = E_{dim}(\mathbf{R})\left[1 \pm (-\frac{1}{2} + \frac{3}{2}\cos^2\theta)\right]. \tag{2.56}
$$

The total binding energy turns out to be a function of the angle enclosed by the two ground state atoms. The polyatomic Rydberg molecules that are formed are

named anisotropic polyatomic Rydberg molecules. The nonadditive interactions with different ground state atoms were observed by us using Cs $6s + 6s + nd$ Rydberg trimers for the first time in 2018 [24]. Our experimental results are discussed in Chapter 4.

2.3.6 Summary

The scattering between a Rydberg electron and a ground state atom is a low energy scattering which can be well described by the Fermi pseudopotential. We described the Fermi pseudopotentials for s-wave scattering and p-wave scattering. They, together, give accurate calculations of Rydberg molecules. Current spectroscopic techniques allow us to resolve fine and hyperfine structures of ultralong-range Rydberg molecules. Different spin dependent relativistic effects need to be taken into account. This can give a better understanding of the spectra. The most fascinating characteristic of ultralong-range Rydberg molecules is their large permanent dipole moments, which make them behave like pendula in electric fields. The measurement of the enormous dipole moment was achieved by us for the first time in 2015. In experiments, the dipole moments of ultralong-range Rydberg molecules need to be considered since they can strongly broaden molecular signals in the residual electric fields of the experimental system. The mechanism of a Rydberg electron interacting with more than one ground state atom was described. Depending on the angular momentum states of the Rydberg electron, the scatterings between the Rydberg electron and different ground state atoms can be correlated or independent. By exciting the Cs ground state atoms

into different angular momentum states, both cases were observed and studied by us [24]. We present our experimental results in Chapter 4.

Chapter 3

Experimental Realization

3.1 Introduction

We need to bring Rydberg atoms and ground state atoms close enough to create ultralong-range Rydberg molecules efficiently. The fragile bonds generated by scattering processes make ultralong-range Rydberg molecules difficult to observe in room temperature samples of atoms. The two critical conditions to generate ultralong-range Rydberg molecules are temperature and density. Laser cooling and trapping techniques enable the generation of samples where Rydberg molecules can be observed and their properties can be explored. In this chapter, we introduce basic concepts of laser cooling and trapping. This helps to explain how to generate cold and dense atomic gases. Other details, including the high vacuum system, the two-photon transition, the photoionization and ion detection, are also described. Together the description gives an overview of the spectroscopic experiments we use to investigate ultralong-range Rydberg molecules. These methods are commonly used in atomic physics today.

3.2 Laser Cooling and Trapping

3.2.1 Magneto-optical Trap

A magneto-optical trap (MOT) consists of a laser cooling technique referred to as optical molasses with quadrupole magnetic fields. Optical molasses is

generated by three pairs of counter-propagating circularly polarized beams intersecting perpendicularly. The confinement of optical molasses comes from the scattering/dissipation force generated by photons absorbed by atoms. Since the absorption happens along the laser beam's direction, while the following spontaneous emission happens along a random direction, on average, the photons absorbed by atoms behave as a frictional force on the atoms. Here we use a two-level system as our model, the scattering force can be expressed as [42]

$$F_{\text{scattering}} = \text{photon momentum} \times \text{scattering rate}. \tag{3.1}$$

Each photon has a momentum $\hbar k$, where $\hbar$ is the reduced Planck constant, k is the wavevector of the photon. The scattering rate is $R_{\text{scattering}} = \Gamma\rho_{22}$. $1/\Gamma$ is the lifetime of the excited level. ρ_{22} is the fraction of population in the excited level of the two-level system in a steady state which we can obtain from solving the optical Bloch equations,

$$\rho_{22} = \frac{\Omega^2/4}{\delta^2 + \Omega^2/2 + \Gamma^2/4}, \tag{3.2}$$

where $\delta = \omega - \omega_0 + kv$ is the frequency difference between the laser frequency ω and the atomic transition ω_0. kv accounts for the Doppler effect generated by the motion of the atom. v is the projection of the atom's velocity along the laser's propagation direction. k is the wavevector of the laser light. Ω is the Rabi frequency. With the expression of ρ_{22} substituted in,

$$F_{\text{scattering}} = \hbar k \frac{\Gamma}{2} \frac{\Omega^2/2}{\delta^2 + \Omega^2/2 + \Gamma^2/4}. \tag{3.3}$$

The Rabi frequency and saturation intensity are related by $I/I_{\text{sat}} = 2\Omega^2/\Gamma^2$, where I is the intensity of the laser light, I_{sat} is the saturation intensity of the transition between the ground level and excited level. Substituting this relation into equation 3.3,

$$F_{\text{scattering}} = \hbar k \frac{\Gamma}{2} \frac{I/I_{\text{sat}}}{1 + I/I_{\text{sat}} + 4\delta^2/\Gamma^2}. \tag{3.4}$$

The maximum scattering force $F_{\text{max}} = \hbar k\Gamma/2$ can be reached when the intensity I of the laser goes to infinity. The maximum deceleration is

$$a_{\text{max}} = \frac{F_{\text{max}}}{m} = \frac{v_{\text{r}}}{2\tau}, \tag{3.5}$$

where m is the mass of the atom and $v_{\text{r}} = \hbar k/m$ is called the recoil velocity. $\tau = 1/\Gamma$ is the lifetime of the excited level.

Atoms in a gas move in all directions. To reduce their temperatures requires scattering forces in all three perpendicular directions. This can be realized by three pairs of counter-propagating laser beams tuned to the red side of the cooling transition. The Doppler effect leads to an increase in the frequency of the laser beam propagating in the direction opposite to the atom's velocity. It brings the laser closer to the resonance and thereby increases the rate of absorption from this beam. Meanwhile the other beam co-propagating with the atom is further off-resonant. The imbalance between scattering forces of two counter-propagating

beams makes atoms always face frictional forces no matter which directions they move towards. The cross section between six laser beams behaves like optical molasses for atoms confined within. The frictional force of the optical molasses is given by,

$$F_{\text{molasses}} = F_{\text{scattering}}(\omega - \omega_0 - kv) - F_{\text{scattering}}(\omega - \omega_0 + kv). \tag{3.6}$$

In our experiment, we use Cs $6s_{1/2}$ $F = 4$ to $6p_{3/2}$ $F = 5$ as the cooling transition with 15 MHz frequency detuning to the red. A small portion of atoms can be excited into $6p_{3/2}$ $F = 4$ state followed by a decay into $6s_{1/2}$ $F = 3$ state. This takes the atoms out of the cooling transition cycle. Another laser which is on resonance with $6s_{1/2}$ $F = 3$ to $6p_{3/2}$ $F = 4$ transition is used to put them back to the cooling transition cycle. The cooling transition is achieved using a trapping laser (Toptica DFB laser) with an output of ~ 40 mW. A small portion of this output is used to do a saturation absorption locking. The rest is amplified by a tapered amplifier (Eagleyard Photonic EYP-0850-00500-3006-CMT03) which gives ~ 100 mW, and sent to a beam splitting system to generate six circularly polarized beams. The power of each beam is adjustable. Each trapping beam has a power of ~ 12 mW with a diameter of ~ 1 cm. More details can be found in Appendices A and C. The repumping laser is a home-made diode laser. Only a small amount of power is needed to realize efficient repumping. The total power of the MOT repumping laser is ~ 6 mW. More details can be found in Appendix B.

Although optical molasses can cool down atoms, it cannot trap atoms and hold them. To trap atoms, a quadrupole magnetic field generated by a pair of anti-Helmholtz coils is needed to cooperate with the optical molasses. When the axis of a pair of anti-Helmholtz coils is along z direction, the gradient of the magnetic field of this quadrupole magnetic field is

$$\frac{\mathrm{d}B_x}{\mathrm{d}x} = \frac{\mathrm{d}B_y}{\mathrm{d}y} = -\frac{1}{2}\frac{\mathrm{d}B_z}{\mathrm{d}z}. \tag{3.7}$$

The zero point of the magnetic field is overlapped with the center of the optical molasses, where there is no net force for atoms at rest. Atoms at small distances from the center suffer both a frictional force and a restoring force

$$\begin{aligned} F_{\mathrm{MOT}} &= F^{\sigma^+}_{\mathrm{scattering}}(\omega - kv - (\omega_0 + \beta z)) - F^{\sigma^-}_{\mathrm{scattering}}(\omega - kv - (\omega_0 - \beta z)) \\ &\approx -2\frac{\partial F}{\partial \omega} kv + 2\frac{\partial F}{\partial \omega_0}\beta z \\ &\approx -\alpha v - \frac{\alpha\beta}{k} z. \end{aligned} \tag{3.8}$$

βz is the Zeeman shift at displacement z, which can be expressed as

$$\beta z = \frac{g\mu_{\mathrm{B}}}{\hbar}\frac{\mathrm{d}B}{\mathrm{d}z} z, \tag{3.9}$$

where μ_{B} is the Bohr magneton, g is the Landé factor. Here the imbalance in the radiation force generated by Zeeman effect behaves like a restoring force with a spring constant $\alpha\beta/k$.

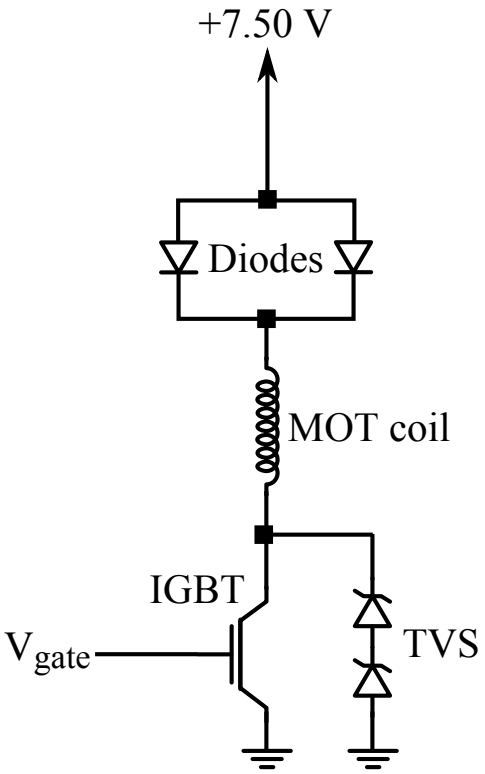

Figure 3.1: Circuit diagram for the IGBT current switch.

The anti-Helmholtz coils used to generate the quadrupole magnetic field are installed in the vacuum chamber. The coils are water-cooled copper tubes, typically carrying a current of 30 A (Lamda EMS 7.5-130 Power Supply). The coils are switched using an insulated-gate bipolar transistor (IGBT) which can turn off the magnetic field in as little as 10 μs, depending on the number of transient voltage suppressors (TVS) used in the circuit, figure 3.1. Another three pairs of Helmholtz coils in three perpendicular directions are installed outside the chamber. They can be used to compensate residual magnetic fields, such as earth field.

Under typical operating conditions, atoms in magneto-optical traps undergo over-damped harmonic motion. Magneto-optical traps are a commonly used technique to generate cold atomic gases, especially for alkali atoms where the trapping and repumping lasers have been commercialized. Further cooling can be conducted based on magneto-optical traps. It is important to characterize the cooling limit of magneto-optical traps.

A random walk of N steps gives a mean displacement proportional to $N^{1/2}$. Like Brownian motion, in time t, the spontaneous emission happens $R_{\text{scattering}}t$ times with each of them giving the atom a v_{r} recoil velocity along a random direction,

$$v_{\text{z}}^2 = \frac{1}{3}v_{\text{r}}^2 R_{\text{scattering}}t, \tag{3.10}$$

where $R_{\text{scattering}} = \Gamma\rho_{22}$ as described above. The factor 1/3 takes into account the spherically symmetric distribution of the recoil velocity and its projection on z axis. Similarly, the fluctuation of the absorption of the beams along z axis also gives

$$v_{\text{z}}^2 = v_{\text{r}}^2 R_{\text{scattering}}t. \tag{3.11}$$

There is no 1/3 factor because the influence of the fluctuation of the absorption is only along z axis.

When the kinetic energy of the cold atom does not change anymore, we reach the cooling limit,

$$\frac{\mathrm{d}}{\mathrm{d}t}(\frac{1}{2}mv_{\mathrm{z}}^2) = 2mv_{\mathrm{r}}^2 R_{\mathrm{scattering}} - \alpha v_{\mathrm{z}}^2 = 0, \tag{3.12}$$

which finally gives

$$k_{\mathrm{B}}T_{\mathrm{D}} = \frac{\hbar\Gamma}{2}. \tag{3.13}$$

k_{B} is the Boltzmann constant. T_{D} is the Doppler cooling limit which is theoretically the coolest temperature a magneto-optical trap can reach based on the idea so far presented.

However, there is another cooling process called polarization-gradient cooling or Sisyphus cooling within magneto-optical traps. It enables magneto-optical traps to reach even cooler temperatures. The standing wave in each of the three perpendicular directions formed by two counter-propagating circularly polarized laser lights have a spatially varying polarization with it. Energy levels of cold atoms within a magneto-optical trap shift periodically by this polarization-gradient of the standing wave. This finally makes the cold atoms preferentially absorb photons with smaller energies followed by emission of photons with more energies. The energy difference between the absorptions and emissions further cools down the atoms. The final temperature is related to the intensity and frequency detuning of the cooling laser light by

$$k_{\mathrm{B}}T \propto \frac{I}{|\delta|}. \tag{3.14}$$

From this equation we can see, if we want to reach a lower temperature, we can

decrease the intensity of the laser light and increase the detuning of the laser light.

In our experiment, after each 1.4 s long loading of the MOT, a 60 ms long polarization-gradient cooling is conducted, where both the powers of the trapping laser and repumping laser are attenuated a lot and the frequency of the trapping laser is shifted further to the red side of the cooling transition. The total power of the trapping laser is reduced from $\sim$ 100 mW to $\sim$ 35 mW. The power of the repumping laser is reduced from $\sim$ 6 mW to $\sim$ 50 μW. The detuning of the trapping laser from the $6p_{3/2}$ $F = 5$ state is increased from -15 MHz to -25 MHz [49, 50]. At the same time, the far-off-resonance trap is turned on. The AC Stark shift generated by the intense light of the far-off-resonance trap makes the trapping laser even more off-resonant. The polarization-gradient cooling further cools the atomic gases in the MOT from $\sim$ 125 μK down to $\sim$ 30 μK. The strong attenuation of the repumping laser passively leads all cold atoms to fall into the $6s_{1/2}$ $F = 3$ state, which is the ground state.

3.2.2 Zeeman Slower

Before loading into a magneto-optical trap, hot atoms need to be pre-cooled. At room temperature, atoms are too hot for a magneto-optical trap to capture them efficiently. For our experiment, the desired final velocity needs to be $\leqslant 30$ m s^{-1}, allowing for capture from the power-broadening molasses beams. Direct loading without any pre-cooling as in a vapor-cell MOT is possible, but the maximum density and lifetime it can realize is usually unsatisfactory, 10^{10} cm^{-3} to 10^{11} cm^{-3}, compared to 10^{12} cm^{-3} to 10^{13} cm^{-3} in a MOT loaded from a Zeeman

slower. The pre-cooling can be accomplished either by a Zeeman slower or a 2-dimensional MOT.

The maximum deceleration from a scattering force is shown in equation 3.5. The velocity of the atoms pre-cooled by a Zeeman slower is designed to be zero when the atoms get to the center of a magneto-optical trap. Therefore the length of the Zeeman slower is

$$L_0 = \frac{v_0^2}{a_{\max}}, \tag{3.15}$$

where v_0 is the initial velocity of the atom coming out from the hot oven. An issue with this cooling process is the changing velocity of the atom makes the laser light off-resonant due to the Doppler effect. This can be solved by changing a magnetic field along the Zeeman slower, which leads a shift of the energy level of the atom running along the Zeeman slower. The desired magnetic field can be calculated as [42]

$$\omega_0 + \frac{\mu_{\mathrm{B}} B(z)}{\hbar} = \omega + kv. \tag{3.16}$$

The magnetic field along the Zeeman slower can be adjusted by changing the number of turns of the wire. According to simulations, the current setup of the Zeeman slower gives a final velocity of ~ 24.28 m s^{-1}. A detailed study can be found in reference [51, 52].

In our system, one end of the Zeeman slower is connected to the main chamber by a nozzle. The other end of the Zeeman slower is connected to the Cs source.

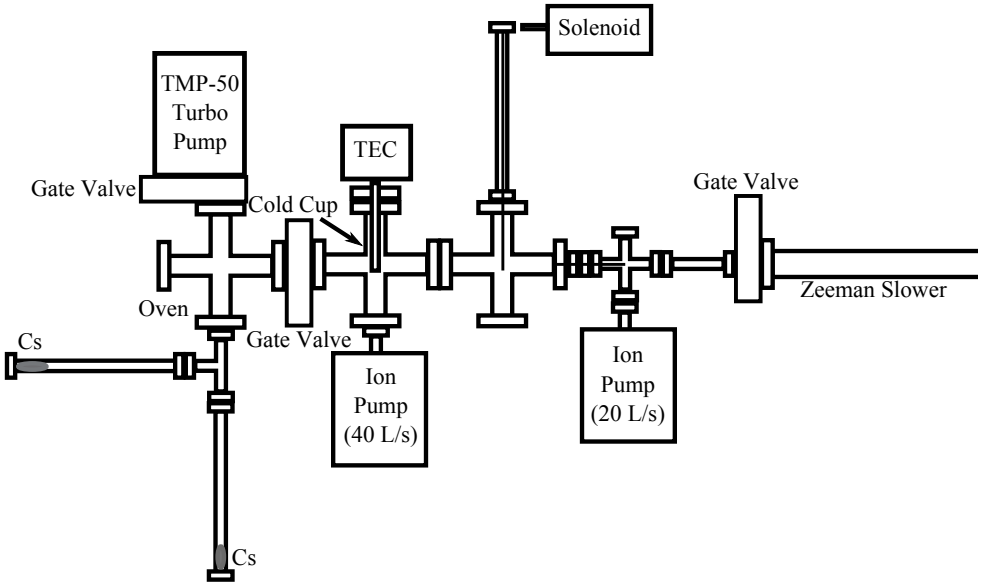

Figure 3.2: The structure of the Cs source.

The Cs source is contained in an oven with a turbo pump (Turbovac 50) used to evacuate the oven after each replacement of the Cs source. Hot Cs atoms flow towards the Zeeman slower due to thermal expansion. A pressure gradient generated by two ion pumps (Gamma Vacuum 40S; Vacion Pump 20) is used to pump out the Zeeman slower, figure 3.2. A cold cup with a tiny aperture at the center is installed to make sure pressure does not build up in the oven. The temperature of the cold cup is regulated at -10 °C using a thermo-electric cooler (TE Tech CP-036). Only atoms with low radial velocities can pass through the aperture when they arrive at the cold cup from the oven. Atoms with high radial speeds will stick on the surface of the cold cup. The Cs atoms passing through the

cold cup with well defined radial velocities are further cooled in the axial direction along the Zeeman slower. The initial axial velocity of the hot atoms coming from the oven depends on the temperature of the oven. For $T = 323$ K, $v = 226$ m/s.

3.2.3 Far-off-resonance Trap

Atoms can be polarized by electromagnetic fields. The induced atomic dipole moment $\mathbf{p}$ oscillates at the driving frequency ω. The electric field of laser light can be expressed as $\mathbf{E}(\mathbf{r},t) = \hat{\mathbf{e}}\tilde{E}(\mathbf{r})\exp(-i\omega t) + c.c.$, and $\mathbf{p}(\mathbf{r},t) = \hat{\mathbf{e}}\tilde{p}(\mathbf{r})\exp(-i\omega t) + c.c.$, where $\hat{\mathbf{e}}$ indicates the polarization direction of the electric field. The amplitude of the dipole moment $\tilde{p}$ can be simply related to the field amplitude $\tilde{E}$ by [53]

$$\tilde{p} = \alpha\tilde{E}. \tag{3.17}$$

Here α is the complex polarizability, which depends on the driving frequency ω. The induced dipole moment can in turn interact with the electromagnetic field. This interaction can be described by

$$U_{\text{dipole}} = -\frac{1}{2} < \mathbf{pE} >= -\frac{1}{2\epsilon_0 c}\text{Re}(\alpha)I. \tag{3.18}$$

The angular brackets denote the time average over the rapid oscillating terms, the field intensity is $I = 2\epsilon_0 c|\tilde{E}|^2$, and the factor $1/2$ takes into account that the dipole moment is induced, not permanent. The dipole force is the gradient of the interaction potential

$$\mathbf{F}_{\text{dipole}}(\mathbf{r}) = -\nabla U_{\text{dipole}}(\mathbf{r}) = \frac{1}{2\epsilon_0 c}\text{Re}(\alpha)\nabla I(\mathbf{r}), \tag{3.19}$$

where we can see the dipole force is a conservative force, which is proportional to the intensity gradient of the driving field. The corresponding scattering rate is

$$R_{\text{scatter}}(\mathbf{r}) = \frac{1}{\hbar\epsilon_0 c}\text{Im}(\alpha)I(\mathbf{r}). \tag{3.20}$$

With a more explicit expression of the complex polarizability α [53] substituted in and using the rotating-wave approximation, the dipole potential and scattering rate can be written as

$$U_{\text{dipole}}(\mathbf{r}) = \frac{3\pi c^2}{2\omega_0^3}\frac{\Gamma}{\Delta}I(\mathbf{r}). \tag{3.21}$$

$$R_{\text{scatter}}(\mathbf{r}) = \frac{3\pi c^2}{2\omega_0^3}(\frac{\Gamma}{\Delta})^2 I(\mathbf{r}). \tag{3.22}$$

$\Delta = \omega - \omega_0$, ω is the frequency of the electromagnetic field and ω_0 is the transition frequency of the atom. $1/\Gamma$ is the lifetime of the excited level. Depending on the laser frequency, we have two different types of optical dipole traps: blue detuned dipole traps, $\omega > \omega_0$, where all atoms are confined at positions with minimum intensity; and red detuned dipole traps, $\omega < \omega_0$, where all atoms are confined at positions with maximum intensity.

For alkali atoms the dipole trap potential can be written as

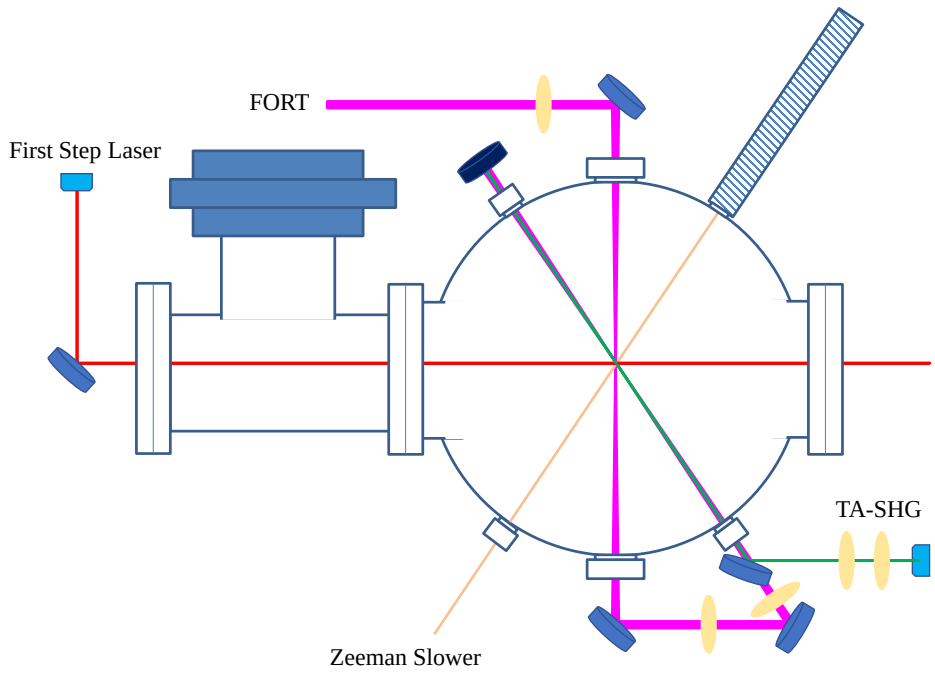

Figure 3.3: The diagram of relative positions of different optical beams inside the chamber.

$$U_{\text{dipole}}(\mathbf{r}) = \frac{3\pi c^2}{2\omega_0^3}\left(\frac{2+\mathbb{P}g_F m_F}{\Delta_{F=3}} + \frac{1-\mathbb{P}g_F m_F}{\Delta_{F=4}}\right) I(\mathbf{r}), \tag{3.23}$$

where F and m_F are the total angular momentum quantum number and the magnetic quantum number of the specified ground state. g_F is the Landé factor. $\mathbb{P} = 0, \pm 1$ correspond to linearly and circularly polarized light. The detunings $\Delta_{F=3}$ and $\Delta_{F=4}$ refer to the energy splitting between the particular ground state $6s_{1/2}$ $F = 3, 4$ and the center of the $6p_{3/2}$ and $6p_{1/2}$ excited states, respectively.

To realize a deep trap with a smaller scattering rate, we usually use a far detuned laser with a very high intensity. In our experiment, we use a diode-pumped ytterbium fiber laser (IPG YLR-50-1064-LP) to generate a crossed far-off-resonance trap, where 50 means the maximum output power is 50 W, 1064

means the wavelength is 1064 nm, and LP means it is linearly polarized. Using a dichroic mirror, the fiber laser beam is transported to the chamber by overlapping it with one of the MOT trapping beams. Before the dichroic mirror, a positive lens is used for collimating the fiber laser beam. After passing through the chamber, the fiber laser beam is collimated again by another positive lens, and reflected back through the chamber to cross the original beam. In this way, we cross the two fiber laser beams at a 22.5° angle with their focuses overlapping, see figure 3.3. The beam waist of each beam is 98 ± 1 μm. The aspect ratio of the cross section is $\sim 2:1$. The trap frequencies are $2\pi \times 3.58$ kHz radially and $2\pi \times 1.0$ kHz axially. The trap depth is ~ 5 mK.

3.2.4 Characterization of Cold Atoms in Far-off-resonance Traps

The two most important parameters for cold atoms in a far-off-resonance trap are temperature and maximum atom number density. In a given potential $U(\mathbf{r})$, the thermal density distribution $n(\mathbf{r})$ directly follows from the Boltzmann factor,

$$n(\mathbf{r}) = n_0 \exp\left[-\frac{U(\mathbf{r})}{k_{\mathrm{B}}T}\right], \tag{3.24}$$

where n_0 is the maximum atom number density, T is the temperature of the cold atomic gas, and k_{B} is the Boltzmann constant. The temperature T can be derived from the measurement of the spatial distribution of the atom number density in the FORT. If the trap potential is harmonic in all directions, the atom number density is a Gaussian distribution in all directions,

$$n(\mathbf{r}) = n_0 \exp(-\frac{x^2}{2\delta_x^2}) \exp(-\frac{y^2}{2\delta_y^2}) \exp(-\frac{z^2}{2\delta_z^2}), \tag{3.25}$$

where $\delta_i = \omega_i^{-1}\sqrt{k_{\mathrm{B}}T/m}$ is the standard deviation of the Gaussian distribution. It is related to the full width at half maximum (FWHM) of the Gaussian distribution. Thus δ_i can be obtained using absorption imaging. m is the mass of the cold atom. ω_i is the trap frequency along each direction, which can be calculated by knowing the parameters of the FORT. The temperature can be obtained as

$$T = \frac{m}{k_{\mathrm{B}}} \delta_i^2 \omega_i^2. \tag{3.26}$$

The temperature can also be measured by observing the thermal expansion of cold atoms after releasing them from far-off-resonance traps. The maximum atom number density, spatial density distribution and thermal expansion can be measured by various imaging methods, for example, absorption imaging or fluorescence imaging. Among these methods, absorption imaging gives the most reliable results. Using a CCD camera and a simple imaging optical setup, see figure 3.4, we can obtain an image of the optical density of a cold atomic gas. This optical density can be further used to obtain the atom number density.

The optical density can be represented as

$$D(x,y) = -ln\frac{I(x,y)}{I_0(x,y)} = -ln\frac{I_{abs} - I_{bg}}{I_{ff} - I_{bg}}, \tag{3.27}$$

where I_0 is the intensity of the imaging light before the cold atomic gas. I is the intensity of the imaging light after the cold atomic gas. I_{abs} is the transmission

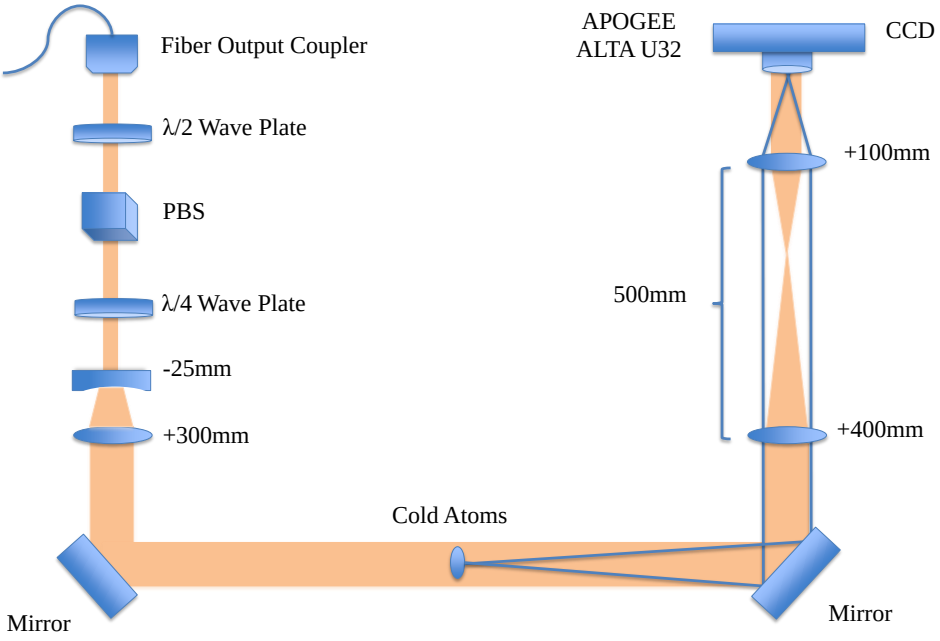

Figure 3.4: The absorption imaging setup.

intensity after absorption by cold atoms in FORT. I_{bg} is the background intensity without cold atoms, the imaging beam is off, the FORT is on. I_{ff} is the intensity of the imaging beam without cold atoms, and the FORT is on. The optical density can be related to column number density by Beer's law

$$D(x,y) = \sigma \int n(x,y,z)\mathrm{d}z = \sigma \tilde{n}(x,y), \tag{3.28}$$

where $n(x,y,z)$ is the atom number density of cold atoms, $\tilde{n}(x,y)$ is the column number density of cold atoms and σ is the absorption cross section. The results of different imaging stages and the final optical density of the cold atoms are shown in figure 3.5.

To image a cold atomic gas in a FORT, a well collimated imaging beam with

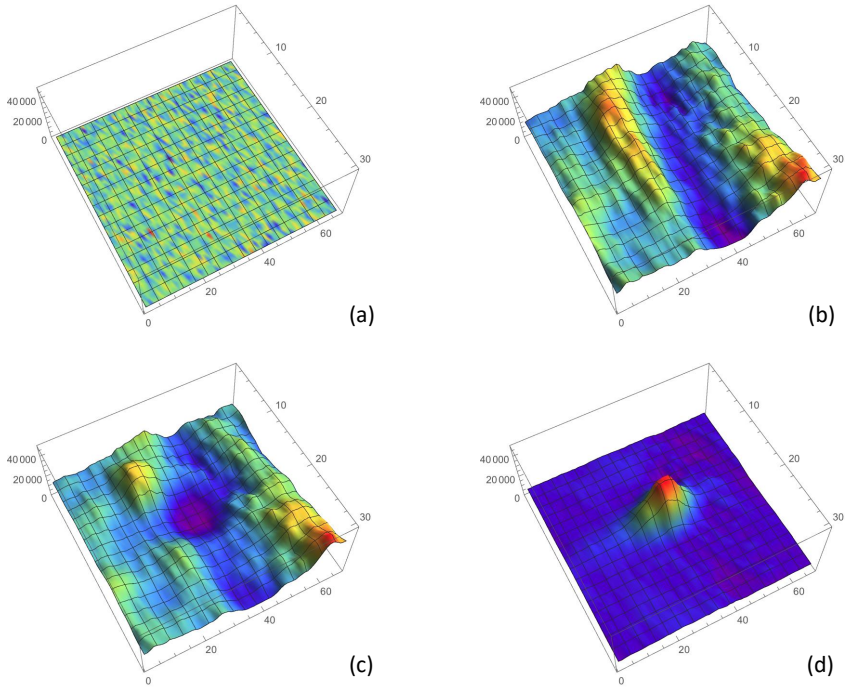

Figure 3.5: Imaging results of different stages during an absorption imaging measurement. (a) is the background intensity I_{bg}, (b) is the intensity of the imaging light I_{ff}, (c) is the transmission intensity after absorption by cold atoms I_{abs}, (d) is the optical density of the cold atoms.

a well defined polarization is guided into the chamber and projected on the cold atomic gas. After passing through the cold atoms, the imaging beam is collected by an optical imaging system consisting of two positive lenses with focuses f_1 and f_2. The magnification of the optical imaging system is

$$m = -\frac{f_2}{f_1}. \tag{3.29}$$

By knowing the array size (how many pixels) and the pixel size of a CCD camera, we can derive the actual size of the cold atomic gas and the spatial distribution of the atom number density. Since the spatial distribution of the atom number density in a 3D harmonic far-off-resonance trap is a Gaussian

distribution, the maximum density can be derived directly

$$\begin{aligned} D(x_0, y_0) &= \sigma \int n(x_0, y_0, z)\mathrm{d}z \\ &= \sigma \int n(x_0, y_0, 0) e^{-\frac{z^2}{2\delta^2}} \mathrm{d}z \\ &= \sigma \; n(x_0, y_0, 0) \; \sqrt{\pi} \; \sqrt{2} \; \delta, \end{aligned} \tag{3.30}$$

where the standard deviation δ of the Gaussian distribution is related to the linewidth

$$\delta = \frac{\mathrm{FWHM}}{2\sqrt{2ln2}}. \tag{3.31}$$

The absorption cross section can be expressed as

$$\sigma = \frac{\sigma_0}{1 + 4(\Delta/\Gamma)^2 + I/I_{sat}}, \tag{3.32}$$

where Δ is the imaging laser detuning from resonance, Γ is the lifetime of the excited state, I is the intensity of the imaging light, I_{sat} is the saturation absorption intensity and σ_0 is the resonance scattering cross section, which is defined as

$$\sigma_0 = \frac{\hbar w \Gamma}{2I_{sat}}. \tag{3.33}$$

ω is the frequency of the imaging laser. I_{sat} can be represented as

$$I_{sat} = \frac{c\epsilon_0 \Gamma^2 \hbar^2}{4|\hat{\boldsymbol{\epsilon}} \cdot \mathbf{d}|^2}, \tag{3.34}$$

where ϵ_0 is the vacuum dielectric constant. $\hat{\boldsymbol{\epsilon}}$ is an unit vector which indicates the polarization direction of the imaging laser beam. $\mathbf{d}$ is the electric dipole moment of the atom.

3.3 Ultrahigh Vacuum Chamber and Fail-safe System

Ultrahigh vacuum (UHV) environments are a critical technique for cold atomic experiments. To obtain cold atomic gases with high densities, a low background loss is necessary. To get a high vacuum, a three tier vacuum pump system is installed in our experiment, figure 3.6. The main chamber is directly pumped by a Leybold TMP 350M turbo molecular pump. It is backed by the second pump which is a Varian M2 diffusion pump. A Leybold D65B rotary vane mechanical pump works as the backing pump for the diffusion pump. The Leybold TMP 350M turbo molecular pump can also be switched to be backed by the Leybold D65B rotary vane mechanical pump directly. In addition, a non-evaporable getter (NEG) pump, SAER CapaciTorr 400-2, is installed in the chamber directly as a supplement to the main pumping system. Several gate valves are installed between different pumps.

A programmable logic controller (PLC) is used to monitor the vacuum system. It accepts input from various sources and from a touch panel display. We can use the touch panel to turn the pumps on/off, and open/close the valves. Different buttons on the display modify variables in the memory of the touch panel which are linked to the memory address in the PLC. The interface on the panel display

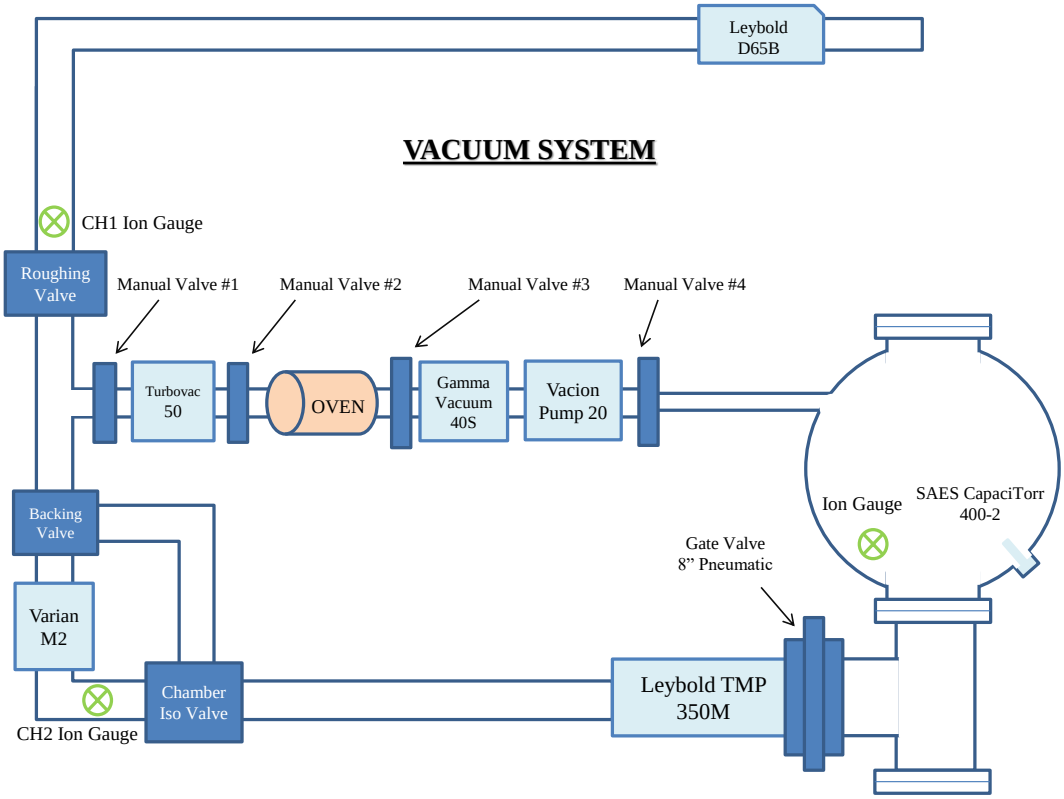

Figure 3.6: The diagram of the vacuum system.

can be designed using a program available from the manufacture called "C-More". The PLC, touch panel display, different gate valves, and the Leybold TMP 350M turbo molecular pump have two back-up batteries as a fail-safe power supply. This is to make sure when a power outage happens, the whole system can transfer into a default state which protects the vacuum in the chamber.

The program on the PLC is controlled by another program called "DirectSoft32" on a remote computer connected to the PLC through a serial cable connection. Once connected, the program on the PLC is shown on the computer and its status can be observed. Each line of the program consists of a series of relays which must be "on" for the output address to turn on. There are two kinds of relays:

"normally open" and "normally closed". "Normally open" relays are on when the address associated with them is on (for example when an input port is receiving a voltage), and off when the address associated with them is off (when the input port is not receiving a voltage). "Normally closed" relays function the opposite way: they are on when the address associated with them is off and vice versa.

3.4 Two-photon Excitation

We use two-photon transitions to photoassociate ultralong-range Rydberg molecules [54]. Different transitions and energy levels used in our experiment are shown in figure 3.7. The Cs atoms are excited from the ground state, $6s_{1/2}$ $F = 3$, to Rydberg states using a near resonant transition to $6p_{3/2}$ $F = 4$ at ~ 852 nm. This first step of the excitation is detuned from the resonance by 300 MHz. Both the first step laser and the Rydberg excitation laser (TA-SHG) ~ 508 nm are locked to an ultralow-expansion (ULE) Fabry-Pérot cavity using the Pound-Drever-Hall (PDH) technique [55, 56]. Each laser has a linewidth ~ 30 kHz. They are linearly polarized in the same direction. The first step laser crosses the first pass of the FORT beam perpendicularly with a beam waist of ~ 1 mm and a power of ~ 4 mW. The Rydberg excitation laser co-propagates with the second pass of the FORT beam with a beam waist of ~ 75 μm and a power of ~ 70 mW. The excitation strength to a Rydberg state can be expressed as the total Rabi frequency of the two-photon transition

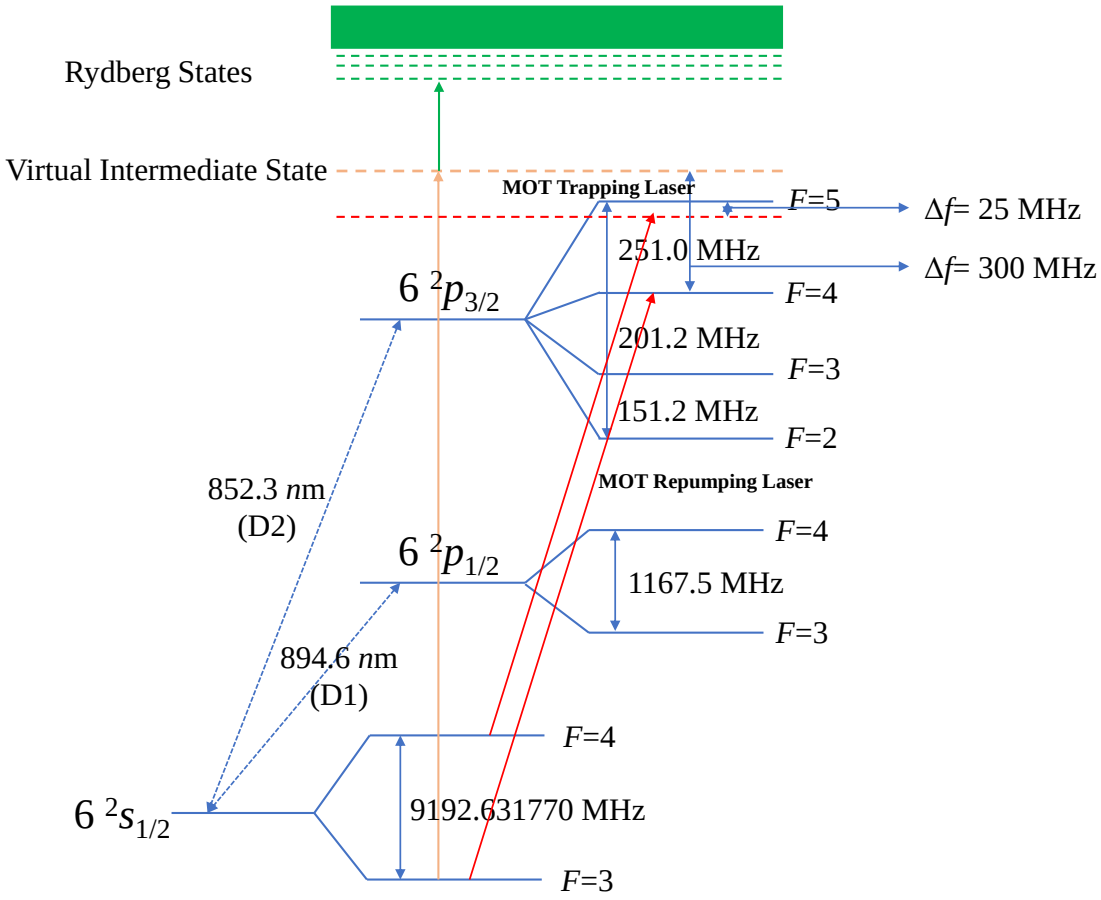

Figure 3.7: Energy levels of Cs atoms and different transitions we use in experiments.

$$\Omega_{ac} = \frac{\Omega_{ab} \cdot \Omega_{bc}}{4\pi\Delta}, \tag{3.35}$$

where Δ is the detuning of the laser from the intermediate state, which is 300 MHz. Each Rabi frequency is defined as

$$\Omega_{ab} = \frac{< a \ |e\mathbf{r} \cdot \mathbf{E}_0| \ b >}{\hbar} = \frac{e}{\hbar} \int \psi_a^*(r)\mathbf{r} \cdot \mathbf{E}_0 \psi_b(r) \mathrm{d}^3\mathbf{r} \tag{3.36}$$

$$\Omega_{bc} = \frac{< b \ |e\mathbf{r} \cdot \mathbf{E}_0'| \ c >}{\hbar} = \frac{e}{\hbar} \int \psi_b^*(r)\mathbf{r} \cdot \mathbf{E}_0' \psi_c(r) \mathrm{d}^3\mathbf{r} \tag{3.37}$$

where $\mathbf{E}_0$ and $\mathbf{E}_0'$ are the amplitudes of the electric fields of the first step laser and Rydberg excitation laser. The two-photon transition can excite Cs atoms from the ground state to Rydberg ns states and Rydberg nd states. The total Rabi frequency is around several hundred Hz to several kHz depending on the Rydberg state we excite and the experimental conditions we use. A detailed description of the setup of the two-photon excitation is found in Appendix D.

3.5 Rydberg Ionization and Detection

To count the number of the Rydberg molecules created in an experiment, we ionize Rydberg molecules and detect them using a multichannel plate detector (MCP). Rydberg atoms and Rydberg molecules can be ionized using either photoionization or pulsed electric field ionization (PFI). The generated ions are projected on to the multichannel plate detector by electric field pulses. The voltage on the MCP is -5 kV and each hit from one ion can generate a small voltage pulse. The number of voltage pulses are counted by a multichannel analyzer (MCA) card (FastComTec P7886) with a 500 ps resolution.

The threshold field for electric field ionization of Rydberg atoms as a function of the principal quantum number n is

$$E = \frac{1}{9n^4}. \tag{3.38}$$

The electric field is generated by two parallel plates separated by 4.5 cm. The corresponding voltages to ionize Rydberg atoms in different Rydberg states can be

calculated using equation 3.38. The electric voltage is supplied by a Glassman EK high voltage power supply in conjunction with a DEI PVX-4140 pulse generator. The repetition rate of the electric field pulse is limited by the power that can be dissipated on the resistors in the chamber. The combined resistance of the system is 3 kΩ and it can only dissipate 0.125 W. The relation between the dissipation power P, resistance R, voltage V, and repetition rate f can be expressed as

$$P = \frac{V^2}{R}\tau f, \tag{3.39}$$

where τ is the length of each pulse.

Rydberg atoms can also be photoionized by our FORT beam directly. The energy required to ionize a Rydberg atom $\sim 10^{-2}$ eV is less than the energy provided by a photon from the FORT beam of 1064 nm $\sim$ 1.17 eV. Compared to pulsed field ionization, photoionization has a lower efficiency $\sim 50\%$, as not all the atoms are ionized at the same time. Detailed studies of photoionization of Rydberg atoms have been given in Chapter 2.

3.6 Experimental Timing and Data Collection

The typical period of the experiment is 2 s. As shown in figure 3.8, it consists of a 1.4 s loading period of the MOT followed by a 60 ms long polarization-gradient cooling. 20 ms after the polarization-gradient cooling, a 10 μs long excitation, where both the first step laser and Rydberg excitation laser are turned on simultaneously, repeats every 500 μs. It repeats 1000 times within 500 ms. 500

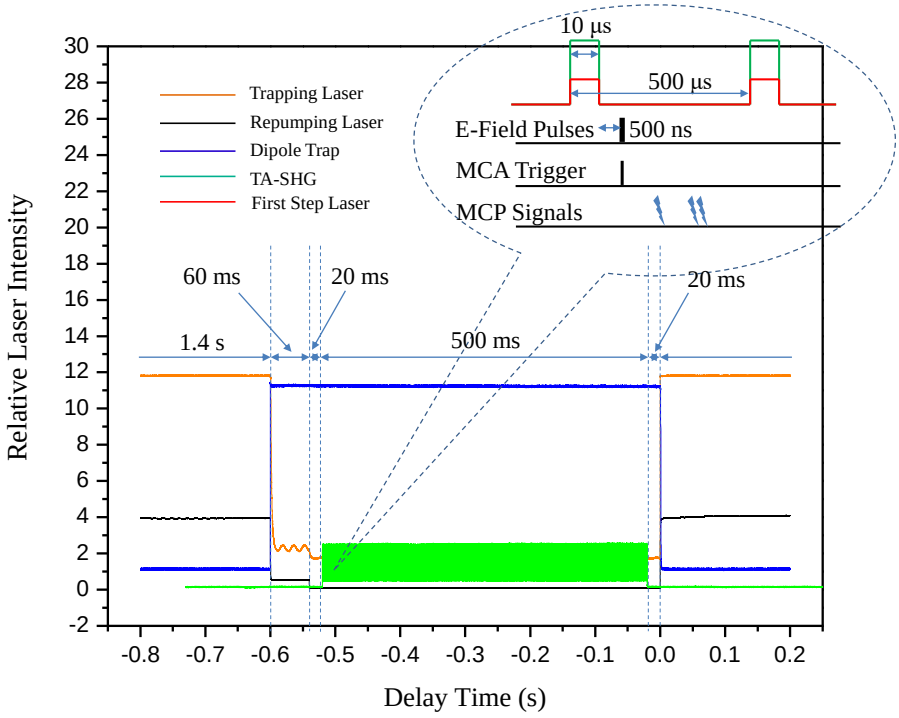

Figure 3.8: Experimental time sequences.

ns after each excitation, a short electric field pulse is turned on for 500 ns. The electric field pulse extracts all ions to the multichannel plate detector.

The complex experimental sequences are accomplished using three different timing controllers. The master timing for the experiment comes from an SRS DG535 digital pulse generator. It is driven by a crystal oscillator which has a center frequency 10 MHz and 25 ppm variation. The resolution is 5 ps. The SRS DG535 digital pulse generator is the most accurate sequence generator with the highest resolution in our system. All micro-timings are controlled by it, for example, the excitation laser's turning on/off and the short electric field pulses used for extracting ions.

There are five delay output BNCs: T0, A, B, C and D, where T0 is the mark of the beginning of the time interval. A, B, C and D can be set from 0 to 1000 s

in 5 ps increments with respect to T0. The output signal can be in TTL, NIM, ECL or adjustable level forms. They can drive 50 Ω or high impedance loads. There are another four pulse output BNCs : AB, -AB, CD and -CD. AB and CD provide pulse intervals with high voltages between A and B, C and D respectively. -AB and -CD provide pulses with low voltages. We use the SRS DG535 digital pulse generator in burst mode. The rate is 2000 Hz with 1000 pulses and 4000 periods. This gives us 1000 pulses every 2 seconds with each pulse 500 μs long. This timing structure is the basic time sequence of our experiment as described at the beginning of this section.

A Thorlabs DG100N digital generator driven by the SRS DG535 is used as the second order timing system. Internal triggers or external triggers can be up to 1 MHz with 50 ppm. Each delay/gate can be set with a 25 ns resolution. It has six outputs, which can be triggered by the master trigger input or be triggered by an individual trigger input. When we want some functions to be turned on/off with certain delays after some other functions triggered by the SRS DG535, we can use the Thorlabs DG100N to trigger these functions.

The last order timing system is a custom program written in C++ for a National Instruments board (NI-DAQ) which is triggered by the Thorlabs DG100N. It has 8 digital outputs and 2 analog outputs. The board has a time resolution ~ 10 μs. The outer frame of the experimental sequence is defined by the NI-DAQ, for example, the length of the MOT loading. Although as the root of all triggers, the SRS DG535 sends a trigger every 2 seconds, the period of the experiment set by this custom program is 4 seconds. It consists of two 2 seconds long parts with the

second part currently set as a repeat of the first part. The second trigger sent by the SRS DG535 in the second 2 seconds is blocked by the Thorlabs DG100N without sending to the NI-DAQ. This setup is very useful when we need to do two different detections alternately, for example, a normal FORT scan followed by a MOT scan.

Detailed setup of different time sequencers is shown in Appendix E.

Chapter 4

Isotropic and Anisotropic Polyatomic Rydberg Molecules

4.1 Introduction

Since the radius of a Rydberg electron's orbit increases as $a_0 n^2$, the number of ground state atoms interacting with a Rydberg electron can be manipulated through changing the radius by changing n. This ability makes Rydberg molecules excellent systems for investigating both few-body physics and many-body physics. It is very interesting to investigate in what manner the Rydberg electron interacts with different ground state atoms. In cold atomic gases, different ground state atoms are far away from each other. The weak interactions between them can be ignored. When the Rydberg electron is in an ns state, its probability distribution is isotropic and the total binding energy is a summation of binding energies from the interaction with each ground state atom. Experimental evidence supporting this result has been reported for Rb [7, 25], Sr [20] and Cs [48]. When the Rydberg electron is in an nd or higher angular momentum state, its probability distribution is anisotropic and the total binding energy depends on the relative positions of different ground state atoms. The nonadditive effect has been first observed and reported by us using Cs $6s + 6s + nd$ triatomic Rydberg molecules [24]. The simulated spectra, combining both dimer and nonadditive trimer states, agree with our experimental measurements much better than spectra that only include

dimer states. In this chapter, we present the results of our work on few-body and many-body physics of Rydberg molecules. Depending on the angular momentum states of the Rydberg molecules, we observed both additive and nonadditive interactions between Rydberg electrons and ground state atoms.

4.2 Isotropic Polyatomic Rydberg Molecules

Theoretical study of the interaction between one Rydberg electron and many ground state atoms has been discussed in Chapter 2. When a Rydberg electron is in an ns state, the total binding energy is a summation of the binding energy of each individual scattering process

$$E = -\frac{1}{2n^2} + 2\pi a_{\rm s}^{\rm T}(k)|\psi_{n,0,0}(\mathbf{R}_1)|^2 + 2\pi a_{\rm s}^{\rm T}(k)|\psi_{n,0,0}(\mathbf{R}_2)|^2 + \cdots . \tag{4.1}$$

The first term on the right side of the equation is the energy of the Rydberg electron in the Coulomb potential. Each following term represents the binding energy from each s-wave triplet scattering process. In this situation, different scattering processes are independent. This can be understood intuitively. Considering the atom number density of our cold atomic gas, on average, different ground state atoms are far away from each other. Their weak interactions can be ignored. The chance to have two ground state atoms close enough to each other that the interaction between them cannot be ignored is very small. The probability distribution of a Rydberg electron in an ns state is spherically symmetric. This

means no matter what the relative positions of the ground state atoms are, the Rydberg electron has the same probability to be scattered by each ground state atom in the same way. Hence the total binding energy is a summation of binding energies from different scattering processes.

The probability to find a ground state atom at a distance R away from the Rydberg ion core scales with the area of the sphere centered on the Rydberg ion core with radius R, which can be expressed approximately as $4\pi \mathrm{R}^2 \Delta \mathrm{R}$. Therefore the probability to find N ground state atoms at distances R_1, R_2, ..., R_N scales as $(\mathrm{R}_1 \cdot \mathrm{R}_2 \cdot ... \cdot \mathrm{R}_N)^2$. This means the dominant molecular signals are the ground molecular states in the outer-most potential wells, where the internuclear distance R_0 is the largest. Experimental signals of polyatomic molecular states with short bond lengths are suppressed. Equation 4.1 changes to be

$$\begin{aligned} E &= -\frac{1}{2n^2} + \sum_{i=1}^{N} 2\pi a_{\mathrm{s}}^{\mathrm{T}}(k) |\psi_{n,0,0}^2(\mathbf{R}_0)|^2 \\ &= -\frac{1}{2n^2} + N \times 2\pi a_{\mathrm{s}}^{\mathrm{T}}(k) |\psi_{n,0,0}^2(\mathbf{R}_0)|^2. \end{aligned} \tag{4.2}$$

From this equation, we expect to observe a series of molecular signals evenly distributed on the red side of the Rydberg transition line in an experiment. Each order of the molecular signals corresponds to isotropic polyatomic Rydberg molecules with a certain number N of ground state atoms. The frequency difference between two adjacent molecular signals is the binding energy of the Rydberg dimer, and the total binding energy of the polyatomic Rydberg molecule is a

multiple of it.

With the atom number density fixed, more and more ground state atoms are within the orbital of the Rydberg electron as n increases. Higher orders of polyatomic Rydberg molecular signals, with more ground state atoms interacting with the Rydberg electron, can be obtained as we go to higher n Rydberg states. At the same time, the depth of potential energy curves decreases as n increases. Frequency differences between different orders of polyatomic Rydberg molecular signals are smaller and smaller. Different polyatomic Rydberg molecular signals tend to get close to each other energetically. In the limit of large numbers, the states blur together and cannot be distinguished in experimental spectra.

In a cold atomic gas with a certain atom number density, an ns state Rydberg atom on average has a certain number $\bar{N}$ of ground state atoms within the orbital of the Rydberg electron. This means polyatomic Rydberg molecules with a certain number $\bar{N}$ of ground state atoms have the largest chance to be created, which gives the strongest molecular signal in the spectra. This number can be calculated by knowing the maximum density n_0 of the cold atomic gas and the geometric volume of the Rydberg atom $V_{n,l}$,

$$\bar{N} = n_0 \cdot V_{n,l} = n_0 \, \frac{4}{3} \, \pi \left\{ \, \frac{1}{2} \left[\, 3n^2 - l \, (\, l + 1 \,) \, \right] \right\}^3 , \tag{4.3}$$

where n is the principal quantum number and l is the angular momentum quantum number. For example, a cold atomic gas with a maximum density of $\sim 5 \times 10^{12}$ cm^{-3}, has on average three ground state atoms within the orbit of the Rydberg

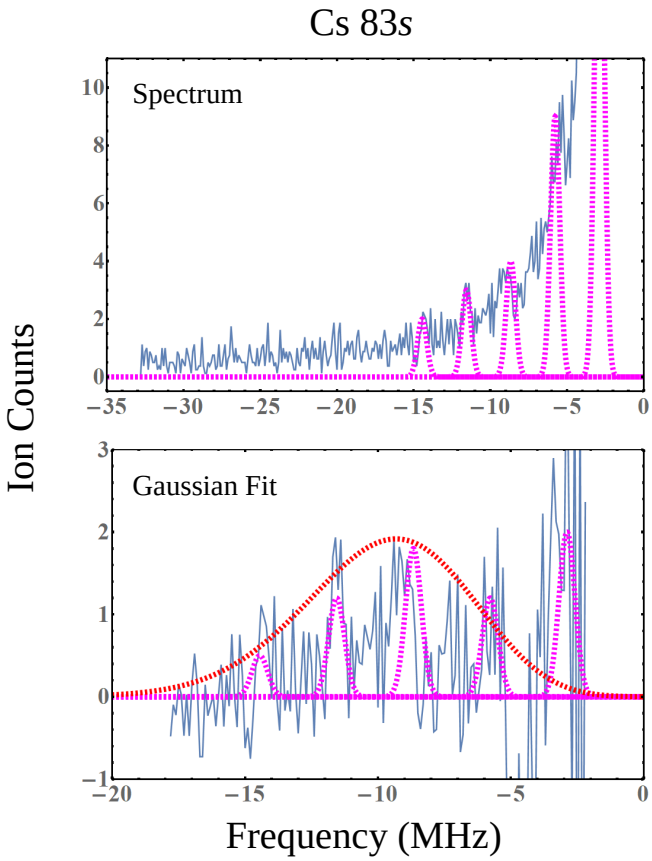

Figure 4.1: The experimental result for the Cs 83s isotropic polyatomic Rydberg molecules, where the atom number density of the cold atomic gas is $\sim 5 \times 10^{12}$ cm^{-3}. The upper graph is the experimental spectrum, where the pink dashed curves are Gaussian distributions we used to fit the molecular signals. The lower graph is the spectrum after we subtracted the base line coming from the Rydberg transition line. The red dashed curve is a Gaussian fit based on the amplitudes of different orders of the molecular signals.

electron in the 83s state. The chance to have a number of ground state atoms less than or more than the mean value $\bar{N}$ within the orbit of the Rydberg electron decreases. The amplitudes of the spectral lines corresponding to more or less atoms within the Rydberg orbital are smaller. This means a series of molecular signals with their amplitudes displaying a Gaussian distribution centered on the order corresponding to the mean value $\bar{N}$ is expected to be observed in spectra.

Figure 4.1 shows experimental results for the Cs 83s isotropic polyatomic

Rydberg molecules. The upper graph is the spectrum of the Cs 83s Rydberg molecules. A series of molecular signals can be seen in the spectrum. These molecular signals are the ground state in the outer-most potential well generated by the s-wave triplet scattering and its multiples generated by different scattering processes with different ground state atoms. We fit each individual molecular signal with a Gaussian distribution, which is shown as a pink dashed line in the spectrum. We find these molecular signals evenly distributed from the Rydberg transition line to -15 MHz, with a frequency difference of ~ 2.9 MHz between two adjacent molecular signals. This energy is the binding energy of the molecular dimer ground state generated by the s-wave triplet scattering process.

Since this series of molecular signals is very close to the atomic Rydberg transition line, the base line of the molecular spectrum is strongly affected by the corresponding Rydberg transition. The amplitude displayed in the experimental spectrum is a sum of the molecular signal and the atomic signal from the corresponding atomic Rydberg transition. To get the base line of the molecular spectrum, we fit the corresponding atomic Rydberg transition to a Gaussian distribution, then subtract this Gaussian curve from the spectrum. The result is shown as the lower graph in figure 4.1. The amplitudes of different molecular signals should fit a Gaussian distribution with the center on the order corresponding to $\bar{N}$. Therefore, we fit the molecular spectrum to a Gaussian distribution according to the amplitudes of different orders of the molecular signals, and find the center of the Gaussian distribution is around the third order of the molecular signals. This indicates that on average there are three ground state atoms within the orbital

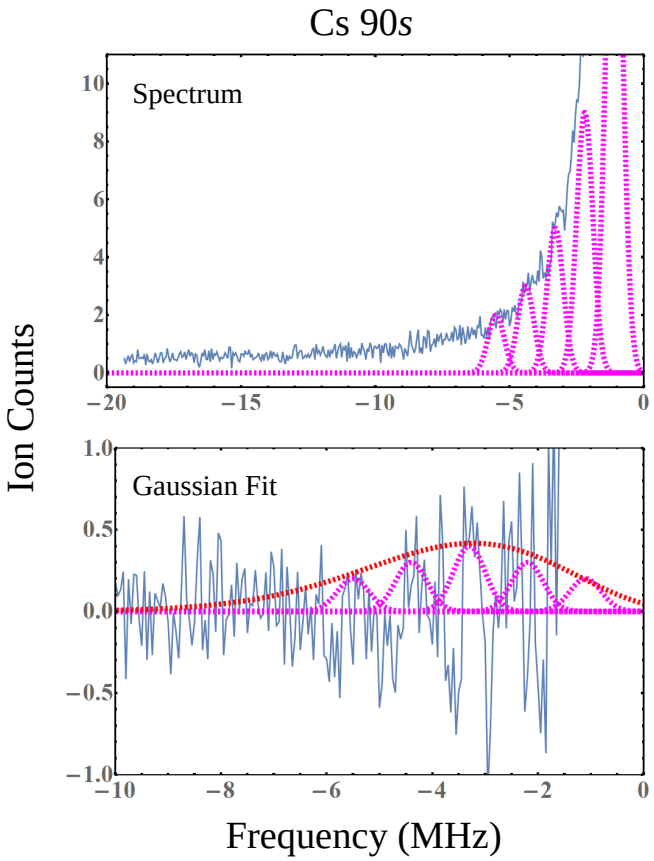

Figure 4.2: The experimental results for the Cs $90s$ isotropic polyatomic Rydberg molecules, where the atom number density of the cold atomic gas is $\sim 3 \times 10^{12}$ cm^{-3}. The upper graph is the experimental spectrum. The pink dashed curves are Gaussian distributions we used to fit the molecular signals. The lower graph is the spectrum after we subtracted the base line coming from the Rydberg transition line. The red dashed curve is a Gaussian fit of the molecular spectrum. In $90s$, molecular signals are spectrally less resolved and energetically close to the atomic Rydberg transition due to the decrease of the binding energy with increasing n.

of the Rydberg electron in the $83s$ state. Using equation 4.3, we can deduce the average density of our cold atomic gas is $\sim 5 \times 10^{12}$ cm^{-3}, which is consistent with our measurements using the absorption imaging.

Similar results were obtained for the $90s$ state, which is shown in figure 4.2. The upper graph is the spectrum of the Cs $90s$ Rydberg molecules. We fit each molecular signal by a Gaussian curve. We can see a series of molecular signals are

evenly distributed on the red side of the Rydberg transition line with a frequency difference of $\sim$ 1.1 MHz between two adjacent molecular signals. This is the binding energy of the ground state in the outer-most potential well generated by the s-wave triplet scattering process of the corresponding Rydberg dimer. The binding energy of the Rydberg dimer decreases from 2.9 MHz for the $83s$ state to 1.1 MHz for the $90s$ state. Since the binding energy is smaller for the $90s$ state, the different polyatomic Rydberg molecular signals are less resolved, which makes them harder to distinguish. The Gaussian fit of the amplitudes of different molecular signals is shown in the lower graph. We can see the center of the Gaussian fit is at around the quatramer of this series of polyatomic molecular signals. This indicates on average there are three ground state atoms within the orbital of the Rydberg electron in $90s$ state. The average density calculated using equation 4.3 is $\sim 3 \times 10^{12}$ cm^{-3}, which is consistent with what we obtained for the $83s$ state.

4.3 Anisotropic Polyatomic Rydberg Molecules

When a Rydberg electron is in an nd or higher angular momentum state, its probability distribution is anisotropic. The total binding energy depends on the relative positions of the ground state atoms. Triatomic "trilobite" Rydberg molecules have been theoretically studied recently [57, 58, 59], where expressions for potential energy surfaces have been derived.

For $R_1 = R_2$, the total binding energy of the $l = 2$ trimer eigenstates can be

expressed as

$$E_{\pm}(\mathrm{R},\theta) = E_{\mathrm{dim}}(\mathrm{R})\left[1 \pm (-\frac{1}{2} + \frac{3}{2}\cos^2\theta)\right], \tag{4.4}$$

where $E_{\mathrm{dim}}(\mathrm{R})$ is the corresponding diatomic PECs. The result is illustrated in figure 4.3 (a), which describes $E_{\pm}$ as functions of the angle enclosed by the two ground state atoms, namely the function $1 \pm (-\frac{1}{2} + \frac{3}{2}\cos^2\theta)$. The minima on the curve give the angles which are energetically favored. The electronic wavefunction maximizes its density on the two ground state atoms in these configurations. For E_+, the energetically favored angles are $\theta = 0$ and $\theta = \pi$, where the total binding energy is twice the binding energy of the dimer state. For E_-, the energetically favored angle is $\theta = \pi/2$. Although the minimum of the E_- channel is not a global minimum, it can still support vibrational states at 3/2 the dimer binding energy.

For anisotropic polyatomic Rydberg molecules, different spin dependent relativistic effects need to be treated carefully. There are several reasons. The total binding energy is a function of the angle enclosed by the two ground state atoms, which means the trimer spectra signal shifts as the relative positions of the ground state atoms change. The weak trimer signals merge together with the dimer signals in spectra, which are complex due to spin dependent relativistic effects. An accurate calculation is needed to seek out the nonadditive trimer signals from a complex background.

There are two important spin dependent relativistic effects: the spin-orbit

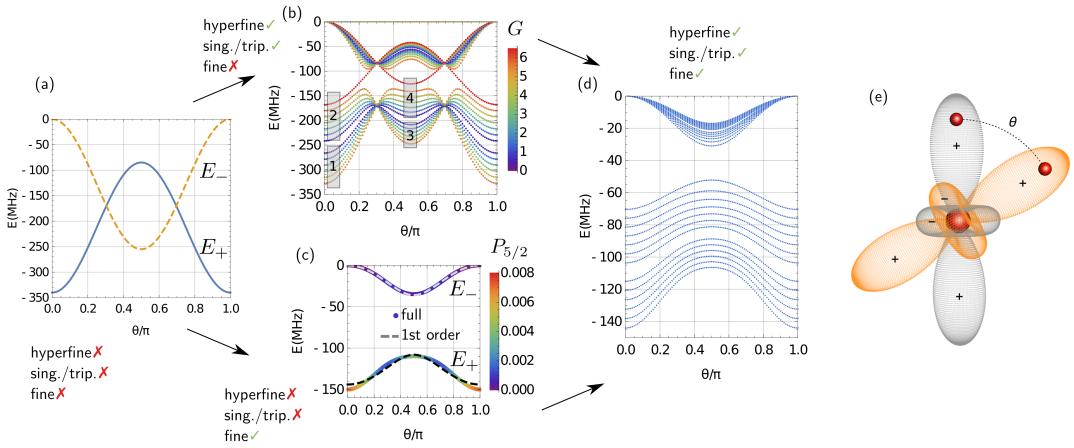

Figure 4.3: The angular trimer potential energy curves of the Cs $34d_{3/2}$ Rydberg molecules (a) for $R_1 = R_2 = 1868\ a_0$ without considering any spin dependent relativistic effects. The influence of the hyperfine interactons of the ground state atoms is shown in (b), and (c) shows the influence of the spin-orbit coupling in the Rydberg atom. (d) shows the final potential energy curves after adding spin dependent relativistic effects, where we combined both the hyperfine interactions and the spin-orbit coupling. The primitive orbitals (signs indicated) of the trimer state are illustrated in (e).

coupling of the Rydberg atom and the hyperfine interaction of each ground state atom with the Rydberg electron. Figure 4.3 (b) shows the change of the PECs after adding the hyperfine interactions. Due to the hyperfine interactions, $\boldsymbol{G} = \boldsymbol{F}_1 + \boldsymbol{F}_2 + \boldsymbol{s}_{\mathrm{Ryd}}$ is a good quantum number, where $\boldsymbol{F}_1 = \boldsymbol{F}_2 = 3$ and $\boldsymbol{s}_{\mathrm{Ryd}} = 1/2$. G takes half-integer values between 13/2 and 1/2. Each of these curves belongs to a number of 2G degenerate states. The 13 curves can be further subdivided into 6 deeper curves and 7 shallower curves corresponding to the s-wave triplet scattering process and the mixing between the s-wave singlet and the s-wave triplet scattering process, which are marked by the gray rectangle boxes in figure 4.3 (b). The influence of the spin-orbit coupling is shown in figure 4.3 (c). The spin-orbit coupling leads to a mixing of $34d_{3/2}$ ($36d_{3/2}$) and $34d_{5/2}$ ($36d_{5/2}$). The mixing with the $d_{5/2}$ angular momentum state is represented by the vertical colored bar on the

right side of figure 4.3 (c). We can see that the trimer state corresponding to E_- is almost a pure $d_{3/2}$ state, but the trimer state corresponding to E_+ is a hybrid mixture with the $d_{5/2}$ state. Due to the selection rules, the spin-orbit coupling lifts the degeneracy of E_- and E_+ and generates avoided crossings. Then we combine these two spin dependent relativistic effects, and obtain the BO angular PECs in figure 4.3 (d). $E_\pm$ splits into two sets of potential energy curves. The E_- set of PECs has their minima at $\theta = \pi/2$ and is shallower. The E_+ set of PECs has their minima at $\theta = 0$, π and is deeper than the E_- set.

The evidence for nonadditive three-body interactions comes from the comparison between the simulated spectra and the experimental observations. First, we present the simulations of the dimer states and the trimer states separately, as shown in figure 4.4, and compared them individually to the experimental observations. This allows us to directly study the effect of having nonadditive trimers presented in the trap.

The potential energy curves are displayed as gray solid curves on the graph. The outer-most potential well formed by the s-wave triplet scattering process is at around 1800 a.u. with a depth of $\sim$ 70 MHz. The hyperfine interaction of the ground state atom mixing the singlet scattering channel with the triplet scattering channel, generates a new series of potential energy curves. Its outer-most potential well has a shallower potential depth of $\sim$ 30 MHz. Both the PECs generated by the triplet scattering and the mixing between the singlet and triplet scattering start to split as the internuclear distance R decreases, because of the influence of the p-wave scattering process. Here, we only presented several

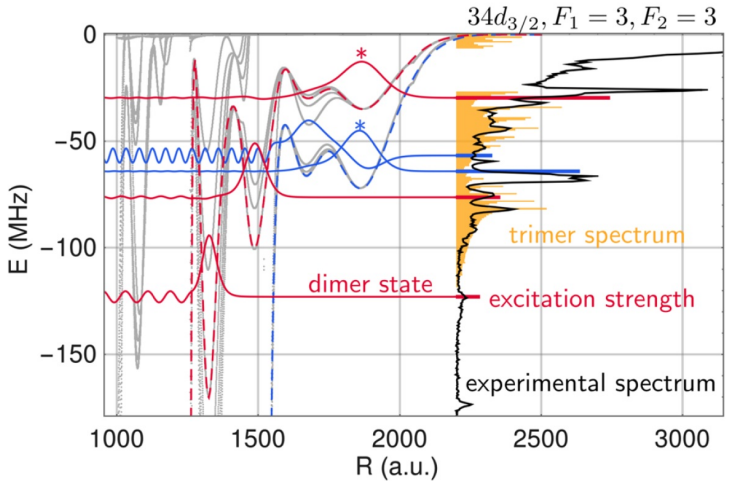

Figure 4.4: Comparison between the experimental spectrum (black line) and theoretical simulation of the dimer states (colored lines) and trimer states (orange histograms). The dimer states come from a few diatomic potential energy curves (dashed lines) that have been selected from all potential energy curves (gray background).

dominant dimer states with their wavefunctions represented by solid colored curves. The dimer vibrational wavefunctions were calculated using the finite difference method and considering the quantum reflection formed by the steep potential drops. The relative strengths of the transitions are represented by the lengths of the corresponding red horizontal bars shown with the experimental spectrum. The strength of a molecular signal can be estimated by calculating the corresponding Frank-Condon factor

$$\Gamma_\nu \propto \left| \int \mathrm{dR} \chi_0(\mathrm{R}) \mathrm{R}^2 \chi_\nu(\mathrm{R}) \right|^2, \tag{4.5}$$

where the initial state $\chi_0(\mathrm{R})$ is the pair wavefunction for two cold atoms in the ground state [60].

The most striking molecular signals in the spectrum are well described by the

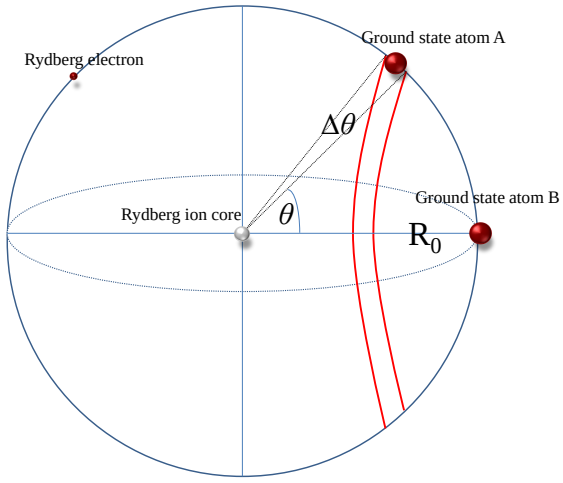

Figure 4.5: The diagram to show the probability to have two ground state atoms with an angle θ enclosed by them.

dimer simulation. The strong peaks at -25 MHz and -60 MHz correspond to the ground molecular dimer states supported in two outer-most potential energy wells. The small lump at around -120 MHz corresponds to the ground molecular dimer state supported by an inner potential well.

The trimer spectrum was simulated by fixing $R_1 = R_2$ at the internuclear distance of the outer-most potential well R_0, due to the probability to find two ground state atoms at distances R_1 and R_2 from the Rydberg ion core scales as $(R_1R_2)^2$. For $34d_{3/2}$, $R_0 = 1868\ a_0$, and for $36d_{3/2}$, $R_0 = 2110\ a_0$. Trimer states supported in the inner parts of the PECs were ignored in the calculation. The trimer spectrum was simulated using Monte Carlo method. Two ground state atoms are randomly placed on a sphere with radius R_0 and centered on the Rydberg ion core. After one ground state atom is fixed on the sphere, the chance to find the other ground state atom on the sphere at an angle θ with respect to it depends on the area of a ring associated with θ on the sphere, figure 4.5. The area

of the ring is $2\pi\sin\theta \mathrm{R}^2 \mathrm{d}\theta$. This leads to a $\sin\theta$ distribution of the sample when we obtained the trimer spectrum simulation. More contributions to the trimer spectra are expected for energies close to $E(\mathrm{R}_1, \mathrm{R}_2, \theta \approx \pi/2)$.

In figure 4.4, the trimer signal is shown as a histogram of energies $E(\mathrm{R}_1, \mathrm{R}_2, \theta)$. The bin width of the histogram is set to be 700 kHz and 3 MHz for $34d_{3/2}$ and $36d_{3/2}$ respectively according to the conditions of the experiment. Good agreement exists between the trimer simulation and the experimental spectrum. For example, from -30 MHz to -55 MHz and from -70 MHz to -120 MHz, the simulated trimer state can predict the positions, strengths and trend of the experimental spectrum very well.

To further confirm the observation of nonadditive three-body interactions, we compared our simulations to the experimental spectra in another way. We compared the simulated dimer state spectra and the simulated spectra including both dimer states and trimer states to the experimental observations. The results are shown in figure 4.6. Unlike the results shown in figure 4.4 where only the dominant dimer states are displayed, here we include all bound dimer states. Both dimer and trimer states are convoluted with Gaussian profiles with a linewidth of 700 kHz (3 MHz) for $34d_{3/2}$ ($36d_{3/2}$). In figure 4.6, we can see that the simulated spectra including both the dimer states and trimer states (black dotted-dashed line) agree with our experimental observation (blue solid line) much better than the spectra that only include the dimer states (gray dotted-dashed line) for both the $34d_{3/2}$ and $36d_{3/2}$ state. Three parts of the spectra marked by red circles, -35 MHz to -45 MHz and -80 MHz to -100 MHz in $34d_{3/2}$, -50 MHz to -60 MHz in

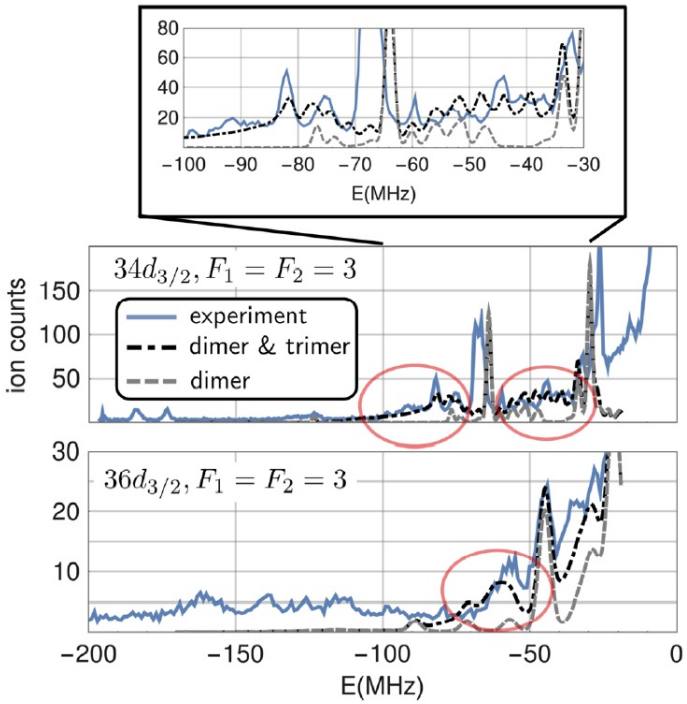

Figure 4.6: Comparison between the experimental spectra, the simulated spectra which only include dimer states and the simulated spectra which include both dimer states and trimer states. The most significant differences between the dimer state simulations and simulations including both dimer states and trimer states are marked out by three red circles, where we can see the simulations which include both dimer states and trimer states agree with our experimental observation better than the dimer state simulations.

$36_{3/2}$, clearly show that the experimental spectra can only be explained by the inclusion of the trimer states.

In the experimental spectra, there are other molecular signals from -100 MHz to -200 MHz, on the red side of the Rydberg transition line. These states are beyond the scope of our theoretical simulation. They are molecular states which exist in the inner parts of the potential energy curves. As discussed in Chapter 2, the inner parts are strongly influenced by the p-wave scattering processes and shape resonances, which make them much deeper than the outer parts.

4.4 Experiment Method

Experimental spectra were obtained using two-photon photoassociations. Details of the experiment have been discussed in Chapter 3. Cold atomic gases are prepared in our FORT at a temperature of 30 μK. The maximum atom number density is $\sim 1 \times 10^{13}$ cm^{-3} with a Gaussian profile distribution. 1000 pulses of excitation are applied at a frequency of 2000 Hz. The first step laser and Rydberg excitation laser pulse simultaneously for 10 μs. 500 ns after the end of each laser pulse, a 67 V cm^{-1} electric field pulse with a duration of 500 ns extracts ions to a MCP detector at the bottom of the experimental chamber. Considering the lifetimes of the Rydberg molecules, which are similar to the lifetimes of the corresponding Rydberg atoms, the length of the excitation can be adjusted to get the best signal. For Rydberg atoms, as discussed in Chapter 2, the lifetime increases as n increases.

Excitations can be conducted with the FORT beams on. Since the strong FORT beams give considerable AC Stark shifts, two problems need to be carefully treated. The first one is different parts of the cross section of the FORT beams have different intensities, which give different AC Stark shifts. Here we adjust the diameter of our excitation laser to be ~ 70 μm, which is smaller than the diameter of the cross section, ~ 98 μm. The second problem is the power of the FORT laser increases during 1000 excitations. This means the AC Stark shift changes. To solve this problem, we only count the ions generated by the first 50 to 300 pulses. These two problems give a line broadening that decreases the

resolution of our experiment. We can eliminate the AC Stark shift by turning off the FORT beam during excitations. This gives us molecular signals with higher spectral resolution, but with smaller amplitudes. This is because the trap freely expands when the FORT is off, which gives a lower density. Both the results with the FORT beams on and off were obtained.

The total Rabi frequency of the two-photon transition we use to photoassociate ultralong-range Rydberg molecules can be calculated using equation 3.35. The first step laser with a wavelength of $\sim$ 852.33 nm can excite Cs atoms from the ground state $6s_{1/2}$ $(F = 3)$ to the intermediate state $6p_{3/2}$ $(F = 4)$ with a detuning $\Delta = 300$ MHz to the blue side. The laser beam is well collimated after being filtered by a polarization maintaining fiber. It is collimated to a diameter of ~ 2 mm and has a power of ~ 4 mW. The large size of the first step laser beam makes the alignment easier. The power was chosen to give a Rabi frequency strong enough to excite the atoms without significant power broadening. The detuning of the first step laser from resonance can be tuned by adjusting either the frequency shift of the AOM (A28 in Appendix D) or the frequency of the side band used to lock the laser. According to equation 3.35, when the first step laser is close to the resonance with the intermediate state $6p_{3/2}$ $(F = 4)$, the smaller detuning gives a better total Rabi frequency, but a broader molecular signal. A TA-SHG with a wavelength of $\sim$ 511 nm is used to achieve the Rydberg excitation. The power of the TA-SHG laser beam is 140 mW. Both lasers are linearly polarized in the same direction and locked to an ultralow-expansion FP cavity using the PDH technique. Each laser has a linewidth of 30 kHz. The photoassoicated Rydberg molecules

were photoionized by the FORT beams. Each spectroscopic scan contains 400 steps with a step size of 0.5 MHz. The step size was chosen by estimating the linewidth of the molecular signals in the experimental spectra, which is influenced by the linewidth of the excitation lasers, residual electric and magnetic fields, dipole moments of the formed molecules, and temperatures. We count both the Cs^+ signal and Cs_2^+ signal to generate experimental spectra.

4.5 Summary

Depending on the angular momentum state of the Rydberg atom, there are two different types of polyatomic Rydberg molecules, isotropic and anisotropic polyatomic Rydberg molecules. When the Rydberg electron is in an ns state, the spherically symmetric probability distribution of the Rydberg electron makes the Rydberg electron equally interact with each ground state atom. The total binding energy is a summation of the binding energy from each scattering process. We studied the additive interactions using the Cs $6s + 83s$ and $6s + 90s$ isotropic polyatomic Rydberg molecules. In the experimental spectra, a series of molecular signals evenly distributed on the red side of the Rydberg transition line is observed. Different orders of the molecular signals correspond to different numbers of ground state atoms within the orbital of the Rydberg electron. The frequency difference between two adjacent molecular signals is the binding energy of the diatomic Rydberg molecule. The total binding energies of the isotropic polyatomic Rydberg molecules are multiples of the binding energy of the diatomic Rydberg molecule.

When the Rydberg electron is in an $l > 0$ angular momentum state, the probability distribution of the Rydberg electron is not spherically symmetric anymore. The total binding energy depends on the relative positions of different ground state atoms. Spatial correlations are established between different ground state atoms due to the anisotropic probability distribution of the Rydberg electron. The nonadditive interactions were studied by us for the first time using the Cs $6s+6s+34d$ and $6s+6s+36d$ anisotropic triatomic Rydberg molecules. The trimer state simulations were obtained using the angular dependent PECs considering spin dependent relativistic effects. We compared the experimental observations with our theoretical simulations. The simulations including both the Rydberg dimer states and trimer states agree with the experimental observations better than the dimer state simulations, which proves the existence of the anisotropic Rydberg trimer states.

Chapter 5

Conclusions

A loosely bound Rydberg electron can be approximately seen as a free electron with small kinetic energy near its outer turning point. It can be scattered by a ground state atom when the ground state atom gets close to the Rydberg electron. The scattering potential is a polarization potential. The low energy scattering process can be described by a Fermi pseudopotential. For alkali atoms, negative scattering lengths generate potential wells which are deep enough to support bound molecular states. The formed molecule is called an ultralong-range Rydberg molecule. According to equation 2.3, the radius of a Rydberg electron's orbit increases as $a_0 n^2$. This makes us able to manipulate the number of ground state atoms interacting with a Rydberg electron in a cold atomic gas for a particular atom number density by exciting the Rydberg electron to different Rydberg states.

Depending on the angular momentum state of the Rydberg electron, two types of polyatomic Rydberg molecules exist. An isotropic polyatomic Rydberg molecule has the Rydberg electron in an ns state. The probability distribution of the Rydberg electron is spherically symmetric. The isotropic probability distribution makes the Rydberg electron equally interact with each ground state atom. The total binding energy is a summation of binding energies from different ground state atoms, which is shown in equation 4.1. Since the probability to find N ground state atoms at distances R_1, R_2, ..., R_N scales as $(R_1 \cdot R_2 \cdot ... \cdot R_N)^2$, the

dominant molecular signals are the ground molecular states in the outer-most potential wells, where the internuclear distance R_0 is the largest. Experimental signals of polyatomic molecular states with short bond lengths are suppressed. Equation 4.1 changes to be equation 4.2. The total binding energy of an isotropic polyatomic Rydberg molecule with N ground state atoms is N times the binding energy of the corresponding diatomic Rydberg molecule. We studied the isotropic polyatomic Rydberg molecules using the Cs $6s + 83s$ and $6s + 90s$ Rydberg molecules. For each Rydberg state, a series of molecular signals was observed on the red side of the Rydberg transition line. They are evenly distributed with equal frequency difference between two adjacent molecular signals. This is exactly what is described by equation 4.2. Different orders of molecular signals correspond to polyatomic Rydberg molecules with different numbers of ground state atoms. Their binding energies are multiples of the binding energy of the Rydberg dimer. Since on average there are a certain number $\bar{N}$ of ground state atoms within the orbit of a Rydberg electron in an ns state, the polyatomic Rydberg molecule with $\bar{N}$ ground state atoms has the strongest molecular signal in the spectra.

When the Rydberg electron is in an $l > 0$ angular momentum state, the probability distribution of the Rydberg electron is not spherically symmetric anymore. The anisotropic probability distribution leads the total binding energy to depend on the relative positions of different ground state atoms. Spatial correlations are established between different ground state atoms. We used the Cs $6s + 6s + 34d$ and $6s + 6s + 36d$ triatomic Rydberg molecules to study the nonadditive interacitons between the Rydberg electron and the two ground state

atoms. The total binding energy is expressed as equation 4.4. The first part on the right side of the equation is the binding energy of the Rydberg dimer. The influence of the relative positions of the two ground state atoms on the total binding energy is represented as the second part. Different spin dependent relativistic effects are taken into account. These interactions include the hyperfine interaction of the ground state atom and the spin-orbit coupling of the Rydberg atom. The spin dependent relativistic effects lift the degeneracy of the PECs. We obtained simulated spectra of the Cs $6s + 6s + 34d$ and $6s + 6s + 36d$ Rydberg trimers and compared them to the experimental observations in two different ways. In the first way, we separately compared the dimer simulations and trimer simulations to the experimental observations. We find both simulations are consistent with our observations. In the second way, we combined the trimer simulations and dimer simulations together. The combined simulations agree with the experimental spectra better than the dimer simulations. Several features in the experimental spectra which are not captured by the dimer simulations can be well described by the combined simulations.

As discussed in Chapter 2, the angular dependence of the total binding energy is generated by the cross term g_{ij} under the square root in equation 2.45. When the principal quantum number state n, angular momentum state l and its projection on the internuclear axis m are all fixed, the cross term can be canceled. The total binding energy is a summation of binding energies from different scattering processes. This is what happens when a Rydberg electron is in an ns state, where $l = m = 0$.

For $l > 0$, m can also be fixed using the optical polarization. This is realized by adding magnetic fields to lift the degeneracy of the m states, and then using optical pulses with certain lengths to excite the atoms into a certain m' state [61]. We expect to obtain experimental spectra which are different with the experimental spectra where m is not fixed.

It would be more interesting to investigate how a Rydberg electron interacts with many ground state atoms in electric fields. "Trilobite" molecules and "butterfly" molecules are good candidates for this topic [57, 58, 62]. The large dipole moments with them cause the formed polyatomic Rydberg molecules to have particular geometric configurations in electric fields to get the lowest binding energies. The geometric configuration depends on the direction of the electric field and the polarization direction of the linearly polarized excitation laser. Different directions of the electric fields with respect to the polarization of the excitation laser give different geometric configurations and different experimental spectra.

Besides these two interesting topics, there are lots of other fascinating topics on ultralong-range Rydberg molecules. For example, in Chapter 2, we described how to use spectroscopy to measure the dipole moments of ultralong-range Rydberg molecules. Another method to measure the dipole moment is to use the Rydberg blockade generated by the dipole moment between two ultralong-range Rydberg molecules [63, 64]. We can prepare cold atoms in two optical tweezers separated by a distance R, use one laser with a certain frequency ω_0 to photoassociate "trilobite" molecules or "butterfly" molecules in one optical tweezer and scan the second laser near the frequency ω_0 to see at what frequency ω' we can generate

the same Rydberg molecules in the other optical tweezer. The relation between the frequency ω' and the distance R between the two optical tweezers can be used to derive the Rydberg blockade radius and the dipole moments of the "trilobite" or "butterfly" molecules.

"Trilobite" molecules and their large permanent dipole moments come from the summation of Rydberg electrons' wavefunctions of different angular momentum states. Recently, Matthew Eiles and his colleagues predict the existence of a ghost "trilobite" chemical bond [65]. They proved that we can realize the same summation of wavefunctions of different angular momentum states, by adding electric fields and magnetic fields with particular amplitudes and lengths in a certain sequence on Rydberg atoms. This means without the scattering processes between the Rydberg electron and ground state atoms, we can generate ghost "trilobite" atoms possessing large permanent dipole moments. The creation and observation of a ghost "trilobite" chemical bond in an experiment is very attractive. However, this topic is very challenging, extremely accurate control of electric fields and magnetic fields is needed.

The Hamiltonian 2.36 we describe in Chapter 2 gives accurate predictions of the relative positions of different molecular states with respect to the corresponding Rydberg transition line. Unfortunately, the calculations of rovibrational line strengths still cannot give satisfying results which are quantitatively consistent with experimental observations. Moreover, our recent work on photoionization of Rydberg molecules shows when we photoionize Rydberg molecules, Rydberg molecules of some molecular states are more likely to decay as atomic ions, while

others are more likely to decay as molecular ions [66, 67, 68]. This suggests spectral results which only use atomic ion counts or molecular ion counts as the signature of the number of Rydberg molecules created in experiments are not accurate. It turns out both the theoretical calculations and the experimental observations of the relative line strengths of different rovibrational states are suspect. In experiments, we need to include both atomic ion counts and molecular ion counts into spectra to reflect the relative rovibrational line strengths correctly.

The gigantic permanent dipole moments of ultralong-range Rydberg molecules make ultralong-range Rydberg molecules have high potential commercial values. For example, the dipole moment of the Cs "trilobite" molecules measured by our group is $\sim$ 2000 Debye. It is two orders of magnitude larger than the dipole moment of RbI (11.5 Debye), the largest dipole moment reported in [69]. Because of the large permanent dipole moment, the ultralong-range Rydberg molecule is very sensitve to external DC electric fields. They can be used to measure the strengths and directions of the electric fields, when the field is extremely weak where other methods [70, 71] are not capable.

References

[1] E. Amaldi, Nature **133**, 141 (1934).

[2] E. Fermi, Il Nuovo Cimento (1924-1942) **11**, 157 (1934).

[3] A. Omont, Journal de Physique **38**, 1343 (1977).

[4] C. H. Greene, A. Dickinson, and H. Sadeghpour, Physical review letters **85**, 2458 (2000).

[5] E. L. Hamilton, C. H. Greene, and H. Sadeghpour, Journal of Physics B: Atomic, Molecular and Optical Physics **35**, L199 (2002).

[6] V. Bendkowsky, B. Butscher, J. Nipper, J. P. Shaffer, R. Löw, and T. Pfau, Nature **458**, 1005 (2009).

[7] V. Bendkowsky, B. Butscher, J. Nipper, J. Balewski, J. Shaffer, R. Löw, T. Pfau, W. Li, J. Stanojevic, T. Pohl, *et al.*, Physical review letters **105**, 163201 (2010).

[8] J. Tallant, S. Rittenhouse, D. Booth, H. Sadeghpour, and J. Shaffer, Physical review letters **109**, 173202 (2012).

[9] W. Li, T. Pohl, J. Rost, S. T. Rittenhouse, H. Sadeghpour, J. Nipper, B. Butscher, J. Balewski, V. Bendkowsky, R. Löw, *et al.*, Science **334**, 1110 (2011).

[10] A. T. Krupp, A. Gaj, J. B. Balewski, P. Ilzhöfer, S. Hofferberth, R. Löw, T. Pfau, M. Kurz, and P. Schmelcher, Physical review letters **112**, 143008 (2014).

[11] D. A. Anderson, S. A. Miller, and G. Raithel, Physical review letters **112**, 163201 (2014).

[12] D. Booth, S. Rittenhouse, J. Yang, H. Sadeghpour, and J. Shaffer, Science **348**, 99 (2015).

[13] D. A. Anderson, S. A. Miller, and G. Raithel, Physical Review A **90**, 062518 (2014).

[14] H. Saßmannshausen, F. Merkt, and J. Deiglmayr, Physical review letters **114**, 133201 (2015).

[15] F. Böttcher, A. Gaj, K. M. Westphal, M. Schlagmüller, K. S. Kleinbach, R. Löw, T. C. Liebisch, T. Pfau, and S. Hofferberth, Physical Review A **93**, 032512 (2016).

[16] S. Markson, S. T. Rittenhouse, R. Schmidt, J. P. Shaffer, and H. R. Sadeghpour, ChemPhysChem **17**, 3683 (2016).

[17] M. Schlagmüller, T. C. Liebisch, H. Nguyen, G. Lochead, F. Engel, F. Böttcher, K. M. Westphal, K. S. Kleinbach, R. Löw, S. Hofferberth, *et al.*, Physical review letters **116**, 053001 (2016).

[18] J. B. Balewski, A. T. Krupp, A. Gaj, D. Peter, H. P. Büchler, R. Löw, S. Hofferberth, and T. Pfau, Nature **502**, 664 (2013).

[19] R. Schmidt, H. Sadeghpour, and E. Demler, Physical review letters **116**, 105302 (2016).

[20] F. Camargo, R. Schmidt, J. Whalen, R. Ding, G. Woehl Jr, S. Yoshida, J. Burgdörfer, F. Dunning, H. Sadeghpour, E. Demler, *et al.*, Physical review letters **120**, 083401 (2018).

[21] R. Schmidt, J. Whalen, R. Ding, F. Camargo, G. Woehl Jr, S. Yoshida, J. Burgdörfer, F. Dunning, E. Demler, H. Sadeghpour, *et al.*, Physical Review A **97**, 022707 (2018).

[22] J. A. Fernández, P. Schmelcher, and R. González-Férez, Journal of Physics B: Atomic, Molecular and Optical Physics **49**, 124002 (2016).

[23] C. Fey, M. Kurz, and P. Schmelcher, Physical Review A **94**, 012516 (2016).

[24] C. Fey, J. Yang, S. T. Rittenhouse, F. Munkes, M. Baluktsian, P. Schmelcher, H. R. Sadeghpour, and J. P. Shaffer, Physical Review Letters **122**, 103001 (2019).

[25] A. Gaj, A. T. Krupp, J. B. Balewski, R. Löw, S. Hofferberth, and T. Pfau, Nature communications **5**, 4546 (2014).

[26] J. J. Sakurai, J. Napolitano, *et al.*, *Modern quantum mechanics* (Pearson Harlow, ADDRESS, 2014), Vol. 185.

[27] J. D. Jackson, Classical electrodynamics, 1999.

[28] T. F. Gallagher, *Rydberg atoms* (Cambridge University Press, ADDRESS, 2005), Vol. 3.

[29] H. A. Bethe and E. E. Salpeter, *Quantum mechanics of one-and two-electron atoms* (Springer Science & Business Media, ADDRESS, 2012).

[30] W. Li, I. Mourachko, M. Noel, and T. Gallagher, Physical Review A **67**, 052502 (2003).

[31] J. Han, Y. Jamil, D. Norum, P. J. Tanner, and T. Gallagher, Physical Review A **74**, 054502 (2006).

[32] P. Goy, J. Raimond, G. Vitrant, and S. Haroche, Physical Review A **26**, 2733 (1982).

[33] K.-H. Weber and C. J. Sansonetti, Physical Review A **35**, 4650 (1987).

[34] J. a. Mitroy, M. S. Safronova, and C. W. Clark, Journal of Physics B: Atomic, Molecular and Optical Physics **43**, 202001 (2010).

[35] M. Marinescu, H. Sadeghpour, and A. Dalgarno, Physical Review A **49**, 982 (1994).

[36] F. Salvat, J. Fernández-Varea, and W. Williamson Jr, Computer physics communications **90**, 151 (1995).

[37] T. Gallagher, S. Edelstein, and R. Hill, Physical Review A **11**, 1504 (1975).

[38] I. Beterov, I. Ryabtsev, D. Tretyakov, and V. Entin, Physical Review A **79**, 052504 (2009).

[39] R. Potvliege and C. Adams, New Journal of Physics **8**, 163 (2006).

[40] C. Gabbanini, Spectrochimica Acta Part B: Atomic Spectroscopy **61**, 196 (2006).

[41] J. Tallant, D. Booth, and J. Shaffer, Physical Review A **82**, 063406 (2010).

[42] C. J. Foot *et al.*, *Atomic physics* (Oxford University Press, ADDRESS, 2005), Vol. 7.

[43] N. Y. Du and C. H. Greene, Physical Review A **36**, 971 (1987).

[44] C. Bahrim and U. Thumm, Physical Review A **61**, 022722 (2000).

[45] G. J. Schulz, Reviews of Modern Physics **45**, 378 (1973).

[46] T. Niederprüm, O. Thomas, T. Eichert, C. Lippe, J. Pérez-Ríos, C. H. Greene, and H. Ott, Nature communications **7**, 12820 (2016).

[47] A. Khuskivadze, M. Chibisov, and I. Fabrikant, Physical Review A **66**, 042709 (2002).

[48] J. Yang, A. Jahangiri, S. Rittenhouse, M. Reschke, D. Booth, H. Sadeghpour, and J. Shaffer, Bulletin of the American Physical Society **61**, (2016).

[49] S. Kuppens, K. Corwin, K. Miller, T. Chupp, and C. Wieman, Physical review A **62**, 013406 (2000).

[50] D. A. Steck, URL http://steck. us/alkalidata (2012).

[51] C. J. Dedman, J. Nes, T. Hanna, R. Dall, K. Baldwin, and A. Truscott, Review of Scientific Instruments **75**, 5136 (2004).

[52] J. E. Tallant, Ph.D. thesis, 2012.

[53] R. Grimm, M. Weidemüller, and Y. B. Ovchinnikov, *Advances in atomic, molecular, and optical physics* (Elsevier, ADDRESS, 2000), Vol. 42, pp. 95–170.

[54] K. M. Jones, E. Tiesinga, P. D. Lett, and P. S. Julienne, Reviews of Modern Physics **78**, 483 (2006).

[55] E. D. Black, American journal of physics **69**, 79 (2001).

[56] J. Alnis, A. Matveev, N. Kolachevsky, T. Udem, and T. Hänsch, Physical Review A **77**, 053809 (2008).

[57] I. C. Liu and J. M. Rost, The European Physical Journal D-Atomic, Molecular, Optical and Plasma Physics **40**, 65 (2006).

[58] I. C. Liu, J. Stanojevic, and J. M. Rost, Physical review letters **102**, 173001 (2009).

[59] C. Fey, F. Hummel, and P. Schmelcher, Physical Review A **99**, 022506 (2019).

[60] B. DeSalvo, J. Aman, F. Dunning, T. Killian, H. Sadeghpour, S. Yoshida, and J. Burgdörfer, Physical Review A **92**, 031403 (2015).

[61] J. Söding, D. Guéry-Odelin, P. Desbiolles, G. Ferrari, and J. Dalibard, Physical review letters **80**, 1869 (1998).

[62] P. J. Luukko and J.-M. Rost, Physical review letters **119**, 203001 (2017).

[63] E. Urban, T. A. Johnson, T. Henage, L. Isenhower, D. Yavuz, T. Walker, and M. Saffman, Nature Physics **5**, 110 (2009).

[64] M. Saffman, T. G. Walker, and K. Mølmer, Reviews of Modern Physics **82**, 2313 (2010).

[65] M. T. Eiles, Z. Tong, and C. H. Greene, Physical review letters **121**, 113203 (2018).

[66] T. Niederprüm, O. Thomas, T. Manthey, T. M. Weber, and H. Ott, Physical review letters **115**, 013003 (2015).

[67] M. Schlagmüller, T. C. Liebisch, F. Engel, K. S. Kleinbach, F. Böttcher, U. Hermann, K. M. Westphal, A. Gaj, R. Löw, S. Hofferberth, *et al.*, Physical Review X **6**, 031020 (2016).

[68] T. Schmid, C. Veit, N. Zuber, R. Löw, T. Pfau, M. Tarana, and M. Tomza, Physical review letters **120**, 153401 (2018).

[69] W. M. Haynes, *CRC handbook of chemistry and physics* (CRC press, ADDRESS, 2014).

[70] H. Fan, S. Kumar, R. Daschner, H. Kübler, and J. Shaffer, Optics Letters **39**, 3030 (2014).

[71] H. Fan, S. Kumar, J. Sedlacek, H. Kübler, S. Karimkashi, and J. P. Shaffer, Journal of Physics B: Atomic, Molecular and Optical Physics **48**, 202001 (2015).

Appendix A

Trapping Laser Scheme

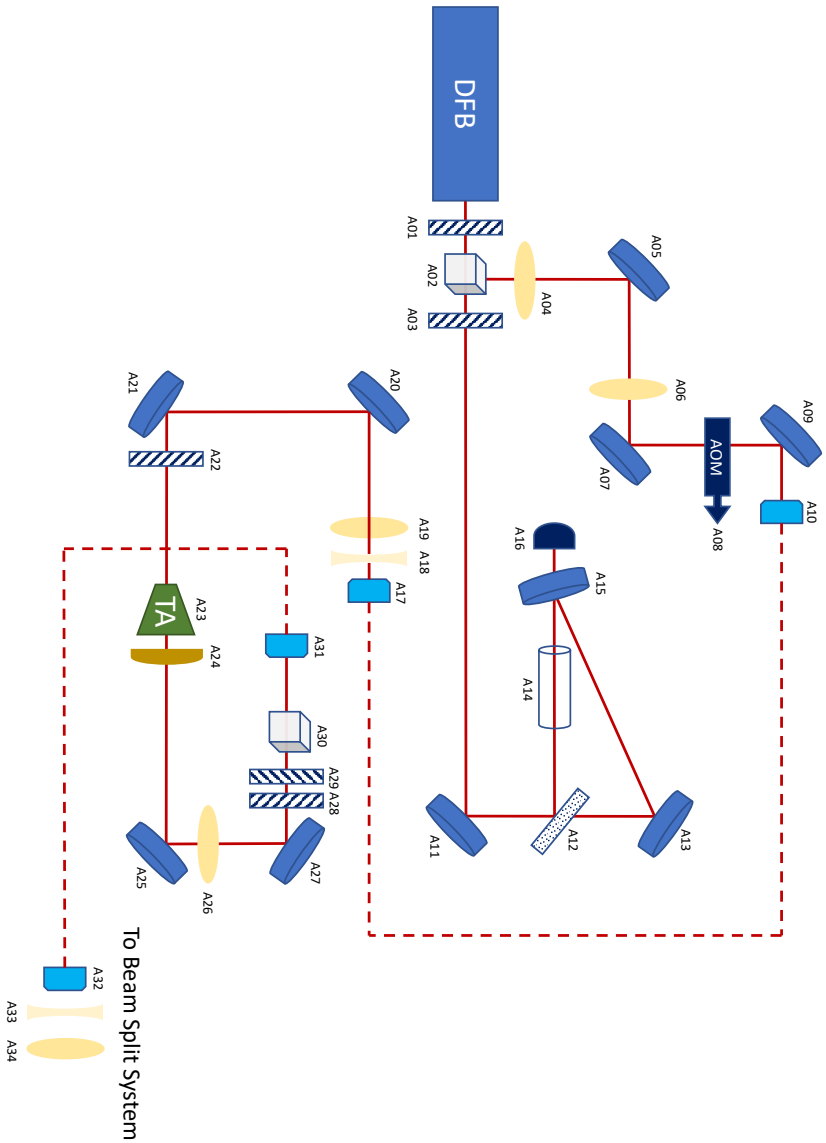

Figure A.1: The trapping laser setup.

Table A.1: Scheme of Trapping Laser Setup.

Item No.	Item Name	Item Description
A01	Half-wave Plate	Rotate the polarization axis of a linearly polarized beam (*combined with* A02).
A02	Polarizing Beamsplitter	Split a beam into two parts with adjustable intensities (*combined with* A01).
A03	Half-wave Plate	Rotate the polarization axis of a linearly polarized beam (*combined with* A12).
A04	Positive Lens	Shrink beam size to get the most 1st order transition efficiency of AOM and get the most coupling efficiency into fiber(*combined with* A06).
A05	Mirror	-
A06	Positive Lens	Shrink beam size to get the most 1st order transition efficiency of AOM and get the most coupling efficiency into fiber(*combined with* A04).
A07	Mirror	-
A08	Acousto-optic Modulator	Work as switching trapping laser on and off; It is also used to switch between the normal loading and the polarization-gradient cooling. It is driven by an op-amp summing box.
A09	Mirror	-
A10	Fiber Coupler	Guide the beam to TA with the spatial mode of the beam well defined.
A11	Mirror	-
A12	Glass	Work similarly as a polarizing beamsplitter (*combined with* A03).
A13	Mirror	-
A14	Cesium Cell	Generate saturation absorption.
A15	Mirror	(*It is put at a lower level*).
A16	Photodiode	Receive saturation absorption signal and send to Digi-Lock.
A17	Fiber Couple	To TA.
A18	Negative Lens	Amplify beam size to get the most TA amplification efficiency (*combined with* A19).
A19	Positive Lens	Amplify beam size to get the most TA amplification efficiency (*combined with* A18).
A20	Mirror	-
A21	Mirror	-
A22	Half-wave Plate	Regulate the polarization of the input beam to TA.
A23	Tapered Amplifier	Eagleyard Photonics EYP-0850-00500-3006-CMT03. It is very sensitive to the polarization of input beam.
A24	Cylindrical Lens	Adjust aspect ratio of the output of tapered amplifier, change it from a oval to a circle.
A25	Mirror	-

Continued

Item No.	Item Name	Item Description
A26	Positive Lens	Shrink beam size to get the most coupling efficiency into the fiber.
A27	Mirror	-
A28	Half-wave Plate	Adjust the polarization of incoming beam to get the maximum transition with well-defined polarization (*combined with* A30).
A29	Quarter-wave Plate	Adjust the polarization of incoming beam to get the maximum transition with well-defined polarization (*combined with* A30).
A30	Polarizing Beamsplitter	Obtain a pure linearly horizontally polarized beam.
A31	Fiber Coupler	Guide the trapping laser to the beam split system with its spatial mode well defined.
A32	Fiber Coupler	To beam split system.

Appendix B

Repumping Laser and Zeeman Slower Laser Scheme

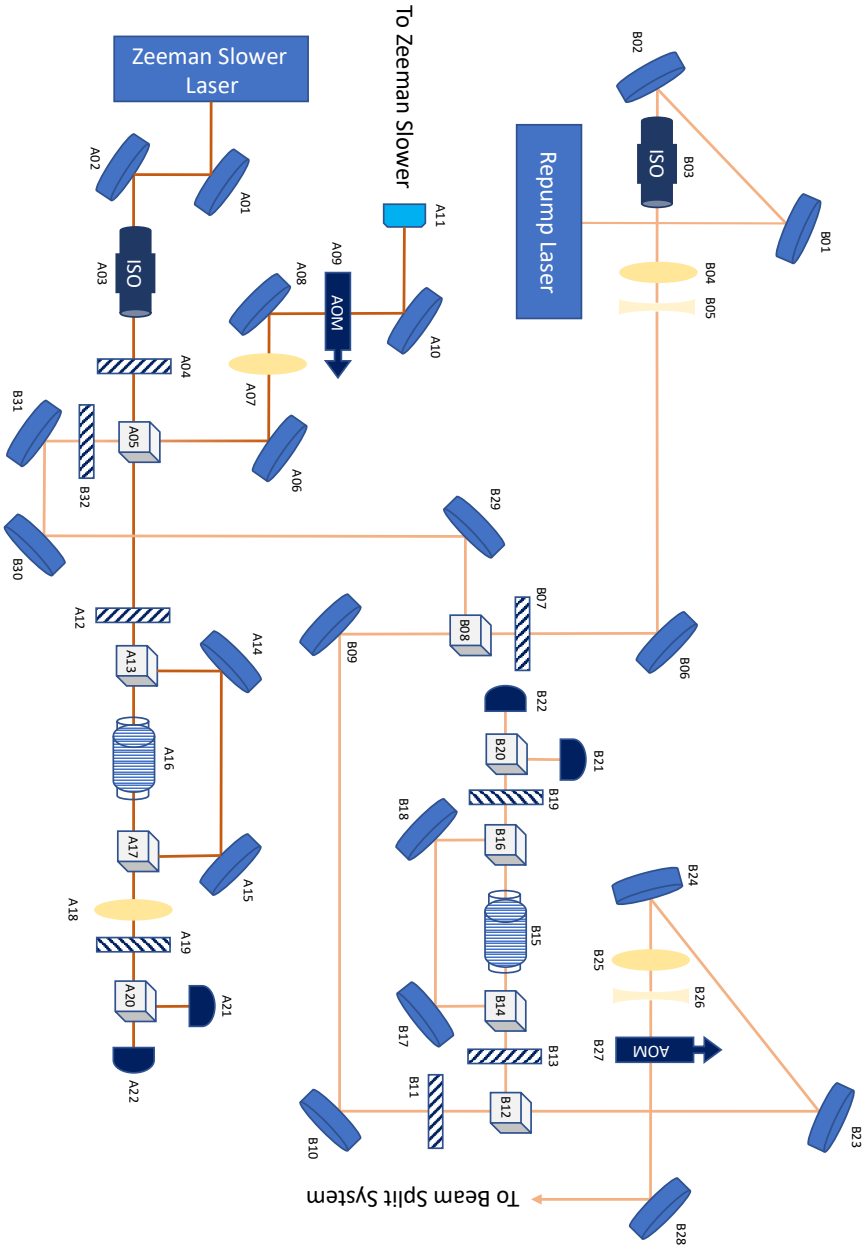

Figure B.1: The repumping laser and Zeeman slower laser setup.

Table B.1: The repumping and Zeeman slower laser setup.

Item No.	Item Name	Item Description
A01	Mirror	-
A02	Mirror	-
A03	Isolater	-
A04	Half-wave Plate	Rotate the polarization axis of a linearly polarized beam (*combined with* A05).
A05	Polarizing Beamsplitter	Split a beam into two parts with adjustable intensities (*combined with* A04).
A06	Mirror	-
A07	Positive Lens	Shrink beam size to get the most 1st order transition efficiency of AOM and fiber coupling.
A08	Mirror	-
A09	Acousto-optic Modulator	Work as switching laser on and off; The frequency shift has to be taken into account to get the best slowing and repumping efficiency.
A10	Mirror	-
A11	Fiber Coupler	Guide the laser light into Zeeman slower.
A12	Half-wave Plate	Rotate the polarization axis of a linearly polarized beam (*combined with* A13).
A13	Polarizing Beamsplitter	Split a beam into two parts with adjustable intensities (*combined with* A12).
A14	Mirror	-
A15	Mirror	-
A16	Cesium Cell	The Cesium cell is surrounded by magnetic rings and twisted by weirs outside. It is used to generate DEVLL saturation absorption signal.
A17	Polarizing Beamsplitter	Fully transparent for the probe beam coming from A13; Fully reflect the pump beam coming back from A15.
A18	Positive Lens	Focus beam on photodiode detector A21 and A22.
A19	Quarter-wave Plate	Transfer left circularly polarized light into horizontally polarized light and right circularly polarized light into vertically polarized light (*combined with* A20).
A20	Polarizing Beamsplitter	Guide right circularly polarized light into A21 and left circularly polarized light into A22 (*combined with* A19).
A21	Photodiode	Generate DEVLL saturation signal (*combined with* A22).
A22	Photodiode	Generate DEVLL saturation signal (*combined with* A21).
B01	Mirror	-
B02	Mirror	-
B03	Isolater	-

Continued

Item No.	Item Name	Item Description
B04	Positive Lens	Shrink beam size (*combined with* B05).
B05	Negative Lens	Shrink beam size (*combined with* B04).
B06	Mirror	-
B07	Half-wave Plate	Rotate the polarization axis of a linearly polarized beam (*combined with* B08).
B08	Polarizing Beamsplitter	Split a beam into two parts with adjustable intensities (*combined with* B07).
B09	Mirror	-
B10	Mirror	-
B11	Half-wave Plate	Rotate the polarization axis of a linearly polarized beam (*combined with* B12).
B12	Polarizing Beamsplitter	Split a beam into two parts with adjustable intensities (*combined with* B11).
B13	Half-wave Plate	Rotate the polarization axis of a linearly polarized beam (*combined with* B14).
B14	Polarizing Beamsplitter	Split a beam into two parts with adjustable intensities (*combined with* B13).
B15	Cesium Cell	The Cesium cell is surrounded by magnetic rings and twisted by weirs outside. It is used to generate DEVLL saturation absorption signal.
B16	Polarizing Beamsplitter	Fully transparent for the probe beam coming from B14; Fully reflect the pump beam coming back from B18.
B17	Mirror	-
B18	Mirror	-
B19	Quarter-wave Plate	Transfer left circularly polarized light into horizontally polarized light and right circularly polarized light into vertically polarized light (*combined with* B20).
B20	Polarizing Beamsplitter	Guide right circularly polarized light into B21 and left circularly polarized light into A22 (*combined with* B19).
B21	Photodiode	Generate DEVLL saturation signal (*combined with* B22).
B22	Photodiode	Generate DEVLL saturation signal (*combined with* B21).
B23	Mirror	-
B24	Mirror	-
B25	Positive Lens	Shrink beam size to get the most 1st order transition efficiency of AOM (*combined with* B33).
B26	Negative Lens	Shrink beam size to get the most 1st order transition efficiency of AOM (*combined with* B32).
B27	Acousto-optic Modulator	Work as switching laser on and off; The frequency shift has to be taken into account to get the best repumping efficiency.

Continued

Item No.	Item Name	Item Description
B28	Mirror	Guide the beam into beam split system.

Appendix C

The Beam Splitting System

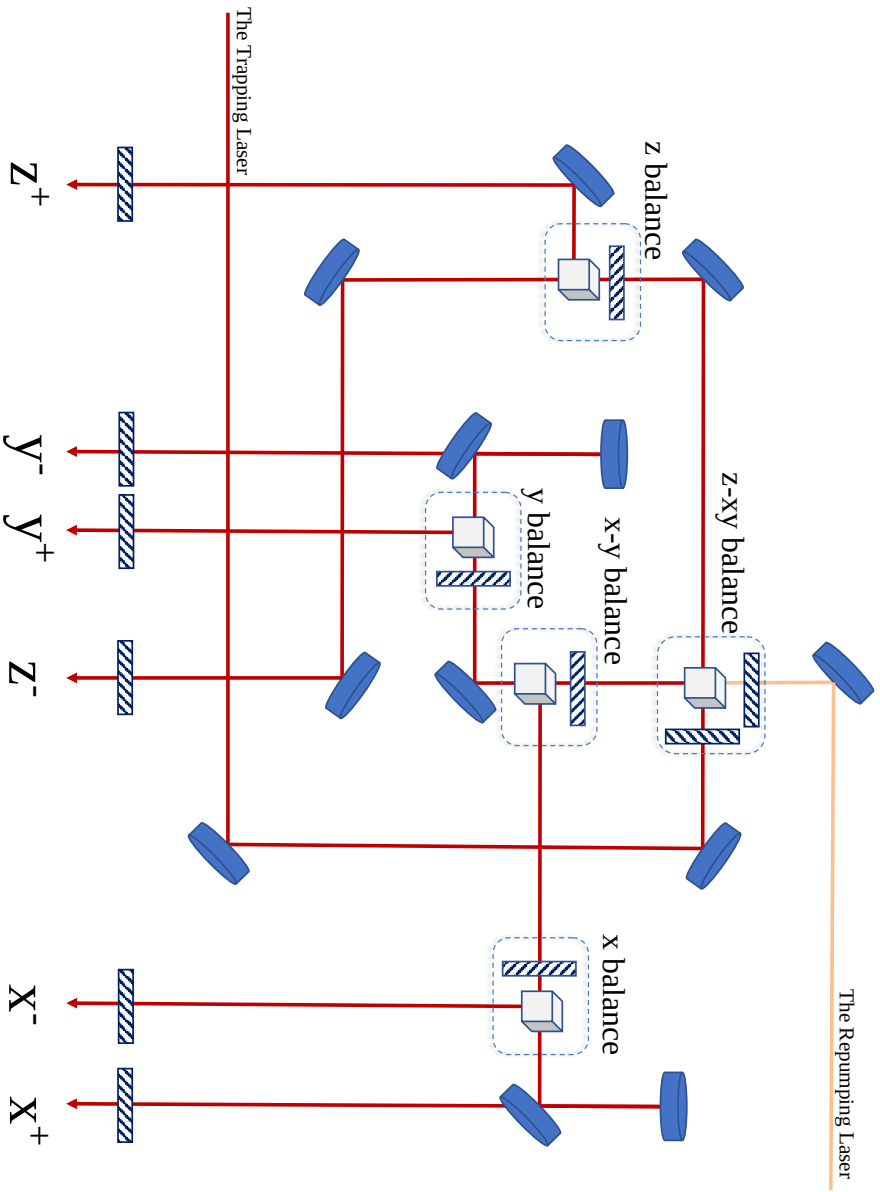

Figure C.1: The beam splitting system.

Appendix D

Two-photon Excitation Scheme

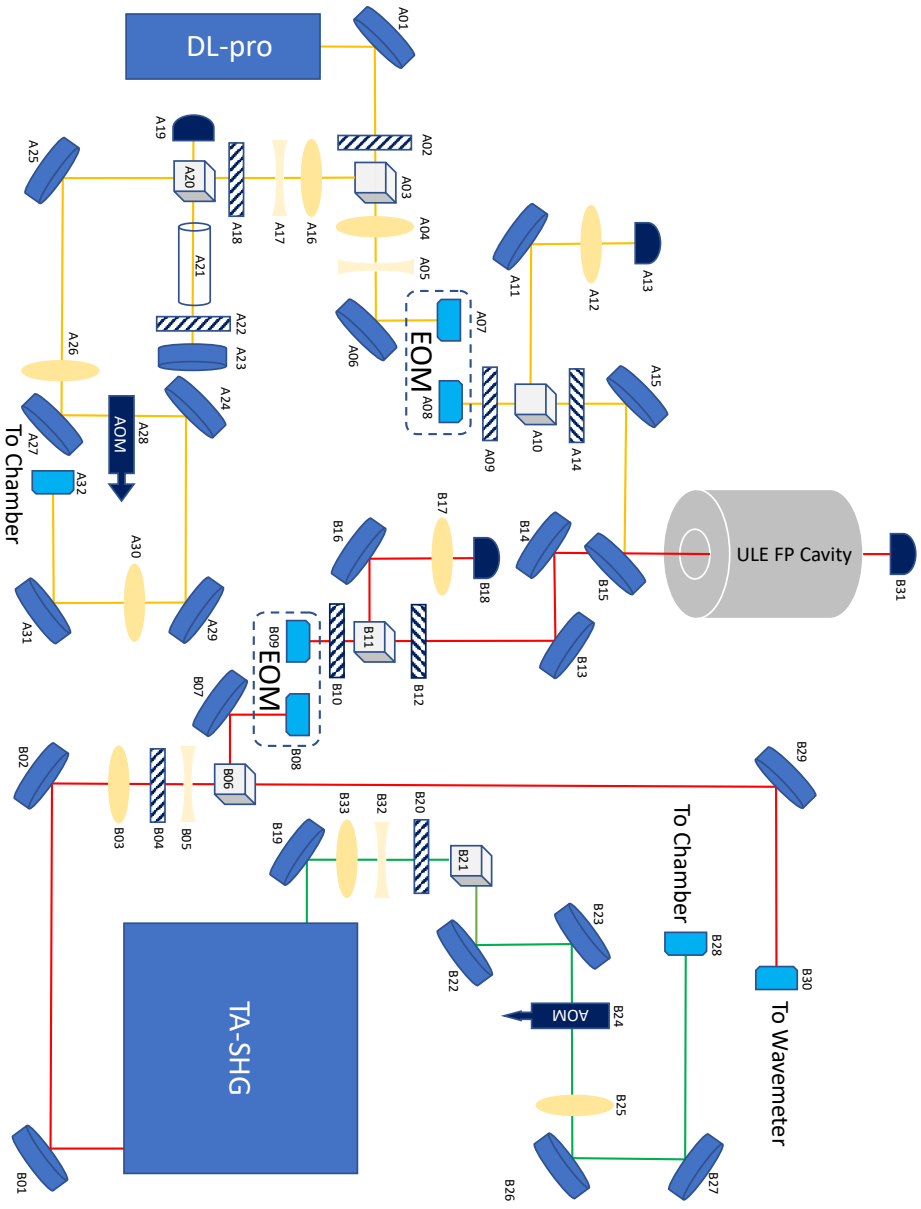

Figure D.1: The two-photon excitation setup.

Table D.1: Scheme of excitation laser setup.

Item No.	Item Name	Item Description
A01	Mirror	-
A02	Half-wave Plate	Rotate the polarization axis of a linearly polarized beam (*combined with* A03).
A03	Polarizing Beamsplitter	Split a beam into two parts with adjustable intensities (*combined with* A02).
A04	Positive Lens	Shrink beam size (*combined with* A05).
A05	Negative Lens	Shrink beam size (*combined with* A04).
A06	Mirror	-
A07	Fiber Coupler	Input of EOM.
A08	Fiber Coupler	Output of EOM.
A09	Half-wave Plate	Rotate a linearly polarized beam, make it fully pass through the next polarizing beamspiltter(*combined with* A10 A14).
A10	Polarizing Beamsplitter	Fully transparent for the beam coming from A09; Fully reflect the beam coming back from A14 to A11 (*combined with* A09 A14).
A11	Mirror	-
A12	Positive Lens	Focus beam on photodiode detector A13.
A13	Pre-amplified Photodiode Detector	Receive the back reflection signal from ULE FP cavity to generate PDH error signal.
A14	Quarter-wave Plate	Rotate beam 45 degrees coming from A10, then rotate it 45 degrees again when the beam reflected back from the ULE FP cavity (*combined with* A09 A10).
A15	Mirror	-
A16	Positive Lens	Shrink beam size (*combined with* A17).
A17	Negative Lens	Shrink beam size (*combined with* A16).
A18	Half-wave Plate	Rotate the polarization axis of a linearly polarized beam (*combined with* A20).
A19	Photodiode detector	Receive saturation absorption signal as reference of the lock point.
A20	Polarizing Beamsplitter	Split a beam into two parts with adjustable intensities (*combined with* A18).
A21	Cesium Cell	Generate saturation absorption.

Continued

Item No.	Item Name	Item Description
A22	Quarter-wave Plate	Rotate beam 45 degrees coming from A20, then rotate it 45 degrees again when the beam reflected back from A23 (*combined with* A20).
A23	Mirror	Covered by a suitable dense filter. The incoming beam works as pump beam; The back reflected beam works as probe beam.
A24	Mirror	-
A25	Mirror	-
A26	Positive Lens	Shrink beam size to get the most 1st order transition efficiency of AOM.
A27	Mirror	-
A28	Acousto-optic Modulator	Work as switching laser on and off; The frequency shift has to be concerned since it adds to the total frequency shift from 6 $^2p_{3/2}$ $F = 4$ state.
A29	Mirror	-
A30	Positive Lens	Shrink beam size to get the most coupling efficiency.
A31	Mirror	-
A32	Fiber Coupler	Guide first step laser beam to the UV chamber.
B01	Mirror	-
B02	Mirror	-
B03	Positive Lens	Shrink beam size (*combined with* B05).
B04	Half-wave Plate	Rotate the polarization axis of a linearly polarized beam (*combined with* B06).
B05	Negative Lens	Shrink beam size (*combined with* B03).
B06	Polarizing Beamsplitter	Split a beam into two parts with adjustable partition of intensity (*combined with* B04).
B07	Mirror	-
B08	Fiber Coupler	Input of EOM.
B09	Fiber Coupler	Output of EOM.
B10	Half-wave Plate	Rotate a linearly polarized beam, make it fully pass through the next polarizing beamspiltter(*combined with* B11 B12).
B11	Polarizing Beamsplitter	Fully transparent for the beam coming from B10; Fully reflect the beam coming back from B12 to B16 (*combined with* B10 B12).

Continued

Item No.	Item Name	Item Description
B12	Quarter-wave Plate	Rotate beam 45 degrees coming from B11, then rotate it 45 degrees again when the beam reflected back from the ULE FP cavity (*combined with* B10 B11).
B13	Mirror	-
B14	Mirror	-
B15	Dichroic Mirror	Fully pass 1064 nm, fully reflect 852 nm.
B16	Mirror	-
B17	Positive Lens	Focus beam on photodiode detector B18.
B18	Pre-amplified Photodiode Detector	Receive the back reflection signal from ULE FP cavity to generate PDH error signal.
B19	Mirror	-
B20	Half-wave Plate	Rotate the polarization axis of a linearly polarized beam (*combined with* B21).
B21	Polarizing Beamsplitter	Split a beam into two parts with adjustable intensities (*combined with* B20).
B22	Mirror	-
B23	Mirror	-
B24	Acousto-optic Modulator	Work as switching laser on and off.
B25	Positive Lens	Shrink beam size to get the most coupling efficiency.
B26	Mirror	-
B27	Mirror	-
B28	Fiber Coupler	Guide Rydberg excitation laser beam to the UV chamber.
B29	Mirror	-
B30	Fiber Coupler	Guide Rydberg excitation laser beam to wave-meter.
B31	Photodiode Detector	Receive transition signal as reference, which is helpful when aligning beams.
B32	Negative Lens	Shrink beam size to get the most 1st order transition efficiency of AOM (*combined with* B33).
B33	Positive Lens	Shrink beam size to get the most 1st order transition efficiency of AOM (*combined with* B32).

Appendix E

Timing Electronics Scheme

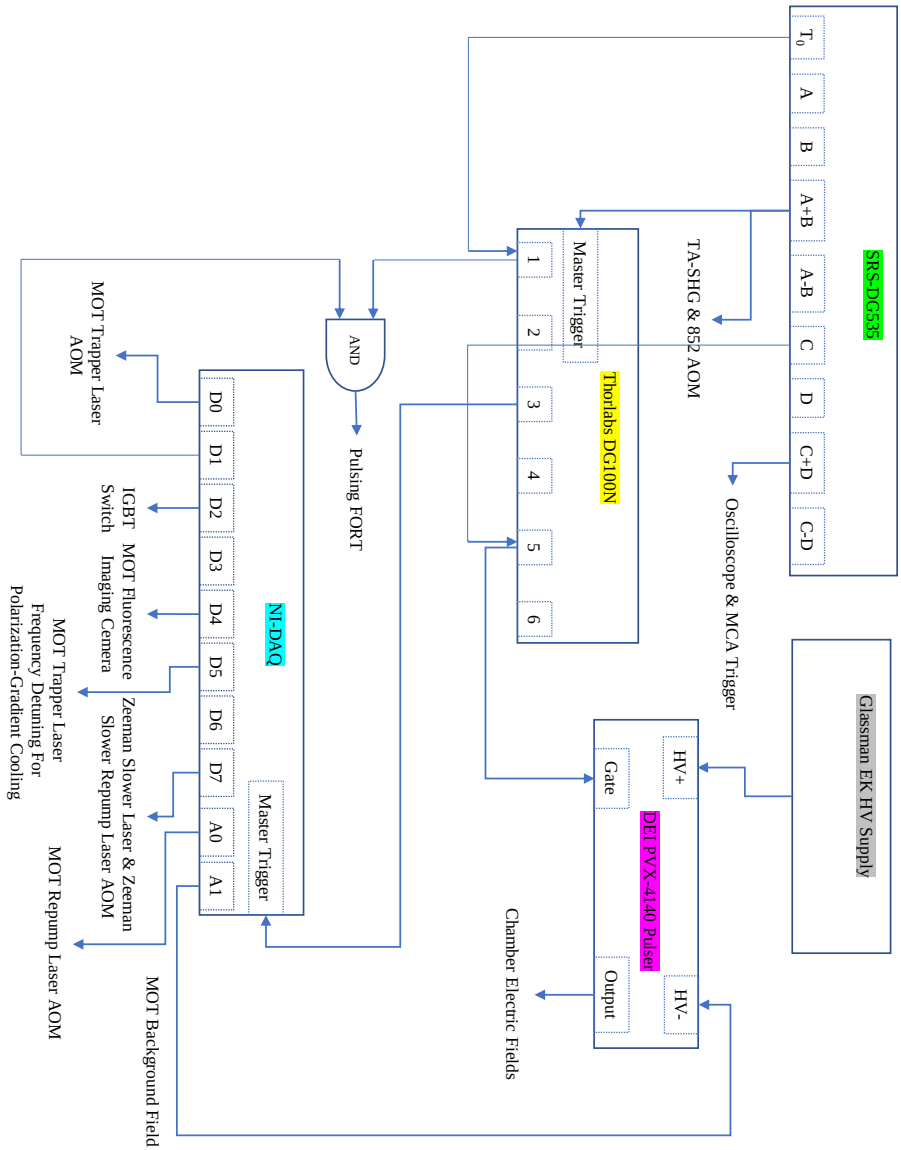

Figure E.1: Scheme of the timing system.

Appendix F

Anisotropic Polyatomic Rydberg Molecules

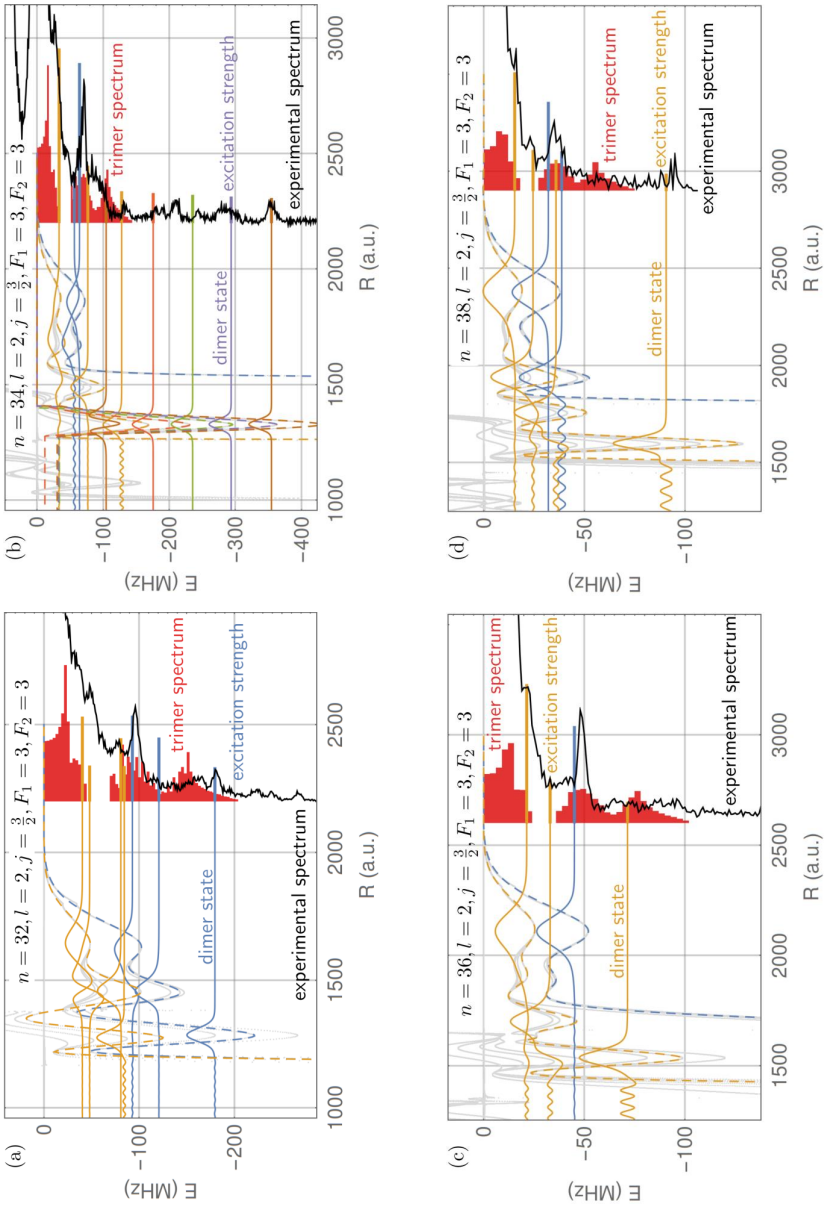

Figure F.1: Theoretical simulations and experimental observations of the Cs $32d_{3/2}$, $34d_{3/2}$, $36d_{3/2}$, and $38d_{3/2}$ anisotropic polyatomic Rydberg molecules. The experimental results only contain Cs^+ signals.